PHYSICS-BASED HIGH FIDELITY MODELING OF HEAT AND MASS TRANSFER IN LASER ADDITIVE MANUFACTURING PROCESSES WITH APPLICATIONS TO PROCESS QUANTIFICATION AND OPTIMIZATION

by

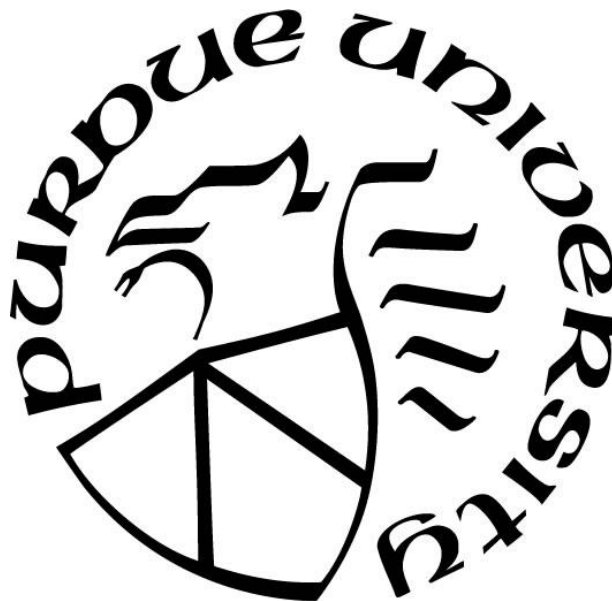**Christopher Michael Katinas**

A Dissertation

Submitted to the Faculty of Purdue University

In Partial Fulfillment of the Requirements for the degree of

Doctor of Philosophy

School of Mechanical Engineering

West Lafayette, Indiana

May 2021

THE PURDUE UNIVERSITY GRADUATE SCHOOL
STATEMENT OF COMMITTEE APPROVAL

Dr. Yung C. Shin, Chair

School of Mechanical Engineering

Dr. Arezoo M. Ardekani

School of Mechanical Engineering

DrMatthew J. Krane

School of Material Science Engineering

Dr. Xiulin Ruan

School of Mechanical Engineering

Approved by:

Dr. Nicole L. Key

ACKNOWLEDGMENTS

What a journey this has been! Along the way, there have been several people who have influenced my time at Purdue and want to acknowledge their efforts, as I wouldn't be here today without them.

First, I want to thank my advisor, Professor Yung C. Shin, for his tireless guidance, patience, and mentoring throughout my program at Purdue. Never in my wildest dreams would I have had the exposure to as much knowledge as he afforded me the opportunity to learn in his research group. In addition, my committee members, Professor Arezoo Ardekani, Professor Matthew Krane, and Professor Xiulin Ruan, thank you for your thoughtful and prompt feedback, even when I didn't make the timeline for such discussions easy for you.

Prior to arriving at Purdue, my time in industry taught me how important teamwork is, but it never prepared me for the exemplification of teamwork I had seen in my lab group. Kyung-Min Hong, thank you for being so patient and willing to help even when experiments never seemed to provide the desired results. Corbin Grohol, not only did you exert 110% all of the time, I will always appreciate how upbeat you were even when impossible situations arose. Neil Bailey, I appreciate all of the time that you spent discussing modeling, experiments, and just about everything else. And lastly, Shunyu Liu, thank you for the time you spent running experiments to validate models contained within this document.

To the friends I have made along the way, you have helped me gain a better understanding what it means to be a friend, whether it be a late night call or a walk around the engineering fountain with a cup of coffee to blow off some steam. Thank you all for being there when I needed you the most.

Last, but certainly not least, my family has helped me out more than they could know. Mom and Dad, you instilled in me an innate sense of respect, curiosity, integrity, which got me to where I am today. Thank you for being a sounding board and for all of the advice you have given me throughout the years, even when it wasn't easy for me to accept. And finally, Jade, you have been my rock throughout this endeavor and can't wait for you to get to the other side as well. I am forever thankful that I've found someone as compassionate and understanding as you have been, and will strive to reciprocate all you have done during this journey.

TABLE OF CONTENTS

LIST OF TABLES

LIST OF FIGURES

ABSTRACT

In the advent of laser additive manufacturing (LAM), extensive efforts have been taken to optimize the properties of resulting manufactured products. Since optimizing these processes experimentally is expensive from both an equipment and materials perspective, modeling of the processes is critical to gain insight into the key parameters necessary to produce a high-quality manufactured component. Physics-based high fidelity modeling of additive manufacturing processes can provide information to predict material properties via track geometry and temperature field; however, previous models require tuning factors that prevent prediction of deposition processes over a wide range of materials or operating conditions.

The overall objective of this research was to develop a methodology to systematically describe each aspect of the LAM process (laser-powder interaction, powder-surface interaction, and heat transfer mechanics) and use the relevant information to feed into various models to predict microstructures, phases, and properties of the resulting deposition. The methodology was demonstrated on a variety of deposition systems, including blown-powder systems and powder bed systems to show the robustness of the method and the predictive capabilities of simulating each of the aforementioned aspects of the process to obtain the track geometry and temperature field, the key factors necessary to determine material properties of as-built components. Although the interactions of the powder, laser irradiation, and substrate are different in nature and must be modeled with due-diligence, these were found to be boundary conditions for a common-core deposition model applicable for any LAM process.

For blown-powder systems, computational fluid dynamics (CFD) was used to calculate the average spatial distribution of powder as the powder is ejected from a gas-assisted nozzle. This was then coupled to the molten pool dynamics model, which involves melting, fluid flow and subsequent heat transfer to the surrounding areas, which are solved by a set of coupled momentum, continuity and energy equations with proper source terms and boundary conditions with the free surface tracked using the levelset method. This model was subsequently applied to H13 and Ti-6Al-4V powder being deposited on their respective substrates in a single-track configuration to understand the temperature field and track geometry throughout the LAM process. These studies enabled the prediction of the phases, microstructure, residual stress and hardness of as-built components produced with blown-powder LAM for these two materials. More importantly,

predictions of capture efficiency were obtained, as opposed to using capture efficiency as an input, which previous researchers relied on as a model tuning parameter. The study of Ti-6Al-4V was taken further by simulating a multi-track deposition with the same LAM parameters and was shown to predict the molten pool region, heat affected zone, and track geometry after three tracks were simulated without the need for any model tuning. Since powder concentration could be calculated throughout the computational domain, the effect of standoff distance on the deposition process was studied to optimize the best cladding condition for Stellite-6 cladding of a mild steel substrate, wherein the cladding is often performed with the laser focal point above the substrate surface to minimize dilution.

The AM model has been extended to powder bed additive manufacturing by modeling particle-particle and particle-surface interactions via a discrete element model coupled with the molten pool dynamics model developed for the blown powder model. Particles of Ti-6Al-4V were modeled with aerodynamic drag and cohesive forces to demonstrate the effect of evaporative-driven gas flow during powder bed deposition, a phenomenon which has been observed experimentally, but had yet to be modeled with reasonable accuracy when coupled to a LAM process model. Simulation of the powder bed formation was included to consider particles of multiple sizes and multiple spreading passes, which is necessary for obtaining a physically representative powder bed. Finally, the model was updated with a robust dual-mesh algorithm that allows for the simulation of high scanning speed processes for large manufactured components without excessive computational effort associated with large-scale simulations.

With these modeling processes being used to predict the geometry and temperature field of a deposition, regardless of the powder feed mechanism, the results could be used to verify optimal LAM parameters from experimentation. Unfortunately, computational effort and cost for modeling of these processes for a large domain is prohibitively expensive, which is needed to determine the resultant microstructure and mechanical properties of industrial large-scale parts. Though having a high-fidelity model of the deposition process enables accurate prediction of the track geometry and temperature fields, methods to increase model throughput are necessary to obtain accurate process predictions without excessive computational effort. A combination of an Arbitrary Lagrangian-Eulerian mesh formulation and volumetric powder-bed heating methods decrease computational effort compared to analogous models in literature by up to 95%.

CHAPTER 1.   INTRODUCTION

1.1   Motivation

Additive manufacturing has garnered significant attention within the last quarter century due to its diversity in both manufacturing and remanufacturing processes. In 2012, the yearly global revenue for additive manufacturing processes was expected to reach $21 billion by 2020 (Wohlers, 2012). Additive manufacturing methods have been sought after in instances where traditional manufacturing methods are unable to achieve desired geometry, specifically when generating internal geometries which could be too costly or impossible to obtain via traditional manufacturing, as is the case for the heat exchanger shown in Figure 1.1. Because of this, high-performance automotive and aerospace components have shifted towards additive manufacturing compared to their traditionally manufactured counterparts (Calignano, 2020).
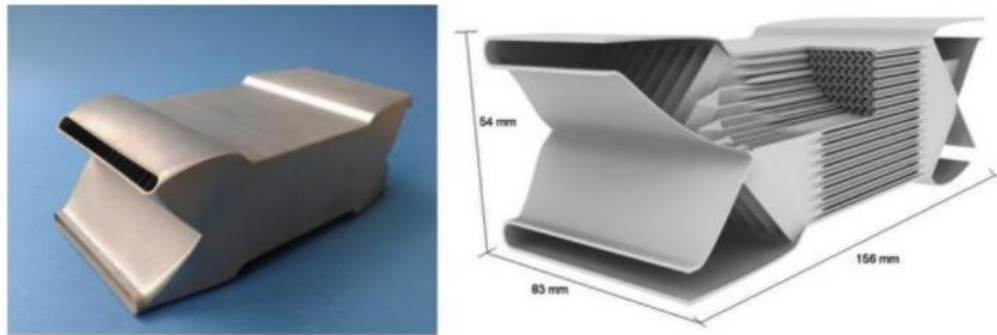
Figure 1.1: Heat exchanger built using additive manufacturing (extracted from (Scheithauer et al., 2018))

Three primary classes of metal additive manufacturing (AM) processes exist: (1) blown powder-based processes (Weerasinghe and Steen, 1986), (2) powder-bed based processes (Powell et al., 1988), and (3) wire-feed processes (Henri et al., 2012), each of which has their own benefits and disadvantages. In literature, the most commonly discussed deposition method is blown powder due to its relative versatility, control of the process and non-contact approach (Weerasinghe and Steen, 1986, Sexton et al., 2002, Lin and Steen, 1998).

In blown powder processes, a powdered material is blown onto a substrate via inert gas propulsion from a powder feeder nozzle while the substrate and powder are melted via laser

irradiation, as shown in Figure 1.2 where one such blown powder process, laser direct deposition (LDD), is exemplified. One significant advantage of blown powder processes is that many combinations of materials can be used for the powder and substrate, allowing for thin surface coatings, monolith construction, functionally gradient structures, synthesis of metal-matrix composites, tool remanufacturing, or an alternative manufacturing method where traditional manufacturing approaches are cost-prohibitive (Atwood et al., 1998).

Alternatively, in powder bed processes, the powder is spread upon the surface of a substrate to generate a bed of powder and irradiating the powder particles until they melt and adhere to the surface of the substrate. Laser-powder bed fusion (L-PBF) is an additive manufacturing process in which powder is placed upon the surface of a substrate and irradiated with a laser heating source to melt the powder and physically bond the powdered material to the substrate or previously formed surface. L-PBF has gained significant attention over the last several years due to its versatility as an alternative manufacturing method to fabricate parts with complex features or internal geometry. Due to the nature of the rapid heating and cooling cycles observed during the process, finer microstructures are obtainable over traditional manufacturing methods, and may lead to final products with higher strength depending on additive manufacturing process conditions (Zhang et al., 2018). A favorable process condition requires sufficient laser energy to not only heat and melt the particles through the thickness of the powder bed, but also bond the molten material to the substrate surface without causing subsurface defects such as porosity and cracking (Khairallah et al., 2016).
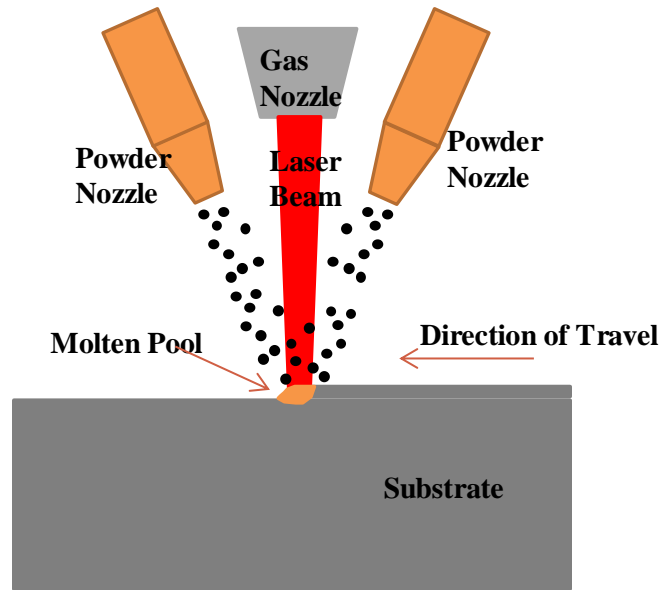
Figure 1.2: Laser Direct Deposition Process Diagram

Blown powder processes encompass much of the additive manufacturing realm due to their versatility and speed. Three types of blown powder methods exist: coaxially blown powder feed (laser and powder concentric axes are congruent), side-feed powder feed, and multiple-nozzle powder feed. Advantages of coaxial cladding include direction-independent control of the process and a multi-directional flow of powder, which enables the potential for a more uniform powder delivery process (De Oliveira et al., 2005). Many previous researchers have used side-impinging powder feeding mechanisms, which although has been shown to increase the amount of powder adhered to the substrate, the nozzle location must be tuned and configured for each system (Weerasinghe and Steen, 1987, Jeng et al., 1991, Frenk et al., 1997). In general, a significant problem of the blown powder processes is that experimental tuning is essential to produce favorable results, especially for custom-designed systems.

Advances in manufacturing technologies continually extend the capabilities in the synthesis of additively manufactured products. Compared with the traditional manufacturing methods such as hot rolling, forging and casting, blown powder AM provides a more effective and economical way of fabricating near-net shape complex products without extra expense (Wu et al., 2004). Blown powder AM can also be applied to repair worn-out components or to build a new part on an existing old part with favorable metallurgical bonding (Wilson et al., 2014, Yang et al., 2017). In addition to improved manufacturing flexibility, the blown powder AM process can

15

produce finer microstructures than typical manufacturing methods due to the rapid heating and cooling thermal cycles during the process (Vrancken et al., 2012, Yu et al., 2012, Shunmugavel et al., 2015). It has been successfully used to generate fully dense components with improved hardness (Wilson and Shin, 2012), strength (Wang et al., 2007), and both wear and corrosion resistance (Zhang et al., 2008, Liu et al., 2014a) when compared to other manufacturing methods.

A multitude of materials can be used in blown powder processes, and include Ti6Al-4V (Bian et al., 2015, Qiu et al., 2015b), Stellite-6 (D'Oliveira et al., 2002), H13 tool steel (Pinkerton and Li, 2005), stainless steels (Hunt et al., 2014) and aluminum alloys (Isanaka et al., 2016), among others. Ti-6Al-4V, a titanium alloy that is widely used in the aerospace, motor manufacturing, medical implants, marine anti-corrosion and petrochemical industries is a high strength, low weight ratio alloy with outstanding corrosion resistance and superior biocompatibility. Among all the titanium alloys, Ti-6Al-4V alloy encompasses about 50% of titanium alloy usage due to its superior overall properties (Donachie, 2000). Additionally, Ti-6Al-4V has often been used as a matrix for metal matrix composites with improved wear resistance and mechanical properties (Banerjee et al., 2003, Wang et al., 2007, Rastegari et al., 2011, Mahamood et al., 2013, Liu et al., 2014b, Mahamood and Akinlabi, 2015). Another material common to blown powder processes is Stellite-6 as a hardfacing coating for the primary purpose of material addition for repair of worn or corroded components (Denney, 1991). In 1987, the first reported cladding of Stellite-6 on mild steel was performed by Singh and Mazumder (1987) who used a side-impinging powder nozzle with Stellite-6 powder to develop multi-track clads on mild steel to investigate microstructure. The third material which will be used in this study is H13 tool steel, which has excellent material properties such as high toughness, high stability in heat treatment, and high resistance to thermal fatigue cracking (Roberts et al., 1998). Because of these properties, H13 is the standard material used in industry for tooling in hot work applications such as die casting, forging, and extrusion.

Experimental studies on the geometry of AM structures have been performed to investigate optimal processing parameters for a variety of deposition systems (Qiu et al., 2015b, Kobryn et al., 2000). Unfortunately, optimizing the process experimentally can be very costly since many of the parameters (including nozzle geometry, stand-off distance, laser power, powder feed rate, scanning speed, and hatching distance) will influence the final geometry of the deposited material and underlying microstructure (Kobryn et al., 2000). Track geometry is directly influenced by the amount of powder captured by the molten pool. Typically, powder particles are emitted from the

powder feed nozzles and are aimed to impact the molten pool; however, depending on the process parameters, the amount of powder adhered to the surface of the substrate is limited. Therefore, an understanding of the capture efficiency during blown-powder processes is necessary since it directly influences the overall process efficiency and may impact factors such as cost and duration of the AM process. In addition, the powder that has not been captured during the process may require a reclamation process to ensure feed powder quality and composition remains consistent with raw feedstock.

As with most engineered systems, trade-offs within an AM process exist and must be understood fully to optimize process conditions. Previous researchers have worked in the development of heuristics to understand how each process variable affects the resulting product, and how to improve the quality of the resulting deposition to prevent undesirable conditions such as porosity (Weerasinghe and Steen, 1986, Hoadley et al., 1991) and micro-cracking (Liu and Li, 2005). A systematic approach to assess the process becomes necessary to reduce system tuning efforts and optimize processing parameters to reduce waste, produce the highest quality product while also increasing throughput.

A significant amount of effort to model blown powder processes has been exerted, though most of the work has been focused on the relatively simple case of coaxial nozzle powder delivery systems (Lin and Steen, 1997, Lin, 2000, Pinkerton and Li, 2004a, Thakar et al., 2004, Zekovic et al., 2007, Yang, 2009, Wen and Shin, 2010, Ibarra-Medina et al., 2011). Instead, various types of nozzles exist, including side-impinging and multi-nozzle powder sprayers, among other customized nozzles which may exist. Figure 1.3 provides an example of one such "complex" nozzle which can be found on the Optomec LENS 750 additive manufacturing system. Four nozzle systems provide flexibility in the manufacturing of components with higher complexity, but at the expense of powder capture efficiency (Gibson et al., 2015).
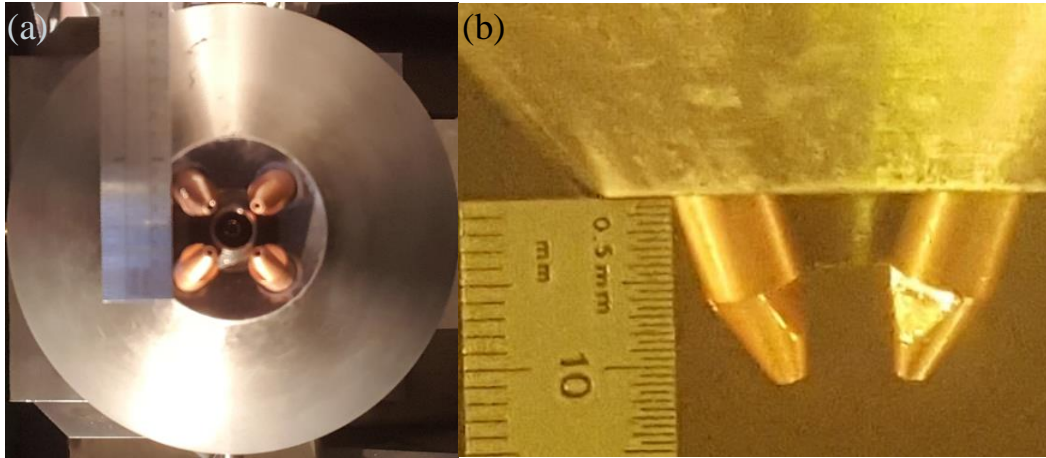
Figure 1.3: Optomec LENS 750 nozzle geometry – (a) bottom view, (b) side view

To fully understand the blown powder AM processes, three main interactions must be understood to assess the impact on the resulting deposited layer: laser-powder, laser-substrate, and powder-substrate interactions. The ability to describe each of these interactions for the materials being added enables an in-depth study into the process beyond a parametric study for a given blown powder system. Furthermore, system tuning can be minimized if an understanding of at least one of the aforementioned interactions is understood for the system at hand, and has been the focus of much literature regarding coaxial nozzles. Similarly, the complexity of the L-PBF process requires several facets of the process to be considered when modeling, including particle placement upon the substrate, laser-particle interaction, laser-substrate interaction, particle melting, and evaporation due to laser-material interaction. Ultimately, it is necessary to develop a physically representative model which can be simulated in a reasonable timeframe and still maintain high fidelity of the physics at hand. Furthermore, each aspect of the process must be considered to successfully predict the resulting molten bead and temperature field, each of which will affect the final microstructure and resultant mechanical properties of the manufactured product.

As it will be shown, methods used to model such processes are not robust or reliable enough to model additive manufacturing processes without using tuning factors or significant assumptions which limit the utility for different materials or different AM equipment. Furthermore, the models reviewed within literature which are capable of providing an estimation of the track geometry are too expensive computationally, which limits their practicality in an industrial setting to design AM components. Thus, for a given model to be impactful, it must be able to accurately describe any

given deposition process with adjustability to accommodate for varying mass addition techniques, whether blown-powder, wire-fed, or powder bed fusion additive manufacturing.

1.2   Literature Review

1.2.1   Blown Powder Additive Manufacturing

Modeling of the LDD process has been carried out extensively in the last two decades to understand various physical phenomena associated with the process. Significant effort has taken place to predict the temperature, melt flow, powder flow, and resulting geometry during laser cladding and laser direct deposition. The first model was a two-dimensional representation of a laser alloying operation, but gave rise to a numerical method to describe powder thermal effects and species diffusion within a laser-irradiated substrate (Chande and Mazumder, 1985). This relatively primitive model neglected molten pool dynamics, and rather focused primarily on diffusion processes, which limits applicability to high laser power LDD operations.

The next major contribution was a primary driver to understand the resulting shape of the deposited material and molten pool. Assuming a 1-D Gaussian heating source via simulation of a blown powder process in a two-dimensional domain, finite element analysis was used with a penalty method through a source term of the momentum equation to enable the effect of free surface tracking while incorporating the Navier-Stokes equations (Hoadley and Rappaz, 1992). This particular study has led to a plethora of solution techniques in an attempt to model blown powder processes: whether to use finite element or finite volume techniques, the former which will briefly be reviewed. Within the last several years, some researchers have focused on using finite element analysis to understand LDD processes. Peyre et al. (2008) used a finite element analysis to predict the temperature and track height during deposition by mapping the powder concentration and laser intensity profile to enable molten pool formation, but could not predict the track shape since surface tension and other molten pool flow-related effects were neglected. Vasquez et al. (2012) modeled conservation of mass, momentum and energy governing equations using COMSOL, a commercially-available finite element analysis solver, but assumed a molten pool shape and width instead of allowing the model to provide the corresponding thermal boundary. Heigel et al. (2015) modeled the deposition process of Ti-6Al-4V using finite element analysis, which included the four-nozzle powder delivery system described in Figure 1.3; however, effects

from the molten pool dynamics were neglected, which are known to increase effective heat transfer from the molten pool and cause track geometry changes. Chiumenti et al. (2017) attempted to develop a framework to describe the analysis of the additive manufacturing process; however, their focus was limited to finite element methods for energy conservation, and neglected fluid dynamics of the molten pool region. Recently, Song et al. (2018) used finite element analysis to describe molten pool dynamics and energy transfer during a single-track deposition process, which correlated well against experimental cases for track shape and molten pool geometry. Unfortunately, the molten pool flow which was presented in their scenarios indicated incorrect directionality, as Marangoni shear stress drives fluid flow in the direction of the surface temperature gradient when the material exhibits a negative surface tension coefficient. Finite element analysis suffers from one major drawback: only global conservation of solved parameters is guaranteed. In finite volume solutions, local conservation can be guaranteed. Furthermore, in finite element methods, flux limiting is not feasible, leading to unstable solutions depending on the discretization scheme utilized, and thus, finite volume methods will be primary focus of numerical schemes for LDD modeling.

Nozzle analysis was one of the key drivers in the initial understanding of the LDD process by providing an understanding of how powder emerges from a powder feed nozzle, and describing the powder available to be absorbed by the molten pool. With the invention of the coaxial powder feed nozzle in 1996 (Aleshin, 1996), an abundance of studies have been performed to investigate optimal process parameters for the blown powder processes involving coaxial nozzles. Analytical models for powder flow during the LDD process were established within a year of the invention of the nozzle (Jouvard et al., 1997), and investigated the powder heating process through the laser irradiation region as well as the energy reaching the substrate by using a Beer-Lambert attenuation law. Lin and Steen (1997) predicted capture efficiency assuming a Gaussian powder distribution (produced at the focal point of coaxial nozzles) and a molten pool width based on the laser beam diameter. The critical issue of this analysis occurs when there is excess powder for the available laser energy, resulting in overestimated capture efficiency. Numerical simulation of the powder flow from a coaxial nozzle was investigated further (Lin, 2000). Lin used Ansys FLUENT (ANSYS, 2009), a commercially-available numerical computational fluid dynamics software package, to simulate the powder flow emerging from the nozzle using a gas-particle mixture known as a discrete phase model. In such a model, particle trajectories were solved assuming

particles are driven by the gas phase. One-way coupling with the gas is a common assumption (Crowe, 1982) and enables particles to be propelled by the gas stream, but added particle momentum is not removed from the gas phase. Though a simplified domain was utilized, it provided the initial motivation to simulate more complex powder flow from a variety of nozzles.

Analytical models of the LDD process then became more prevalent in literature since the numerical analysis of AM processes was still computationally prohibitive. Fu et al. (2002) modeled the cladding process analytically, assuming a radially-symmetric powder distribution being heated by a laser irradiation source at an arbitrary angle with respect to the laser beam center axis. In their analysis, particles were modeled to accomodate phase change, which would be observed while the particles are irradiated within the laser beam, but used constant particle diameters and thermal properties with respect to temperature to simplify the analysis. Han et al. (2004) solved mass, momentum, and energy governing equations to understand the cladding process using a coaxial nozzle, and included laser beam attenuation, powder impingement and the effect of recoil pressure due to evaporation, but used particles of a single diameter (as opposed to the physical particle size distribution) for their powder characterization along with constant thermal and physical properties. Furthermore, their analysis used discrete particles to model the effects of individual particles impacting and melting within the molten pool, but assumed that particle concentration followed a Gaussian distribution. Pinkerton and Li (2004a) developed an analytical model to describe the powder distribution from a coaxial nozzle as a function of distance from the nozzle, and validated their findings using light scattering experimentation. Since laser scattering can impact the net energy used to heat both the powder and substrate, this result provided insight into using Mie scattering representations when modeling particle-laser interaction. Pinkerton and Li (2004b) had also developed a numerical model to describe a single-track cladding process in an effort to gain insight to situations where full bonding of the powder was not achieved, though their analysis used a uniform powder distribution and neglected surface thermal losses such as radiation and convection. As noted by the researchers, such situations lead to porosity and internal material defects, which are not desirable during additive manufacturing processes. Fathi et al. (2006) developed an analytical model to assume the shape of the molten pool free surface as a paraboloid, while assuming the temperature profile of the substrate can be described by an analytical moving heat source model (Carslaw and Jaeger, 1959). Though there is a basis for such simplifications given the complexity of laser-based additive processes, accuracy is greatly

sacrificed for speed and will only work in limited cases. Lalas et al. (2007) developed an analytic model to describe the free surface of the clad and the molten pool geometry based on the contact angle between the molten bead and the substrate. Though this method is slightly more physical than its predecessor, it generates a circular arc for the free surface which is only representative of a molten bead without fluid motion and at a constant temperature throughout. Partes (2009) developed a model to predict the capture efficiency of the process by assuming a Gaussian distribution of powder adjusted for nozzle incline angle. By using experimental images of the molten pool during the process and developing a mathematical representation of the isotherm, powder capture efficiency could be determined based on particles which reached the solidus temperature prior to reaching the molten pool surface. Unfortunately, this method requires *a priori* knowledge of the molten pool boundary, which is the goal of attempting to simulate the deposition process.

Blown-powder heating and attenuation were investigated analytically by Diniz Neto et al. (2007), but their powder distribution was assumed to follow two prescribed powder mathematical representations, which significantly simplified their analysis and the applicability for use within physical cladding systems. In an attempt to reduce calculation time for the powder flow calculation, Pinkerton (2007) developed an analytical model for the powder flow and temperature distribution of particles ejected from a coaxial nozzle by demonstrating that multiple powder distributions exist within the powder stream depending on the distance from the powder focal plane, though the study was limited to particles of a single diameter. Particles used in typical blown powder processes are an agglomeration of multiple diameters (Katinas et al., 2018), which limits the applicability of such modeling to idealized processes. Wen et al. (2009) performed a computational fluid dynamics simulation of the powder flow from a coaxial nozzle and included a particle heating model. In their analysis, a Rosin-Rammler particle distribution was considered which more closely resembles the particle size distribution observed in manufactured powders, and could be applied to practical AM processes. Ibarra-Medina and Pinkerton (Ibarra-Medina and Pinkerton, 2011) investigated the interaction of the substrate including powder flow and laser irradiation phenomena using CFD analysis including the interior of the coaxial nozzle. They determined that interactions within the nozzle play a significant role in the dispersion of the emitted powder cone, and that varying the stand-off distance of the nozzle to the substrate can drastically change the available powder concentration at the molten pool surface. Tabernero et al. (2012) developed a more in-

depth understanding of laser-beam attenuation in coaxial nozzles by combining the powder concentration collected from a CFD model and using a particle heating model. Their model was validated against experimental data for different sized particles and different materials and could be used to gain insight into energy scattering and absorption during laser-particle interaction. Around the same time, He et al. (2010) developed a numerical model to study the temperature, fluid flow, and species transport and used it to study two-track laser cladding of H13 powder onto an H13 substrate, enhancing the field with a multi-track simulation of the deposition process. However, they applied some relatively critical assumptions by using constant thermal and physical properties (though their model was capable of temperature-dependent thermal properties), and assuming small (~10 μm diameter) and uniformly-sized spherical powder which melted upon contact at the liquid surface, a laser divergence half-angle of zero degrees, and a prescribed transverse scanning velocity between adjacent tracks different from the laser scanning speed. In addition, no track or molten pool profiles were provided to substantiate the results of the simulated deposition process against experimental data, but rather primitive dimensions of the clad height, width and depth were compared. Manvatkar et al. (2015b) built a numerical model that predicts the temperature and approximate geometry during the process and used it to analyze the deposition of a thin-walled structure of 316SS by including a powder heating model with and temperature-dependent thermal properties. In their analysis, particles with large diameters (175 μm) were used, which is known to increase surface roughness (Griffith et al., 1996).

As can be seen thus far, much of the available literature is germane to coaxial nozzle powder delivery systems, which limits the applicability of predicting blown powder processes for different nozzles. Analysis of a four-nozzle powder delivery system was addressed by Zekovic et al. (2007) using FLUENT to characterize the powder flow and particle velocities and how particle-substrate interaction would occur. Results were presented for the interaction of the powder stream against a tall thin-wall structure, which is one limiting case of blown powder processes (the other limiting case is deposition on large substrates). Ibarra-Medina et al. (2011) included the influx of powder particles from a four-nozzle powder feeder in their model and used the volume of fluid method to track the free surface, as opposed to levelset surface reconstruction, but their track profile shape was inconsistent with experimental data under the simulated conditions.

The most generically applicable work came with Wen and Shin (2010) when they used computational fluid dynamics to investigate powder concentration emerging from a four-nozzle

powder feed system. Though the powder and temperature profiles were not validated experimentally, the modeling process was similar to their previous work in coaxial nozzle powder flow (Wen et al., 2009). They used a constant powder concentration based on the average powder concentration from their four-nozzle powder feed analysis, and simulated a laser direct deposition process to show reasonable agreement to experimental depositions. In their analysis, Wen and Shin reformulated the levelset governing equation into conservative form to provide a substantial improvement upon previous analysis using levelset surface tracking, since it allowed a simultaneous solution to all governing equations. The levelset tracking methodology was used in conjunction with a fully-implicit solver, as opposed to a multi-step algorithm which involves solving the levelset governing equation separately once the remaining governing equations were solved. Wen and Shin hadn't included a levelset reinitialization scheme since molten pool velocities were relatively small in magnitude. Such a scheme, which ensures the levelset field isocontours remain geodesic (Min, 2010), becomes important with high molten pool convection. Wen and Shin (2011) subsequently used their single-track model and extended the analysis to a multi-track simulation, which pioneered more complex blown powder depositions by enabling the benefits of a fully-implicit numerical scheme introduced with their previous single-track model with the capability to handle temperature-dependent thermal and physical properties, an arbitrary laser irradiation source, and arbitrary powder size and distribution.

To date, the most significant deficiency in blown-powder additive manufacturing models is a generic framework to address solutions using any given powder feeding nozzle, as opposed to a coaxial nozzle. Limiting assumptions, such as use of analytical models to describe powder distribution or powder-laser interaction, can be used readily in instances of radially symmetric nozzles; however, they prevent applicability to other powder feed systems, including those which are custom-designed.

1.2.2   Laser - Powder Bed Fusion Additive Manufacturing

Particle arrangement during powder bed processes is most commonly modeled with a discrete element method (DEM), a simulation that models the interactions of individual particles within a large-scale system (Cundall and Strack, 1979). Several researchers have utilized DEM to simulate the initial stage of the L-PBF process (Lee and Zhang, 2016, Parteli and Pöschel, 2016, Steuben et al., 2016, Xiang et al., 2016, Zohdi, 2006, Haeri et al., 2017, Haeri, 2017, Zhang et al.,

2018), and is similarly performed in this study to acquire the initial placement of powder upon the substrate surface.

After the powder placement, it is the treatment of the laser interaction with the powder, molten pool and substrate, which distinguishes the predictive capability of the L-PBF modeling effort, and becomes a significant source of discussion. Two different methods have been used to model the laser-powder interaction: ray-tracing models and volumetric models. Ray tracing models use known configurations of particles to determine trajectories of a large quantity of incident rays throughout the particle bed and gain insight into the location and amount of energy absorbed by each surface interaction as well as the amount and energy and direction of the reflected energy. Since the absorptivity of laser irradiation into a powder bed changes as a function of particle size, temperature, and arrangement, ray-tracing models provide an accurate physical representation of the absorption phenomenon (Zhou et al., 2009, Boley et al., 2015). Unfortunately, the computation time of ray-tracing models hinders the ability of their use for large-scale powder beds, which would be seen when modeling the L-PBF process for a typically manufactured component. In one such example, Khairallah et al. (2016) established an L-PBF model for a single-layer powder bed, which uses single-reflection ray tracing energy addition and an evaporation model to allow for prediction of molten pool concavity; however, since multiple reflections were neglected to save on computational effort, thicker powder beds could not be simulated properly. In addition, model results from Khariallah et al. (2016) provide the appearance that the molten bead can be concave upon mass adhering to the substrate, a phenomenon that only pertains to thin powder beds since there may be insufficient powder mass to locally absorb the laser energy.

As an alternative, volumetric methods have been used to provide an estimate of the absorption phenomenon by using a Beer-Lambert attenuation law (Gusarov and Kruth, 2005, McVey et al., 2007, Gürtler et al., 2013) to represent the effective absorptivity of the powder bed without the need for their ray-tracing counterparts. Volumetric energy addition requires an attenuation factor to determine the laser energy decay through the powder bed, and is found from ray-tracing modeling of thick powder beds (King et al., 2015a) or experimentation to assess laser irradiation reaching the substrate surface (Trapp et al., 2017). Unfortunately, researchers using volumetric energy addition methods have either made additional assumptions or have neglected remaining physics of the L-PBF process. For example, Bertoli et al. (2017) modeled volumetric heating of a stainless steel powder bed using finite element methods to determine the heating and

cooling rates during laser scanning, but could not model keyholing during L-PBF since fluid motion effects were neglected, and rather focused on track geometry and temperature profiles during the process. Zhang et al. (2018) assumed an effective temperature profile for the powder bed based on a uniform beam intensity profile, rather than determining the energy absorption on a per-particle basis to calculate the individual particle temperatures.

The core of the L-PBF model describing the complex physics of powder melting, molten pool formation, evaporation and keyhole formation is the primary driver of model accuracy and has evolved over the past 15 years, initiated with studies in finite element modeling of the process. Dai and Shaw (2004) used finite element analysis to provide insight into the melting and solidification phenomena of nickel-based alloys with ceramic powder. Though they included temperature-dependent physical properties within their analysis for both materials, only the energy equation was solved. Gusarov and Smurov (2010) described the consolidation kinetics of the powder bed during the melting process, but only included effects from the laser energy absorption on the particles and neglected fluid flow of the gas and molten pool itself. Similar methods using FEA without fluid dynamics have been attempted within the literature, and use localized mesh refinement to generate a solution faster; however, they continue to neglect important physics of laser-material interaction (Patil et al., 2013, Patil et al., 2015, Zeng et al., 2015). For reasons mentioned in section 1.2.1, finite element analysis is not considered an exemplary tool to describe the complex physics of laser-based AM processes.

Finite volume methods have also been used to attempt the prediction of the L-PBF process. Yuan and Gu (2015) modeled the process using finite volume methods via commercially-available software (Ansys FLUENT) to simulate a ceramic composite L-PBF process, which included Marangoni shear stress to drive the fluid flow of the molten pool, but neglected evaporation from the powder bed or substrate material. Since the matrix considered was an aluminum alloy with low molecular weight constituents, evaporation and recoil pressure needed to be considered in their analysis (Miyagi et al., 2018). Furthermore, the source term for solidification was either not included or insufficient to prevent motion of the solid phase, as results of their model showed non-negligible velocity away from the laser irradiation region. Lee and Zhang (2015) used Flow-3D, a commercially-available software package and used the volume-of-fluid method with a piecewise linear interface calculation for tracking the interface between the high density and low density phases. Even though they included effects of evaporation from the powder within their model and

could address keyhole formation with multiple beam reflection, they did not address energy absorption and attenuation from plasma which will occur when a keyhole is generated (Tan and Shin, 2014). A similar effort was undertaken by Qui et al. (2015a) via the inclusion of the same physical phenomena as (Lee and Zhang, 2015) using an open-source software package called OpenFOAM, but did not calculate multiple reflections within the keyhole. The following year, Lee and Zhang (2016) extended their analysis to perform a two-track simulation of an Inconel 718 powder bed on an Inconel 718 block substrate, but their analysis was insufficient in duration to allow for the molten pool to solidify, as they simulated a 1.0 mm long substrate preventing the full development of the molten pool region before the simulation was completed. Wei et al. (2017) modeled the L-PBF process using multiple powder diameters to provide a more realistic representation of the powder bed, but used a substrate thinner than a two-layer powder bed which limits heat transfer from the molten pool. Yan et al. (2017) simulated the L-PBF for single track deposition by tracking the heating of individual particles to predict balling defects; however, their analysis suffers from only being demonstrated on single-layer powder beds. Similarly, Wu et al. (2018) included a thin powder bed composed of multiple particle diameters, but did not provide sufficient laser power intensity to demonstrate the model could work on deeper keyhole formation even though their substrate thickness was large enough to reduce boundary-based effects. Shrestha and Chou (2019) were able to capture pore formation due to keyhole formation in both stable and unstable keyhole scenarios for a powder bed composed of multiple particle sizes, but had neglected plasma formation in their analysis. Each of the aforementioned attempts at modeling the L-PBF process were all limited to small domains (generally in the order of 1.0 mm), which limits the potential understanding of a practical process when building an AM component. Gan et al. (2019) demonstrated the latest in L-PBF modeling during an exposition associated with an additive manufacturing benchmark competition (Lyle and Levine, 2018) in which a single-layer powder bed of Inconel 625 was simulated using three different versions of numerical models: (1) conduction mode only, (2) a conduction model with fluid flow included, and (3) a conduction model with fluid flow and evaporation effects included. As assumed in previous work in literature regarding L-PBF, plasma formation and attenuation of the laser beam continued to be neglected.

The most prominent methodology described in the literature to model the L-PBF process is from researchers at Lawrence Livermore National Lab (LLNL), which uses an in-house developed software package called ALE3D to solve governing equations with a hybridized finite

element/finite volume technique (Khairallah and Anderson, 2014). In 2014, Khariallah and Anderson (2014) simulated a 316L stainless steel powder bed with a single layer of powder upon the substrate. In their analysis, they included melting and solidification phenomena, though had neglected evaporative effects since they were assumed to be relatively small compared to the energy being absorbed and reflected by the particles. At the time, their analysis required approximately 100,000 CPU-hours to simulate a scanning distance of 1.0 mm since an explicit time advancement scheme was used to solve the governing equations. Most recently, Shi et al. (2019) from LLNL simulated Ti-6Al-4V L-PBF using a single-layer powder bed on a thin substrate to predict the transient temperature field via ray-tracing energy addition, a recoil pressure model to include evaporation, and fluid dynamics due to Marangoni shear stress at the free surface of the liquid. Unfortunately, their analysis methodology being similar to the analysis from 2014 is expected to require a similar computational effort, thus is prohibitive in regards to the simulation of practical applications where thicker powder beds and/or substrates are used. To reduce computational effort, previous work has shown that full governing equations could be solved on a smaller region in close proximity to the phenomena being captured, while solving the energy equation on the remainder of the domain using a dual-mesh technique (Tan and Shin, 2014).

Deficiencies continue to remain regarding how to model the L-PBF process for large-scale parts. Commercial software packages currently need to be modified via user-defined functions to handle laser energy addition, DEM modeling, and complexity associated with high intensity laser irradiation energy sources. For researchers who build their own solvers, ray-tracing methods for energy addition are computationally limiting and do not scale well with thick powder beds. Instead, volumetrically-based energy addition allows simulation of pre-placed powder while simultaneously including phenomena such as evaporative effects and gas dynamics above the substrate. Having the capability to simulate with volumetric methods would enable more rapid simulation without significantly sacrificing computational accuracy of the L-PBF process, and would further allow the simulation of larger components and minimizing the effects of boundary conditions on the numerical solution. Such a solution methodology coupled with a dual-mesh solver would allow as-built AM components to be simulated without the need to use domains of limited size, as have been seen in previous literature.

1.3   Research Objective

The objective of this research is to provide insight into various additive manufacturing processes using numerical modeling tools which will predict deposited track geometry, molten pool shape and size, as well as heat-affected zone shape without using model tuning parameters. Specific goals of this research are as follows:

(a) Develop a numerical model to predict blown-powder laser-based additive manufacturing processes.

- The model must use physical powder and energy distribution to account for mass and energy addition during the process.
- The model must be adaptable for different materials through changes to temperature-dependent material properties
- The model must not use tuning factors for capture efficiency, but rather enable the calculation of capture efficiency from the prediction of the deposited mass upon the substrate

(b) Develop a numerical model to predict laser-based powder bed fusion additive manufacturing processes.

- The model must use physical powder and energy distribution to account for mass and energy addition during the process.
- The model must be adaptable for different materials through changes to temperature-dependent material properties.
- The model must not use tuning factors to describe physical processes, such as: melting/deposition of the powder bed, particle motion, and evaporation processes.

(c) All numerical models must be validated against experimental observation and be applied to practical examples to demonstrate the usefulness of the modeling approaches.

1.4   Thesis Outline

This dissertation is segmented into 4 chapters. Chapter 1 describes prior work in this particular field, and includes a literature review and the goals of this research. Chapter 2 provides an investigation into the application of modeling for blown-powder additive manufacturing systems by describing a framework to solve any powder feed mechanism via a systematic approach, enabling the removal of critical assumptions which have historically been utilized in the literature, such as those used for powder capture efficiency. Three case studies are presented to demonstrate the robustness of the model for different materials and blown-powder systems. Chapter 3 examines the principles of modeling for laser-powder bed fusion systems and application to modeling laser scanning processes. Also discussed in this chapter are two methods to reduce computational effort of the laser-powder bed fusion model: volumetric heat addition to the powder which prevents the need of computationally expensive ray-tracing models to describe particle heating, and a dual-mesh algorithm that mitigates the necessity to simulate the entire domain with fine mesh. A two-part case study is presented to demonstrate keyhole and molten bead formation in an instance where the laser irradiation source is static and in another case where the laser beam is scanning along the powder-bed. Finally, Chapter 4 outlines additional research which could provide additional value to the field of modeling and prediction of additive manufacturing processes, specifically by using machine learning concepts to increase model throughput.

CHAPTER 2.   BLOWN-POWDER ADDITIVE MANUFACTURING PROCESSES

This chapter describes the modeling effort to predict the product of blown powder-based processes. Previous models in literature required capture efficiency assumptions which prevent the use of using such models for predictive purposes. Instead, this modeling effort will be shown to provide a prediction of various processes without the need to explicitly describe the amount of powder being absorbed by the molten pool. Characterization of the nozzle and laser irradiation source is necessary to ensure source terms in the governing equations (which are shown extensively in literature) are portrayed accurately without the need for tuning factors. The method described herein is demonstrated through a series of case studies that have been validated against experimentation for different materials and blown powder processes.

2.1   Methodology

Blown-powder additive manufacturing is a highly complex process and requires care when attempting to characterize each of the sub-processes that is necessary to predict the result of such AM processes. To maximize the utility of any particular model for additive manufacturing, a standardized methodology is necessary to ensure that the physics of the process are being captured correctly and in a method that can be adapted readily, regardless of the materials being, the AM process parameters or even the equipment used for deposition. An overview of the solution methodology is provided in Figure 2.1, of which multiple aspects will be described in greater detail in subsections 2.1.1 through 0. The methodology is segmented into three main components: model inputs, solution, and post-processing. The model inputs include gathering information regarding powder and energy distribution, acquiring material properties, and assessing the boundary conditions (such as convection and radiation) which exist at the boundary between the metal and gas phases. Once these quantities are well-understood for the AM system being modeled, numerical simulation of the process can ensue using a computational fluid dynamics solver which allows calculation of molten pool dynamics, energy transfer through the substrate and phase changes at the boundary of the molten pool, in addition to molten pool shape tracking. The final step in the methodology is post-processing the data to generate critical information regarding the

geometry of the molten pool or deposited material, molten pool velocity distribution, or thermal history throughout the process which can be used to generate heating and cooling rate data for determination of phase transitions and transformations.
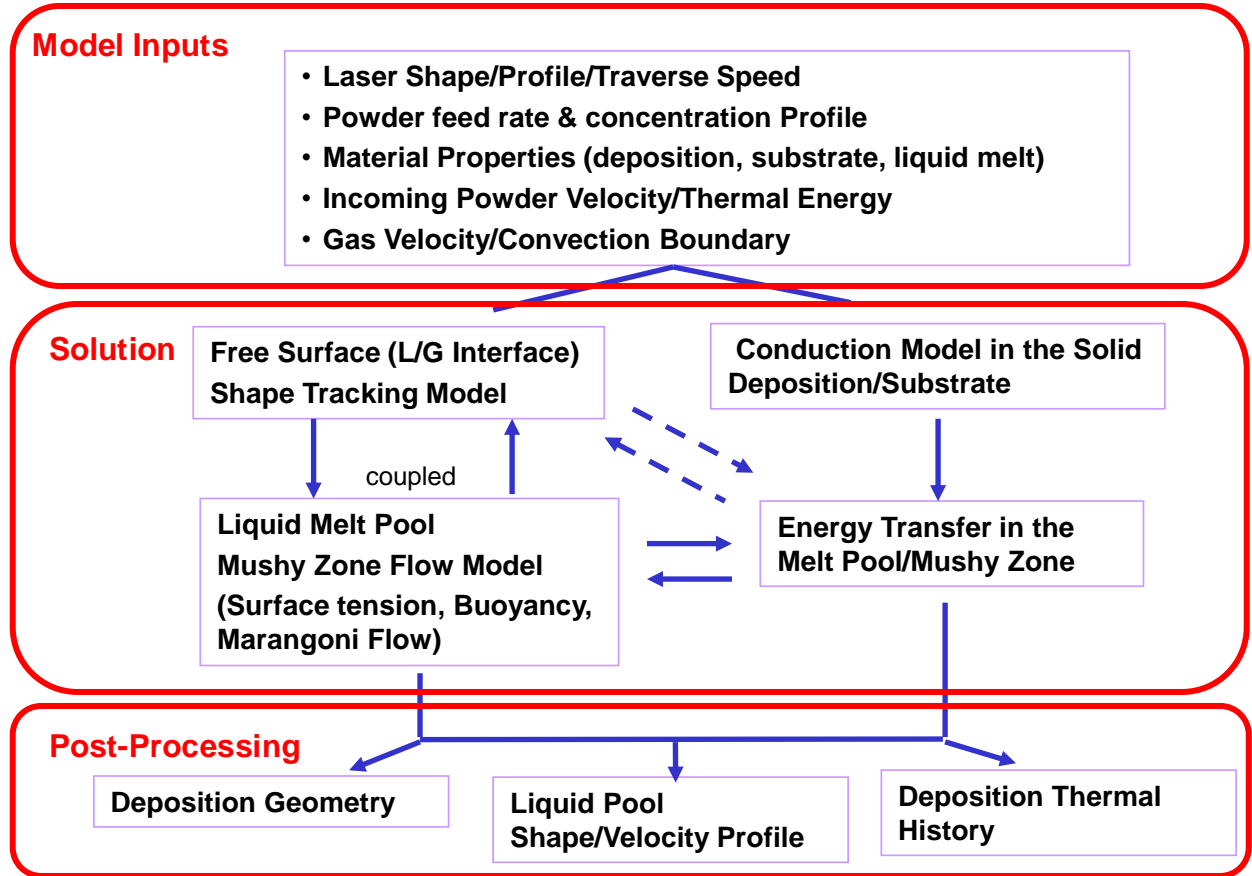
Figure 2.1: Solution flow diagram for blown powder AM processes

2.1.1 Modeling of the Deposition Process

For this study, LDD was modeled with governing equations for continuity, momentum, energy, and levelset, as shown in equations (2.1) through Eq. (2.4) (Wen and Shin, 2010, Wen and Shin, 2011, Katinas et al., 2019), with the levelset equation being used for free surface tracking due to mass addition.

$$\frac{\partial \rho}{\partial t} + \nabla \cdot (\rho \boldsymbol{V}) = S_{\text{mass}} \tag{2.1}$$

$$\frac{\partial(\rho \boldsymbol{V})}{\partial t} + \nabla \cdot (\rho \boldsymbol{V}\boldsymbol{V}) = -\nabla P + \nabla \cdot (\bar{\bar{\tau}}) + \boldsymbol{S}_{\text{mom}} \tag{2.2}$$

$$\frac{\partial(\rho h)}{\partial t} + \nabla \cdot (\rho \boldsymbol{V}h) = \nabla \cdot (k\nabla T) + S_{\text{energy}} \tag{2.3}$$

$$\frac{\partial(\rho \varphi)}{\partial t} + \nabla \cdot (\rho \boldsymbol{V}\varphi) = S_{\text{levelset}} \tag{2.4}$$

In equations (2.1) through (2.4), the quantities $t, \rho, \boldsymbol{V}, \boldsymbol{P}, T, \bar{\bar{\tau}}, k$ and h represent the time, local density, velocity, pressure, temperature, stress tensor, thermal conductivity and enthalpy, respectively. The parameter φ is a scalar quantity, called levelset, to describe the distance from the free surface, which is denoted by $\varphi = 0$. The last terms of equations (2.1)-(2.4) ($S_{\text{mass}}, \boldsymbol{S}_{\text{mom}}, S_{\text{energy}}$, and S_{levelset}) are mass, momentum, energy and levelset source terms for their respective equations. As mass is deposited and/or energy is added at the substrate surface, the source terms for each equation are updated to ensure the conservation of respective quantities. To simulate both convective and radiation heat losses at the free surface, an energy source term was included as part of equation (2.3). Equations for the source terms are shown as equations (2.5) through (2.8).

$$S_{\text{mass}} = (\rho_{\text{g}} - \rho_{\text{m}})\delta(\varphi)\frac{\partial \varphi}{\partial t} \tag{2.5}$$

$$\boldsymbol{S}_{\text{mom}} = -\frac{\mu_{\text{m}}}{K}\boldsymbol{V} - \boldsymbol{e} \cdot (\gamma \boldsymbol{n}\kappa - \nabla_{\text{s}}\gamma)\delta(\varphi) + \rho \boldsymbol{g}\beta(T - T_{\text{r}}) + \boldsymbol{V}(\rho_{\text{g}} - \rho_{\text{m}})\delta(\varphi)\frac{\partial \varphi}{\partial t} \tag{2.6}$$

$$\begin{aligned} S_{\text{energy}} = &\left(\alpha q''_{\text{laser}} + q''_{\text{powder}} + h_{\text{c}}(T - T_0) - \sigma\varepsilon(T^4 - T_0^4)\right)\delta(\varphi) \\ &+ \left(\rho(h_{\text{g}} - h_{\text{m}}) + h(\rho_{\text{g}} - \rho_{\text{m}})\right)\delta(\varphi)\frac{\partial \varphi}{\partial t} \end{aligned} \tag{2.7}$$

$$S_{\text{levelset}} = -\rho F_p|\nabla\varphi| + S_{\text{mass}}\varphi \tag{2.8}$$

where ρ_{g} and ρ_{m} are the density of gas and metallic phases, respectively, $\delta(\varphi)$ is the Dirac Delta function to allow source terms to be distributed across the interface, μ_{m} is the viscosity of liquid metal, K is the isotropic permeability of liquid through a porous medium, $\boldsymbol{e}$ is the unit vector, γ is the surface tension, $\boldsymbol{n}$ is the normal vector, κ is the free surface curvature, $\boldsymbol{g}$ is a vector denoting gravitational direction, β is the thermal expansion coefficient, T_{r} is a reference temperature,

$\alpha q''_{laser}$ is the net absorbed laser intensity, α is the material absorptivity, q''_{powder} is the energy flux introduced by the powder addition, h_c is the convective heat transfer coefficient, σ is the Stephen-Boltzmann constant, ε is the material emissivity, T_0 is the ambient temperature, h_g and h_m are the gas and metallic phase enthalpies, respectively, and F_p is the velocity of the free surface due to mass addition. Physically, the last terms in equations (2.5) through (2.7) describe the displacement of the gas phase with the deposited metal powder. In equation (2.6), the first term is associated with the flow of a solid-liquid mixture with the Carman-Kozeny equation, while the second term describes the free surface forces (surface tension and Marangoni shear). In the energy source, the first term includes surface contributions from laser energy addition, powder addition, convection, and radiation, respectively; while the second term describes the displacement of energy both from mass and enthalpy change during the addition of mass. Derivation of the source terms of the LDD process can be found in (Wen and Shin, 2010).

At the end of simulating three tracks upon reaching the pseudo-steady state, the temperature field was extracted and temperature profiles along the laser scan direction were developed which allowed for the calculation of both heating and cooling rates for a given location within the track. The temporal rate of temperature change was determined from the temperature field using equation (2.9), via utilization of the chain rule as:

$$\frac{dT}{dt} = \frac{dT}{d\boldsymbol{x}} \frac{d\boldsymbol{x}}{dt}\bigg|_{laser} \tag{2.9}$$

where T is the temperature at a given location in the domain and $\boldsymbol{x}$ is the spatial vector. To calculate the cooling or heating rate, the spatial temperature derivative in the direction of the laser scan direction is multiplied by the laser scan velocity. It should be noted that this calculation requires that the temperature field gradient be oriented in the same direction as the laser scan direction; otherwise, the resulting quantity has no physical relevance. Furthermore, this method of calculating the cooling/heating rate requires that the temperature profile remains unchanged at each incremental movement of the laser source (i.e. pseudo-steady temperature profile must be obtained).

2.1.2 Powder Concentration Profiling

In the previous section, each governing equation was shown to be influenced by the change in the free surface, and is subsequently driven by the laser energy and powder available at the gas-metal interface. To quantify the powder distribution, a computational fluid dynamics study was performed on a representative powder used within the Optomec LENS 750. In this particular study, particles of H13 powder were sieved to acquire a measurement on the size distribution such that a discrete phase model (DPM) could be implemented with minimal assumptions. The goal was to be able to develop transferable knowledge for a variety of studies once a given nozzle was characterized.

A sample of 516.296 g of H13 powder from Carpenter Powder Products (Micro Melt H13 powder {-170+325 mesh}) was manually sieved through four mesh sizes (45 μm, 75 μm, 90 μm and 150 μm) to acquire the mass within each size range.

Table 2.1 provides the mass distribution of the tool steel particles from the sieve analysis. The mass fractions were fitted to a Rosin-Rammler distribution (ANSYS, 2009), as shown in equation (2.10):

$$Y_d = e^{-(d/d_c)^n} \qquad (2.10)$$

where d_c is the mean particle diameter (corresponding to Y_d=36.8%) and was found to be 88 μm, and n is the distribution spread factor which was calculated to be 10.75. Approximately 1.1g (or 0.2%) of the powder mass is unaccounted for by the sieving; however, the amount of mass lost would minimally impact the mass distribution calculated by equation (2.10). Figure 2.2 shows representative particles from each size range collected after sieving by viewing under an optical microscope (Nikon Eclipse LV150) at 5x magnification with identical magnification used for each image. For each size of particle collected, it can be seen that the approximate shape of each is similar, allowing for a constant shape factor, or the departure of the average particle shape from spherical, as a function of particle size.

Table 2.1: Mass distribution of H13 powder based on sieve analysis

Size (μm)	Mass Collected (g)	% Mass
x >150	0.038	0.007%
90 < x <150	140.766	27.323%
75 < x < 90	348.791	67.701%
45 < x < 75	20.012	3.884%
x < 45	5.586	1.084%
Total	**515.193**	

The nozzle being studied in this analysis is the factory-installed quadruple nozzle of the Optomec LENS 750 machine. Figure 2.3 provides scaled pictures of the nozzle head containing four radially symmetric powder nozzles, and a center nozzle through which shielding gas is forced. Powder nozzles are each angled approximately 23.2 degrees from the laser beam axis. The flow path through the nozzles starts at 2.5 mm in diameter and tapers to an outlet diameter of 1.0 mm over a distance of 24.6 mm. The origin for the x-coordinate used in all figures is displayed in the side view and is zero at a plane corresponding to the four nozzle outlets.
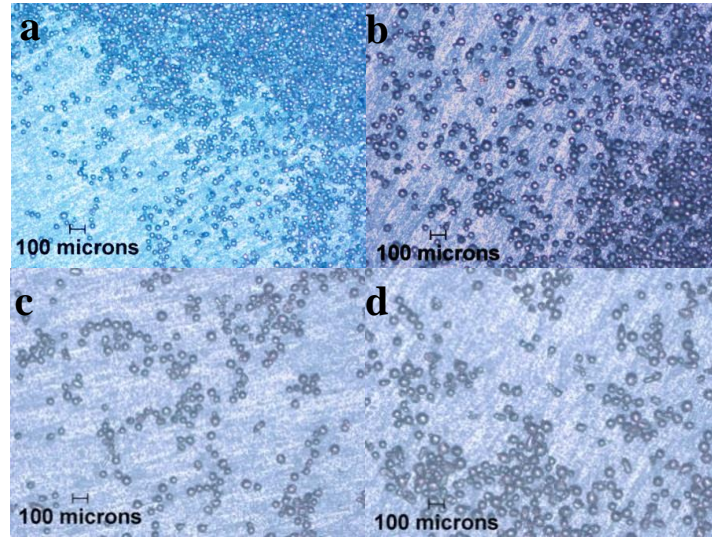
Figure 2.2: H13 particle shapes at (a) <45 μm, (b) 45 μm < x < 75 μm, (c) 75 μm < x < 90 μm, and (d) 90 μm < x < 150 μm
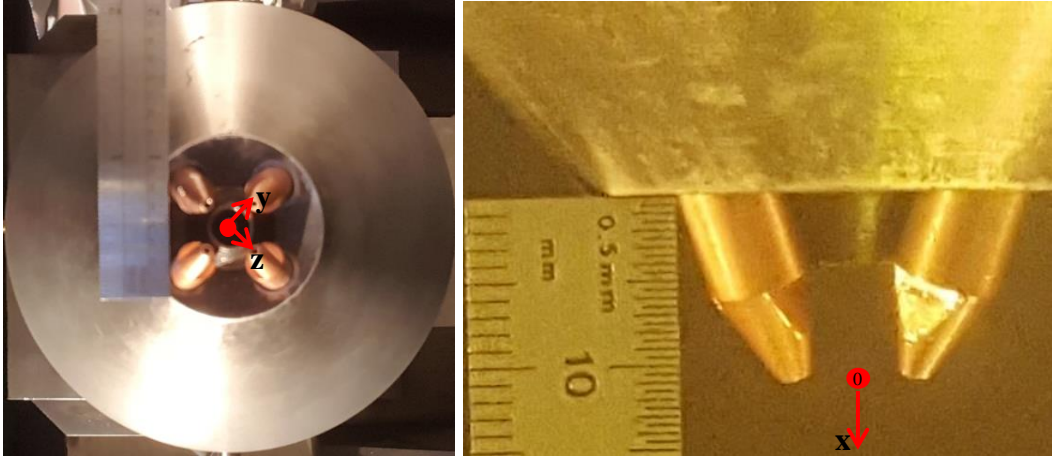
Figure 2.3: Optomec LENS 750 nozzle geometry with coordinate axes labeled– bottom view (left) and side view (right)

A total of four experiments were performed to understand the impact of particle dynamics for two powder mass flow rates in both free stream and substrate impingement scenarios. Free stream particle trajectories are typically not used in standard manufacturing processes, since it denotes a lack of substrate being deposited on; however, results from such experimentation provide insight into the location of the first interaction of powder particles and the substrate. Impingement experimental data is representative of the deposition process since particles will reflect off of the substrate and can potentially land on the top of the molten pool.

During experimentation, the gas flow rate for both the shielding and assist gas was held constant at 13 standard liters per minute (SLPM), with 4.5 SLPM being diverted specifically for particle propulsion through the four powder feed nozzles. Although the typical carrier gas within the Optomec LENS 750 system is argon, particle tracking velocimetry (PTV) experimentation required the chamber to be exposed to atmospheric conditions, which requires adjustment when developing predictions of the powder distribution during deposition in an oxygen-depleted environment. A series of calibration experiments were performed to ensure the mass flow rate of particles from the nozzles could be quantified, and the two mass flow rates used were 9.84±0.02 g/min and 6.55±0.15 g/min, for hopper motor speeds of 7.5 rpm and 5.0 rpm, respectively.

A diagram for the setup of the PTV equipment is shown in Figure 2.4. The laser sheet was generated using a Quantel USA pulse laser (532 nm) controlled by a Quantum Composers Model 9518 pulse generator. An Imperx ICL-B4020M-KF000 digital camera with a Nikon AF Micro

Nikkor 105mm 1:2.8 D lens captured images based on a trigger from the pulse generator. The laser sheet illuminated the $z=0$ plane which crosses the centers of the two out-of-plane nozzles. A pulse spacing of 35 µs was utilized such that at least 10 pixels of particle travel could be observed in the region of interest between adjacent images. Calibration of the image window resolution was performed using a Newark Resolution RES-1 Target, providing a scaling factor of 46 pixels per millimeter. An in-house developed PTV software was used to analyze the velocity of each captured particle (v) by determining its travel distance, Δx, such that $v=\Delta x/\Delta t$, where Δt is the time between images (35 µs).
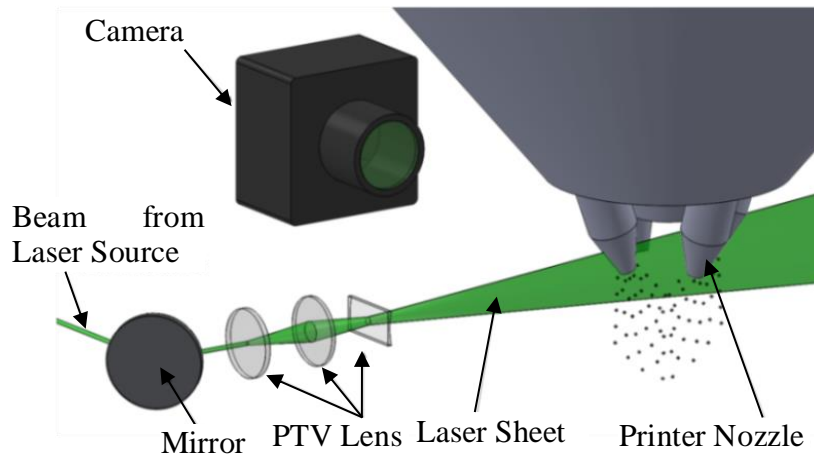
Figure 2.4: Experimental setup of PTV equipment

Upon capturing 880 images at each experimental condition, the particle velocity field was acquired by assigning a velocity at each particle location. Figure 2.5 shows the obtained particle velocity field in a free stream particle flow scenario at a powder mass flow rate of 9.84 g/min by agglomerating all 880 images to increase particle density for better visualization. In free stream flow, particles travel in the downwards direction regardless of the originating nozzle, and thus, they can be identified via directionality of the trajectory and are ignored in the event that the velocity vector points toward the nozzles. To more clearly observe the origin of each particle, the velocity vectors have been color coordinated based on the nozzle from which the particle was ejected, with the red vectors denoting particles from the combination of both out-of-plane nozzles. Additionally, a contour plot of the average velocity magnitude over 16x16 pixel areas was created and shows the highest velocity magnitude to be associated with particles along the nozzle axis.
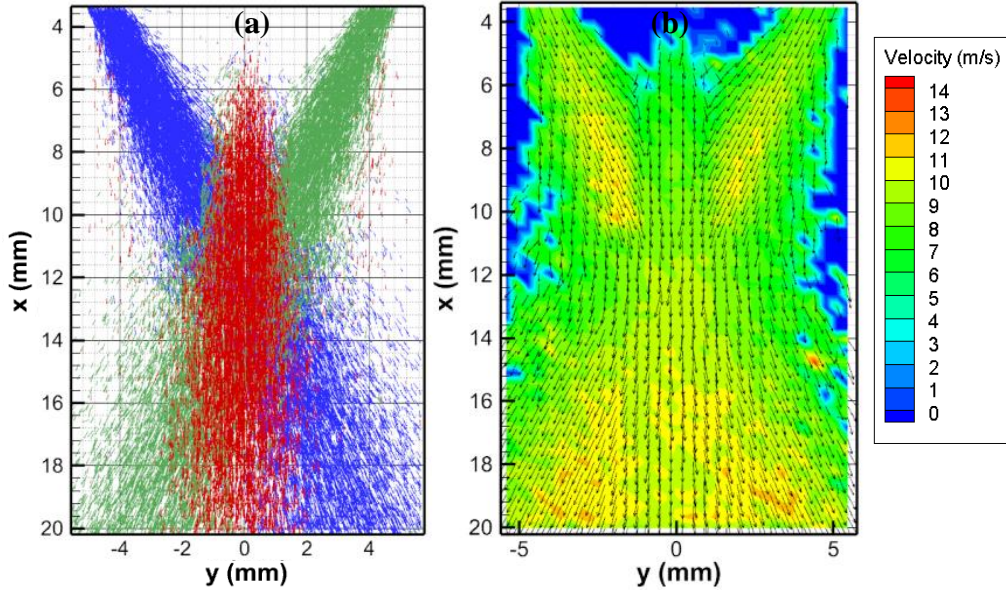
Figure 2.5: Particle velocity field for free stream experimentation at 7.5 rpm hopper speed – (a) individual particles colored by an originating nozzle, (b) average overall particle velocity field

In the impingement case, however, once a particle has impacted the substrate, it will deflect based on the interaction between the particle and the substrate, whether it is a full or partial reflection from the surface. In the region adjacent to the substrate, PTV was unable to capture a reasonable trend due to the particle scatter at the impingement point, though, based on observation during experiments, powder reflection prevented accumulation adjacent to the molten pool, indicating that only powder particles which have trajectories directly from the nozzles to the molten pool need to be considered. For particle and gas properties similar to those used in this experimentation, Wen and Shin showed that particles are not influenced by the gas velocity field, indicating that trajectories can be obtained from free stream simulation data at the corresponding stand-off distance (Wen et al., 2009).

Figure 2.6 depicts a diagram of the interaction of the particles emerging from the out-of-plane nozzles with the laser sheet. The laser sheet resides within the x-y plane; hence, PTV provides a cross-sectional view of the in-plane powder nozzles, while only providing a limited view of the particles emerging from the two out-of-plane nozzles. Only select particles from the four nozzles will interact with the laser sheet, and thus, a slice of the particle cloud with finite thickness is collected from the experimental data. The thickness of the slice can be determined by

the extent in which out-of-plane nozzle particles can be observed in the PTV imagery. For example, in Figure 2.5, few particles above x=6.0 mm were observed in experimentation. Since the laser sheet thickness is less than that of the entire nozzle, only particles below a certain x-coordinate will interact with the laser sheet, as indicated in Figure 2.6. By modeling the spread of particles that emerged from the two in-plane nozzles (since out-of-plane nozzles do not interact with the nozzle sprays from the two in-plane nozzles), and using the same parameters for both of the out-of-plane nozzles, slices of the particle concentration may be obtained at various planes parallel to the laser sheet. Correlation of the laser sheet thickness to the experimental data is performed by assessing the concentration of particles that were detected by the laser sheet and comparing against the modeled version of the same system.
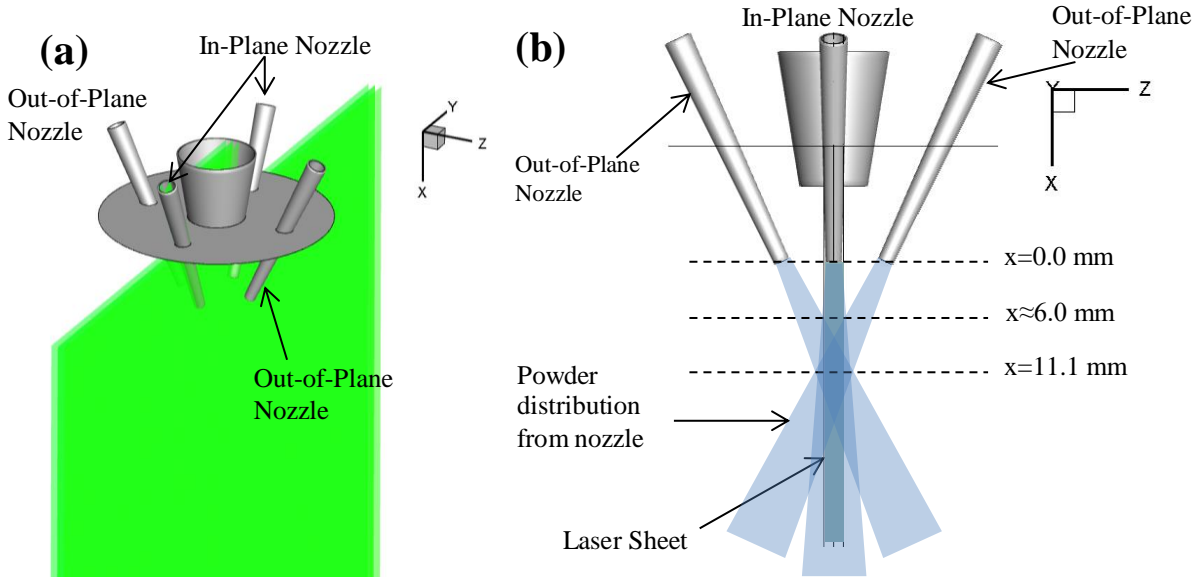
Figure 2.6: Detail of particle interaction with laser sheet (a) isometric view (b) side view

Particle concentration can be obtained from the experimental results by counting the average number of particles within an 8x8 pixel window over the 880 images and calculating a weighted density based on a linear ratio between the volume of free air contained within the laser sheet and the volume of spherical particles with the density of tool steel. Diameters of the individual particles were determined using the number of pixels illuminated for a given particle, and calculating the diameter (in pixels) assuming an equivalent circular cross-sectional shape using

the scaling factor. Each pixel of the high-resolution images corresponded to 23 μm, which provided sufficient resolution to capture particle diameters which measure between 45 μm and 150 μm. Figure 2.7 depicts the particle concentrations calculated from the experimental data of the free stream scenario at a 9.84 g/min powder feed rate.
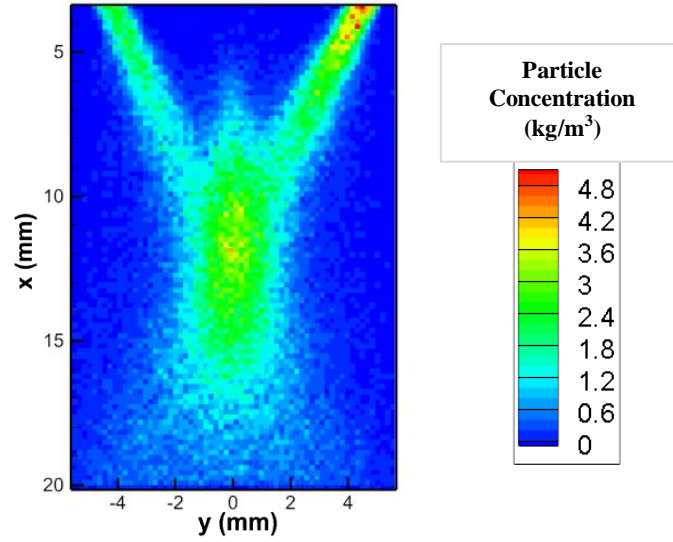
Figure 2.7: Particle concentration for the free stream at 9.84 g/min

Analysis

The governing equations describing the bulk fluid flow within the domain are given by continuity, momentum, and turbulence. In addition, a discrete phase model is used to account for the effect of local velocity on the metal particles. Because this physical system is turbulent in nature and turbulence is a three-dimensional phenomenon, all governing equations presented require a solution in a three dimensional domain, which are solved by using Ansys FLUENT (ANSYS, 2009).

Governing equations for continuity and momentum are shown in equations (2.11) and (2.12) (Wen and Shin, 2010), respectively

$$\frac{\partial \rho}{\partial t} + \nabla \cdot (\rho \boldsymbol{V}) = 0 \tag{2.11}$$

$$\frac{\partial(\rho \boldsymbol{V})}{\partial t} + \nabla \cdot (\rho \boldsymbol{V}\boldsymbol{V}) = -\nabla \boldsymbol{P} + \nabla \cdot (\bar{\bar{\tau}}) + \boldsymbol{S}_{dpm} \tag{2.12}$$

where $\bar{\bar{\tau}}$ is the stress tensor as shown in equation (2.13), $\boldsymbol{P}$ represents the pressure, and S_{dpm} is the force coupling from the discrete phase model. It is assumed that due to the low concentration of particles with respect to the gas, the one-way coupling is valid, and thus the gas affects the discrete phase, not vice-versa (i.e. $\boldsymbol{S}_{dpm} = 0$).

$$\bar{\bar{\tau}} = \mu \left[(\nabla \boldsymbol{V} + \nabla \boldsymbol{V}^T) - \frac{2}{3} \nabla \cdot \boldsymbol{VI} \right] \qquad (2.13)$$

In equation (2.13), μ is the viscosity and $\boldsymbol{I}$ is the identity matrix.

A standard k-ε turbulence model is utilized to capture time-average flow fields, as was developed by Launder and Spalding (Launder and Spalding, 1974), and is provided in equations (2.14) and (2.15)

$$\frac{\partial(\rho k)}{\partial t} + \frac{\partial(\rho k u_i)}{\partial x_i} = \frac{\partial}{\partial x_j} \left[\left(\mu + \frac{\mu_t}{\sigma_k} \right) \frac{\partial k}{\partial x_j} \right] + G_k + G_b - \rho \varepsilon - Y_M + S_k \qquad (2.14)$$

$$\frac{\partial(\rho \varepsilon)}{\partial t} + \frac{\partial(\rho \varepsilon u_i)}{\partial x_i} = \frac{\partial}{\partial x_j} \left[\left(\mu + \frac{\mu_t}{\sigma_\varepsilon} \right) \frac{\partial \varepsilon}{\partial x_j} \right] + C_{1\varepsilon} \frac{\varepsilon}{k} (G_k + C_{3\varepsilon} G_b) - C_{2\varepsilon} \rho \varepsilon \frac{\varepsilon}{k} + S_\varepsilon \qquad (2.15)$$

where coefficients $C_{1\varepsilon}$=1.44, $C_{2\varepsilon}$=1.92, $C_{3\varepsilon}$=0.0, C_μ=0.09, σ_k=1.0 and σ_ε=1.3, based on default values in FLUENT since these parameters provide a reasonable estimation of turbulence for jet flows (ANSYS, 2009), G_b is the generation of turbulent kinetic energy from buoyancy, G_k is the generation of turbulent kinetic energy from average velocity gradients, S_ε and S_k are user-defined (both set to zero) and μ_t is the turbulent viscosity. Calculations of remaining source terms within the turbulence equations are documented in the FLUENT theory guide (ANSYS, 2009). Near-wall treatment is handled using enhanced wall treatment, which separates wall interactions into two layers based on a non-dimensional wall distance and using a blending function (Kader, 1981) to smoothly link the laminar and turbulent regimes together.

The discrete phase model is governed by the trajectory motion of point masses via a force balance as shown by equation (2.16) (ANSYS, 2009)

$$\frac{\partial u_p}{\partial t} = F_D(u - u_p) - \frac{g_x(\rho - \rho_p)}{\rho_p} + F_x \qquad (2.16)$$

where F_D is a velocity damping term including effects for the aerodynamic drag of a given particle and F_x includes additional particle body forces, which are zero for this study. The drag coefficient is a function of the particle size, shape, density, and viscosity of the working fluid, as shown in equation (2.17). Velocity values used to calculate the Reynolds number are based on the magnitude of the relative velocity between a given particle and the gas phase velocity.

$$F_D = \frac{18\mu_g}{\rho_d d_d^2} \frac{C_d Re}{24} \qquad (2.17)$$

Non-spherical particles were discovered upon inspection of the sieve analysis, and hence it is necessary to model the departure of simulated particle shapes from spheres. A shape factor is used to describe such non-ideality, as shown in equation (2.18):

$$\phi = \frac{A_{sph}}{A_p} \qquad (2.18)$$

where A_p is the surface area of the actual particles and A_{sph} is the surface area of a sphere with the same volume as the particle. Based on visual comparison as in the previous work (Wen et al., 2009) in addition to estimation of particle surface area and volume, a shape factor of 0.8 reasonably describes the H13 particles. The coefficient of drag must include the effect of non-spherical particles, and is shown in equation (2.19) (Haider and Levenspiel, 1989).

$$C_d = \frac{24}{Re}(1 + a_1 Re^{a_2}) + \frac{a_3 Re}{a_4 + Re} \qquad (2.19)$$

where

$$a_1 = \exp(2.33 - 6.46\phi + 2.45\phi^2) \qquad (2.20)$$

$$a_2 = 0.096 + 0.56\phi \qquad (2.21)$$

$$a_3 = \exp(4.91 - 13.89\phi + 18.42\phi^2 - 10.26\phi^3) \qquad (2.22)$$

$$a_4 = \exp(1.47 + 12.26\phi - 20.73\phi^2 + 15.89\phi^3) \qquad (2.23)$$

The Stokes number was calculated to understand the effect of gas velocity on H13 particles for the two size extremes, 45 μm and 150 μm, and were calculated based on equation (2.24)

$$St = \frac{u_o}{l_o} \frac{\rho_d d_d^2}{18\mu_g} \tag{2.24}$$

where d_d is the particle diameter, ρ_d is the particle density, μ_g is the dynamic viscosity of the carrier gas, u_o is the local gas velocity, and l_o is the characteristic length of an obstacle. For the smallest particle diameter (45 μm) of H13 with a density of 7835 kg/m^3, carried by air with a viscosity of 1.849e-5 kg/m-s and velocity of 10 m/s by a nozzle with the radius of 0.5 mm, the Stokes number is calculated to be 1.6e4, indicating the inertial effects are too large for the flow field to impact the particles.

Since the laser was deactivated during experimentation, the effect of the energy equation was assumed to be negligible for this system. Furthermore, due to the relatively low velocities of the shielding and assisting gas observed within the system, pressure effects on gas enthalpy due to stagnation can be neglected.

The equations described in this section are solved numerically using Ansys FLUENT (ANSYS, 2009), a commercially available software package. Several assumptions have been made to both reduce computation time and minimize model tuning parameters: (1) Particles are assumed to be dilute with respect to the gas phase, allowing the interaction of particles with each other to be neglected. Furthermore, the particles are assumed to have a Rosin-Rammler distribution (ANSYS, 2009), as discussed earlier. (2) Energy due to laser irradiation is not included since the laser was deactivated during experimentation. (3) Although the flow is turbulent in nature, the flow field is solved as steady-state turbulent flow, thus providing an average glimpse into the flow field. However, this does not impact the trajectory of individual particles since the Stokes number is several orders of magnitude larger than unity, indicating that particle inertia will overcome local drag force from the gas. (4) Since the pressure drop within the flow is relatively low and the velocity is significantly below the Mach number for air at room temperature, the gas phase is assumed to be incompressible.

The computational domain used in this study corresponds to the free stream case, and is composed of the four powder-carrying nozzles and the shielding gas nozzle with an attached gaseous region to allow for gas expansion upon exiting each of the nozzles. To minimize the computational domain, the gaseous region was truncated beyond 29.0 mm, or 2.6 powder nozzle focal distances based on the nozzle head geometry. This is reasonable since particles in the free stream case cannot reflect back into the domain and do not interact with each other. Boundary

conditions for the computational domain are shown in Figure 2.8. Wall boundaries within the nozzles are all assumed to be non-slip stationary walls that reflect metal particles without momentum loss. At the powder nozzle inlets, a velocity normal to each face has an imposed gas velocity magnitude of 5.04 m/s and a particle velocity of 10.5 m/s with an additional 0.3 m/s tangential velocity to allow dispersal of the powder stream upon exit. Particle velocities were determined based on imaging studies of particles leaving the nozzles. The shielding gas nozzle has a uniform inlet velocity of 2.08 m/s. Pressure boundary conditions are all imposed at 0 Pa gauge pressure. The domain was composed of 2.159e6 computational cells, with the majority being tetrahedral control volumes.
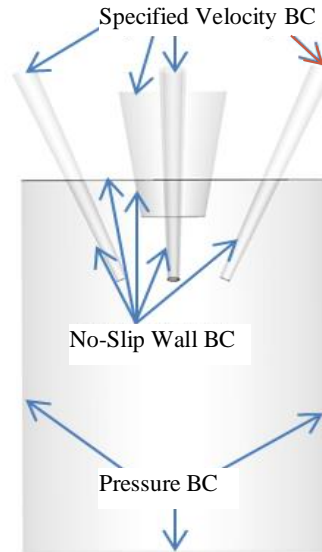
Figure 2.8: Boundary conditions for free stream domain

The smallest computational volume (located near the focal point of the nozzles) had a side length of 65 μm, while the largest had a side length of 0.43 mm and was located near the circumference of the domain. A grid independence study was performed by increasing the number of control volumes to 3.315e6 and showed less than 2% variation on the maximum gas velocity with a refined mesh.

The domain was initialized with a static velocity field (V=0), after which simulations continued until residuals stabilized below 1e-4 for continuity, 1e-6 for momentum, turbulent kinetic energy and turbulent dissipation, or until maximum velocity and average velocity near the focal point changed less than 0.025%, whichever occurred last. Prior to reviewing results, a final

discrete phase model update was performed to acquire the latest information regarding the powder concentration and velocity.

When observing the results obtained from PTV, particles from the two center nozzles can be seen entering the domain above the nozzle focal point, as was seen in Figure 2.5(a). It is believed the particles used in this experiment were reflective enough to scatter the illumination source within 2 mm of each direction of the vertical center plane (equivalent laser sheet thickness of 4mm). Consequently, comparison of simulation to experimental results requires an average particle concentration over the 4 mm effective laser sheet thickness.

To demonstrate the effect of effective laser sheet thickness, differences in the powder concentration profile can be seen by extracting slices from the simulation domain using parallel planes in 0.5 mm increments from the laser sheet center plane, as shown in Figure 2.9. Starting at approximately 1.0 mm from the laser sheet center plane, the influence from the out-of-plane nozzles can initially be observed, while slices farther from the laser sheet center plane are predominantly governed by powder flow from the out-of-plane nozzles.

Two methods of comparison with regards to the powder flow field can be utilized to assess the accuracy of the numerical model: particle velocity and particle concentration. Figure 2.10 provides a comparison of the experimentally acquired particle concentration and the modeled results averaged over the effective laser sheet thickness for the higher powder flow rate case of 9.8 g/min in free stream flow. The general trend of the powder concentration predicted by the model matches that observed in experimentation. At each nozzle, the powder concentration diminishes due to conical expansion of the powder jet, until convergence of the four nozzles begins to occur (at approximately x=10mm), at which point the powder concentration reaches a localized maximum near the powder focal point and finally continues to diminish. Two cross-sectional planes of the powder concentration profile have been extracted and are shown as subfigures (c) and (d). The powder concentration contour shown at 11.6 mm corresponds to the location of the averaged powder concentration focal point while the contour plot at 9.5 mm corresponds to the plane of a typical standoff used for this nozzle head during operation. Previous experimentation has shown that more stable and consistent depositions are observed at standoff distances less than the averaged powder focal point (Zhu et al., 2011), which is further validated with the local powder concentration being a maximum of approximately 2.1 mm from above the averaged powder focal point.
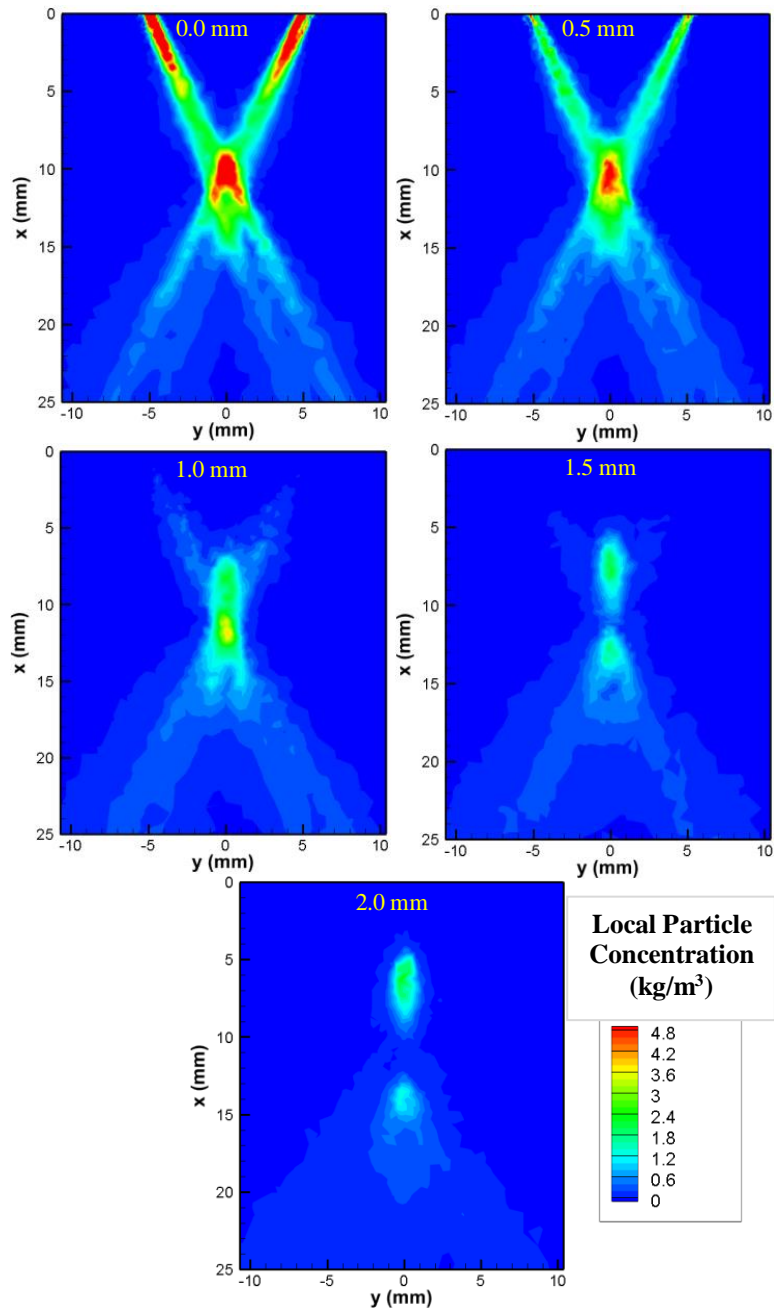
Figure 2.9: DPM concentration at nozzle head off-axis slices from 0.0mm to 2.0mm at 9.84 g/min powder feed rate
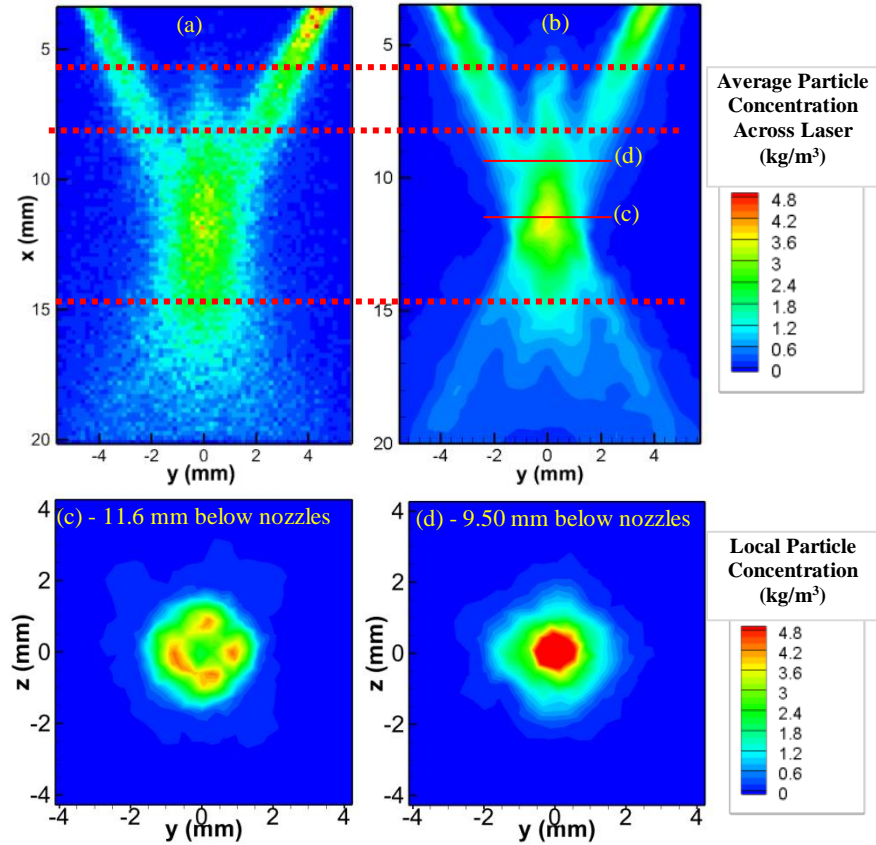
Figure 2.10: Comparison of (a) experimental particle concentration and (b) modeled concentration with extracted concentration contours at two locations (9.84 g/min)

Figure 2.11 depicts the experimental results and model prediction for powder flow in a free stream with a powder flow rate of 6.55 g/min. As seen in the higher powder flow rate, the powder concentration decreases upon ejection from the nozzles, and as the powder streams converge, the particle concentration rises. The maximum particle concentration predicted in the 9.84 g/min and 6.55 g/min powder flow models are 8.89 kg/m^3 and 5.96 kg/m^3 at locations 2.1 mm above the averaged focal point, respectively. The ratio of the maximum particle concentration and powder feed rate between the two cases is similar, indicating linearity of the particle concentration and the powder flow rate.
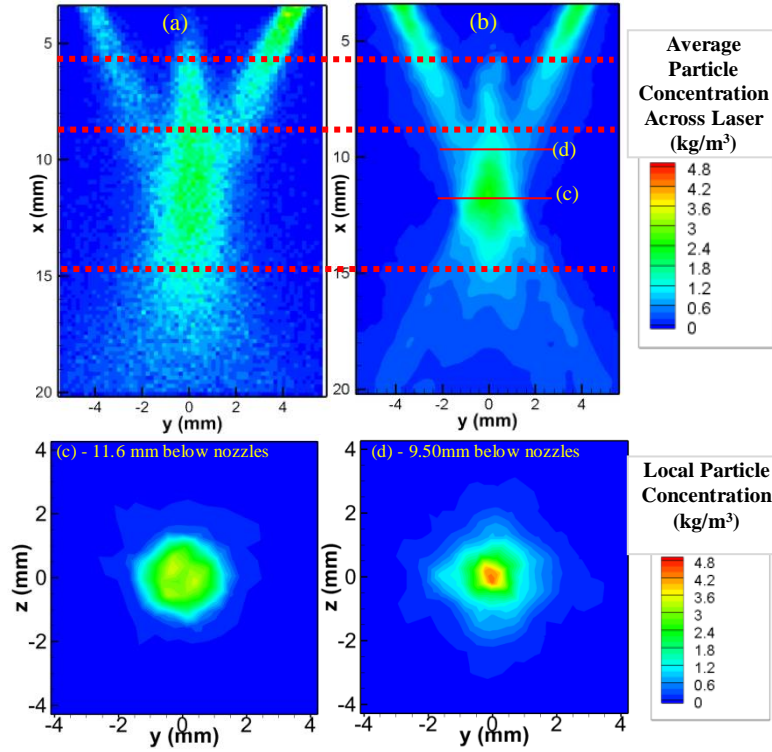
Figure 2.11: Comparison of (a) experimental particle concentration and (b) modeled concentration with extracted concentration contours at two locations (6.55 g/min)

A contour of the absolute difference of the powder concentration between experimentation and simulation was created in the powder focal region and plotted in Figure 2.12. From the error plots, the discrepancy is mostly scattered and random, with a maximum of 1.46 kg/m^3 for the higher feed rate (an average error is 0.394 kg/m^3) and 1.47 kg/m^3 for the lower feed rate (an average error is 0.338 kg/m^3). The checkerboarding pattern observed in the error plots is due to the pixelation of the experimental data.
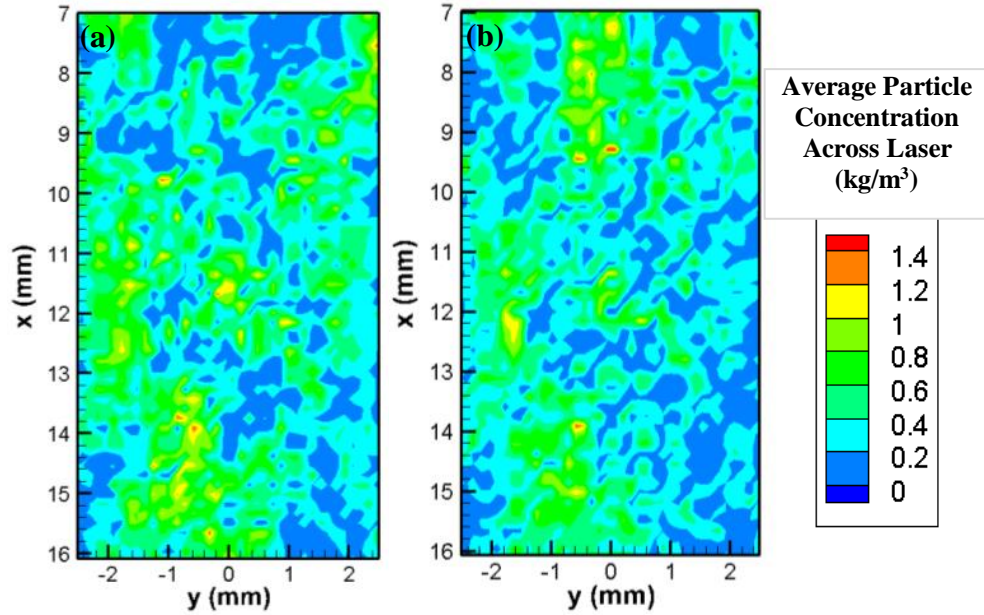
Figure 2.12: Error quantification of free stream cases - powder feed of 9.84 g/min (a) and 6.55 g/min (b)

To complete the information necessary for modeling of the deposition process, the particle velocity is compared against experimental results to assess general trends in the particle velocity field. Using a discrete phase model within FLUENT, path traces were investigated. Figure 2.13 shows the particle velocity field calculated from experimentation along with particle tracks colored by velocity. Although the velocity magnitude is of the same order of magnitude (approximately 10.8 m/s uniform velocity profile), trends at the focal point of the powder cannot easily be discerned. Since experimental results provided an averaged observed set of particles, whereas FLUENT provides a single average snapshot of the particles within the domain, comparison of the velocity fields remains qualitative.
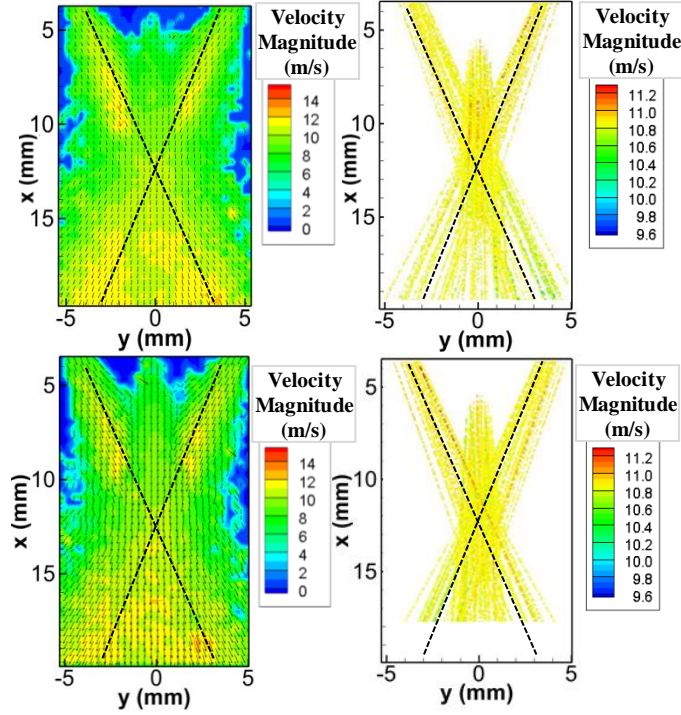
Figure 2.13: Particle velocity fields for free stream scenario at 9.84 g/min (top) and 6.55 g/min (bottom) powder feed rates

2.1.3 Laser Energy Distribution

Understanding the energy distribution from the laser beam is critical since it can affect the energy absorbance at the molten pool surface during the deposition process. Thus, a beam profilometer study was performed on the 500W IPG fiber laser on the Optomec LENS 750. The output of the profilometer measurements is an intensity profile in either a 2D or 3D graphics file, and is shown for one of the laser power settings (245 W) in Figure 2.14. The beam profilometer was unable to provide a text file with the laser intensity settings, so post-processing of the collected images was necessary.

Analysis of these images was performed using Matlab by reading in the colormap of the 2D image for each profile and plotted in a manner consistent with that from the original images. When colormap values were less than 20, the amount of laser irradiation indicated by the pixel was assumed to be zero. Results of the post-processing routine using the 4W profile are shown below in Figure 2.15. The beam was measured to have a diameter of approximately 600 μm at focus, which was subsequently used as the effective diameter for scaling the pixels into μm. The laser power per relative laser intensity count can be determined by summing the number of relative

laser intensity counts and dividing by the total laser power, as was plotted in Figure 2.16. This scaling value and the scaling value for distance per pixel can then be used to acquire the laser irradiation flux in power per square area. The post-processed results from the remaining laser power values can be found in Appendix A. Once the absolute intensities could be determined from the image, they were plotted on a scatter plot as shown in Figure 2.17 and a linear trendline was fit to the data to show the linear change of intensity when laser power is increased.
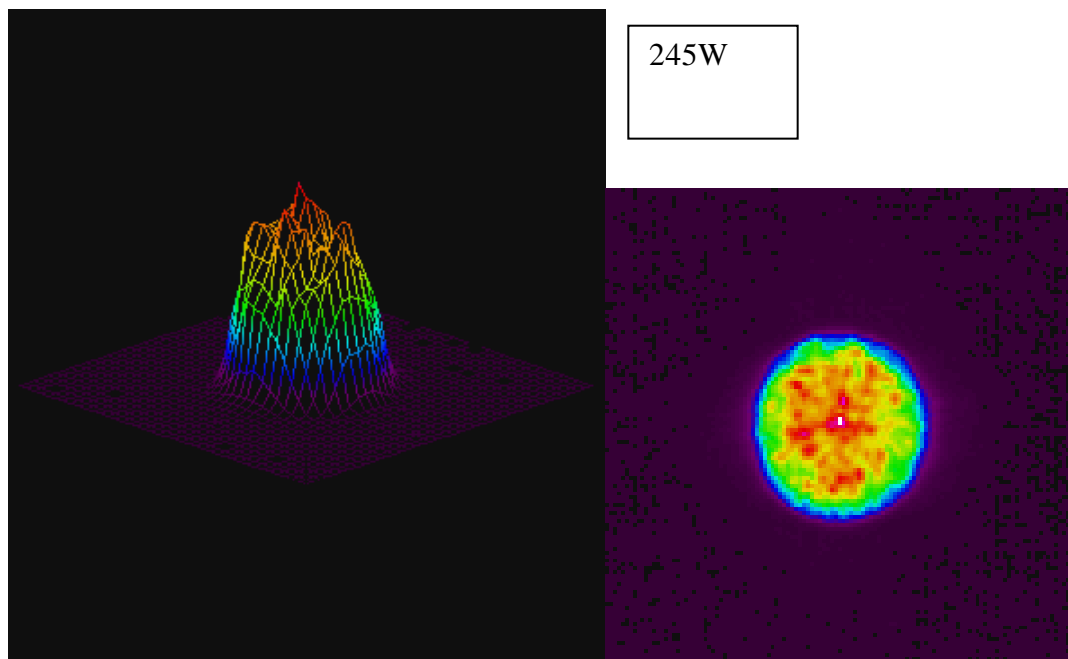
Figure 2.14: Intensity Profiles at 245W Laser Power

Original Images (4W)
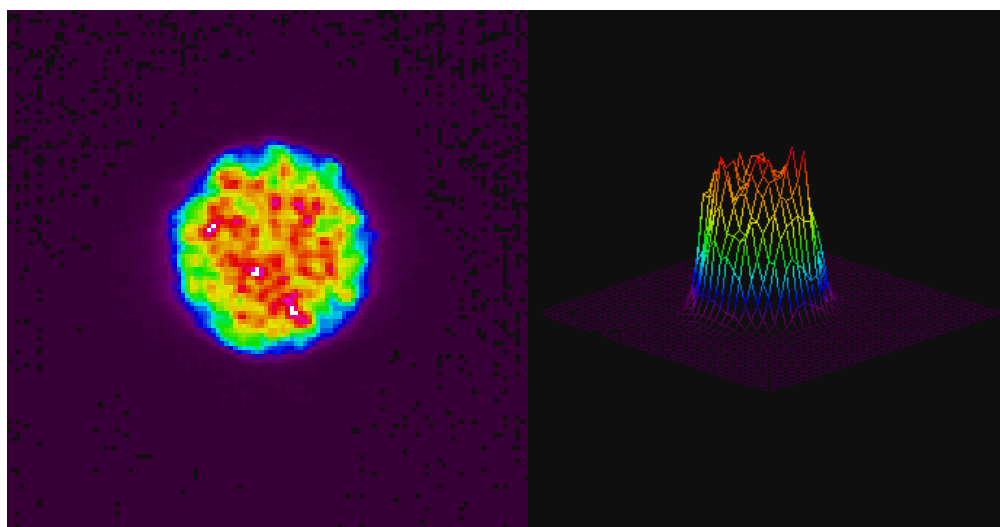
Matlab Interpretation (4W)
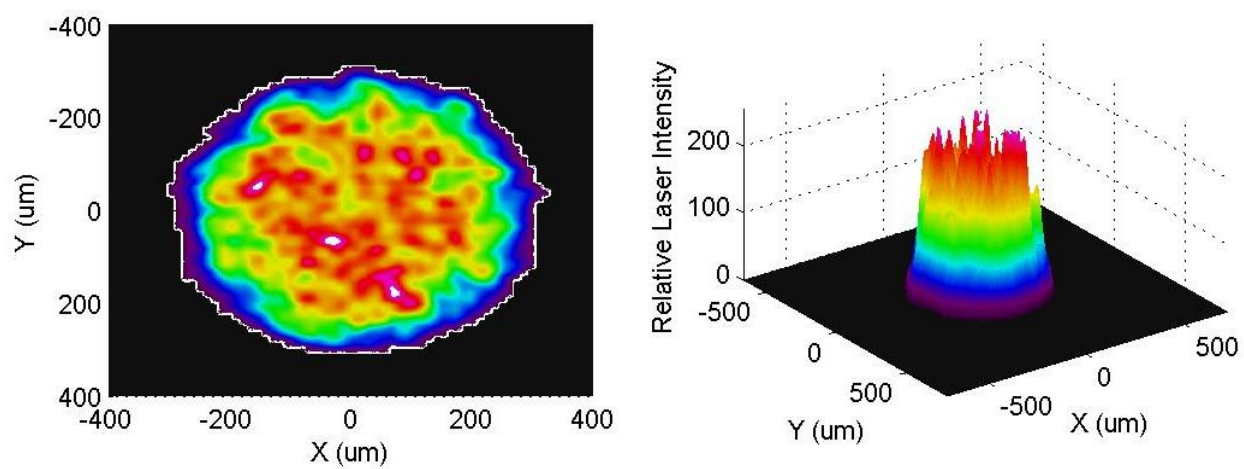
Figure 2.15: Pre- and Post-Processed Laser Profile
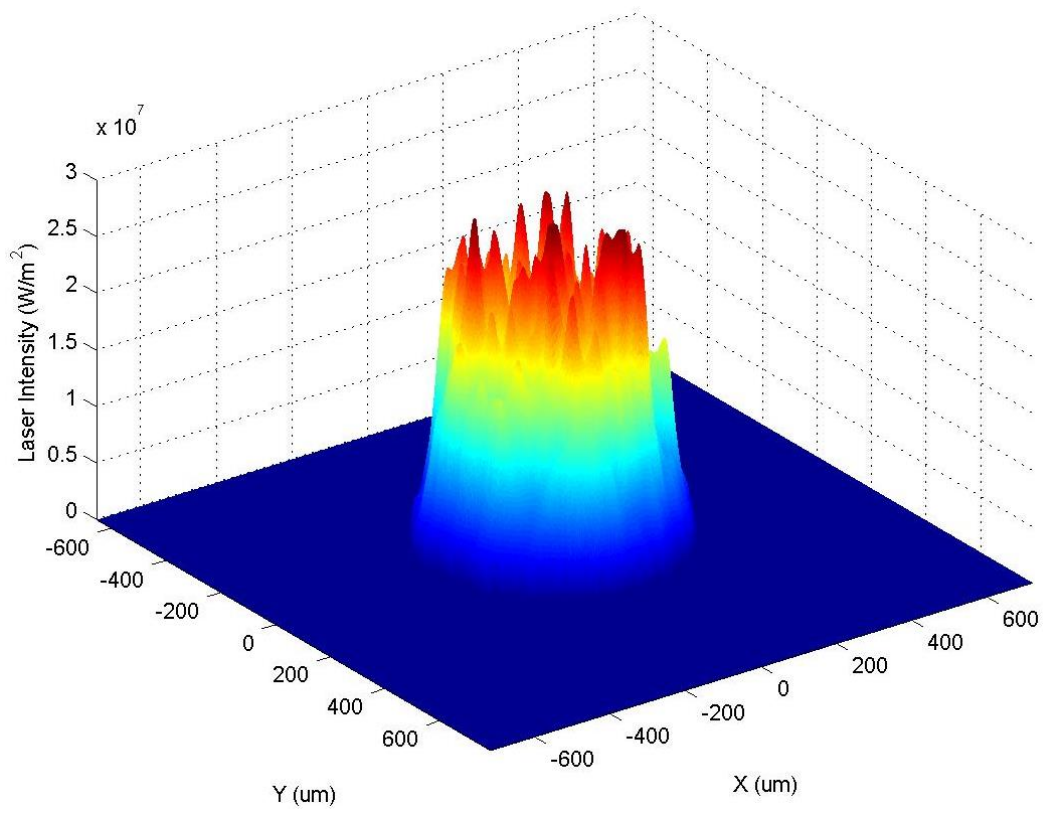
Figure 2.16: Laser Intensity Profile at 4W
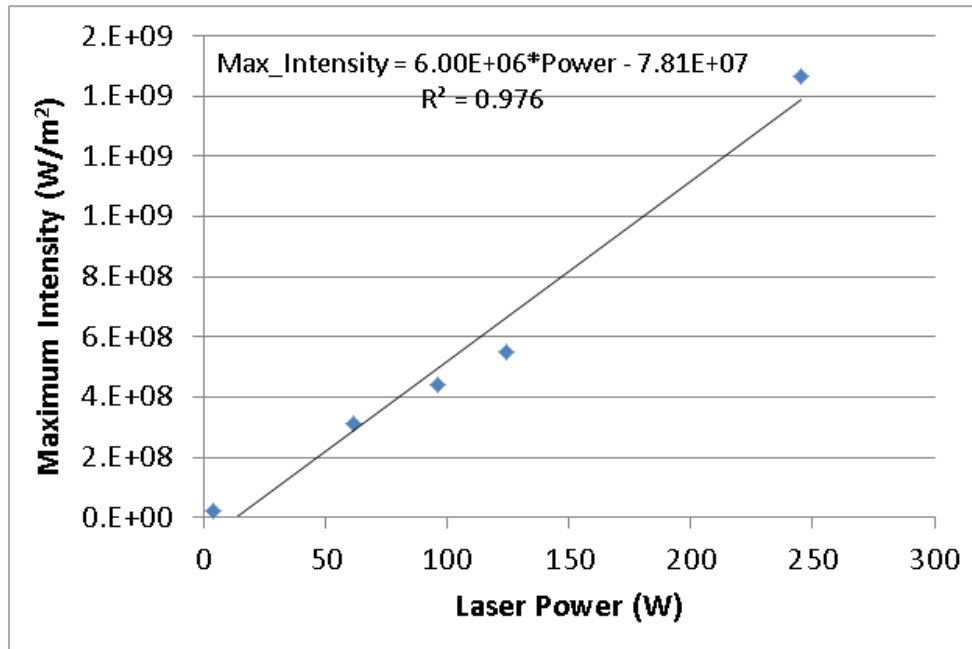
Figure 2.17: Maximum intensity plotted against laser power for IPG 500 W laser on Optomec LENS 750

Since the goal of the curve fitting is to produce a standardized curve regardless of the laser power and focus, the average circular profile needed to be created. Data from each of the beam profile measurements were normalized by dividing the laser intensity by the laser power of the corresponding test, and have been plotted on the same axes as shown in Figure 2.18. Next, an averaged normalized laser intensity was obtained by taking the mean of intensities at similar distances from the beam center across all laser powers. The 245W experiment shows behavior that is not expected at the laser beam center (sharp increase near the beam center), and is removed from the average since it is deemed to be an outlier.
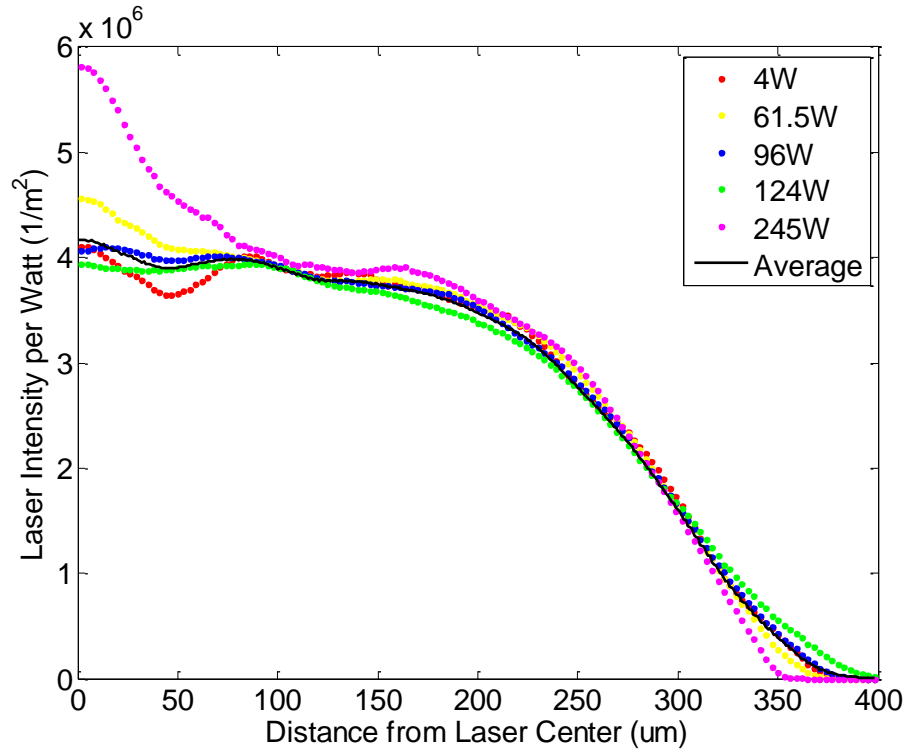
Figure 2.18: Laser Intensity Divided by Laser Power for All Beam Profiles, Average Excludes 245W

Using the average profile, a series of polynomial fits were performed to identify the lowest order polynomial which provided the highest fidelity with regard to the shape of the profile as well as providing a representation of the data with minimal oscillations. Figure 2.19 shows the four curve fits compared to the averaged data. The fifth-order polynomial was found to minimize the prediction error while maintaining a profile that resembles a "top-hat" laser profile.
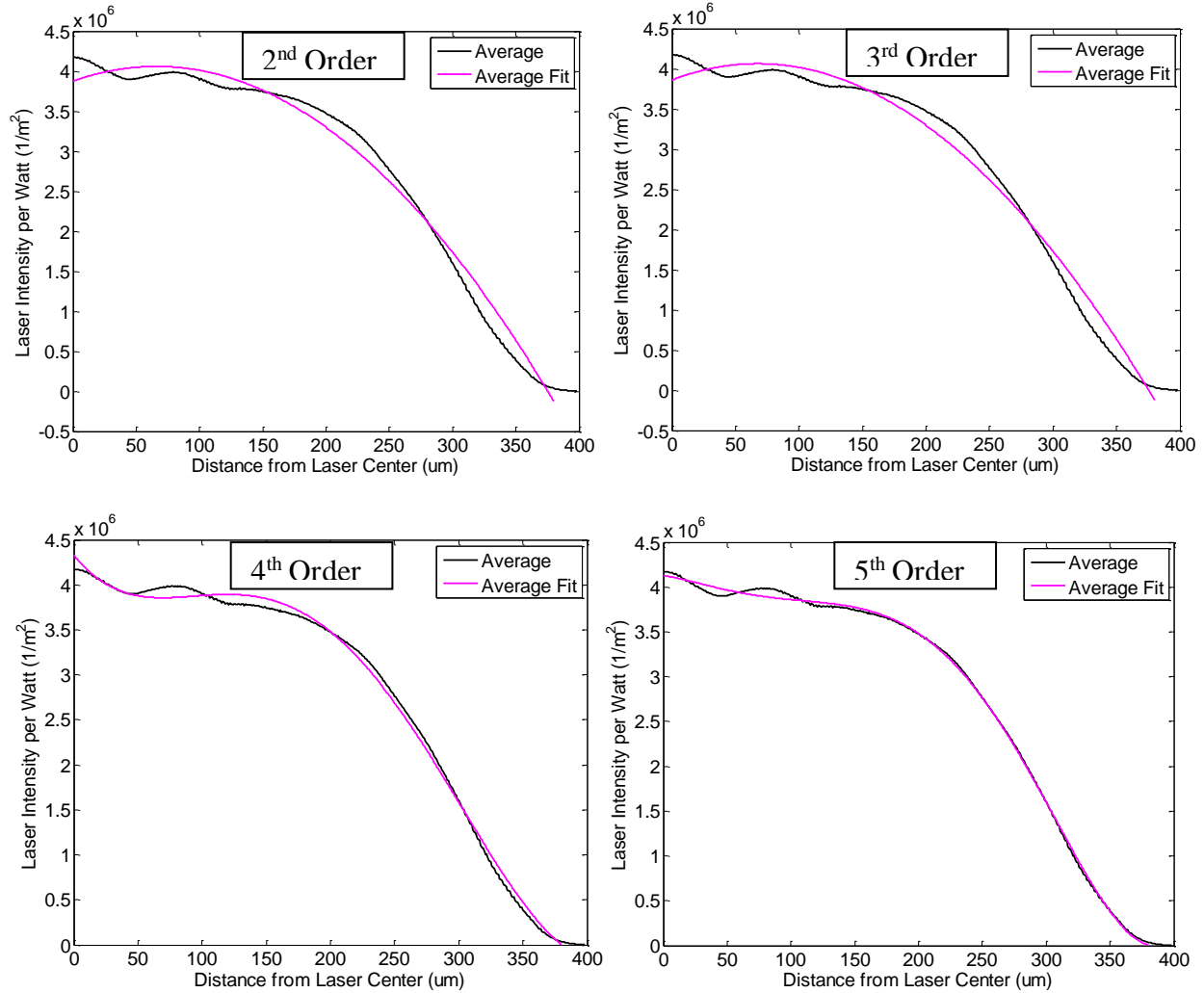
Figure 2.19: Polynomial fits to the averaged data (all except 245W data averaged) to quantify laser profile for IPG 500W laser on Optomec LENS 750

It was noted that the 61.5W and 4W experiments had significant intensity oscillations adjacent to the beam center. To understand the impact of these oscillations on the curve fit, these two data sets were also removed from the averaging, with Figure 2.20 showing a comparison of the fifth-order curve fits obtained depending on the data used during averaging. The difference between the two curves is essentially negligible at distances greater than 50 μm from the beam center. Curve fitting only the 96W and 124W yields a profile that remains constant near the beam center, which is the expected behavior of a top-hat profile beam. Hence, a fifth-order profile based on these two data sets averaged will be used for the polynomial profile for the 500W IPG fiber laser within the Optomec. For reference, Figure 2.21 shows all of the original data with the average profile of only the 96W and 124W laser power experiments.
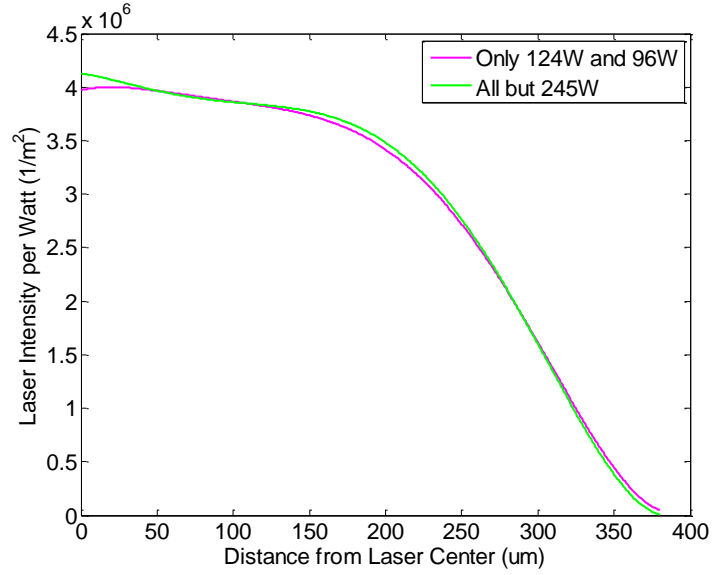
Figure 2.20: Curve Fit Dependence on Intensity Profiles Used for Averaging
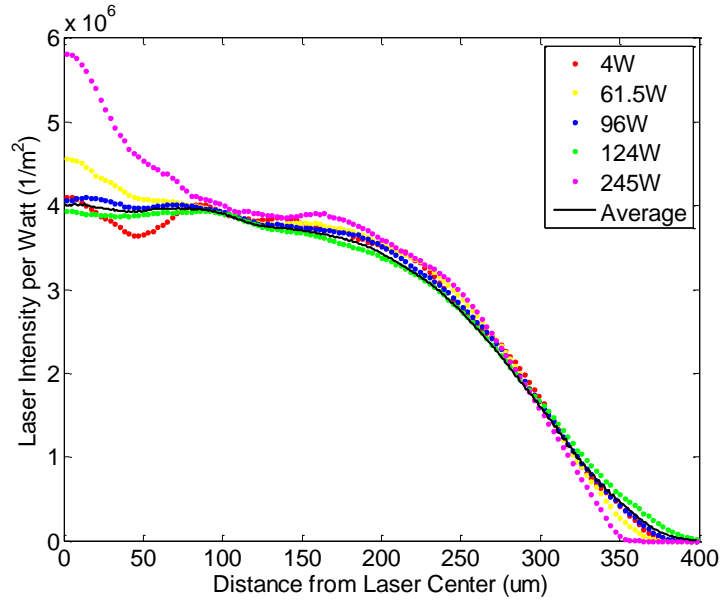
Figure 2.21: Normalized Laser Intensity for All Beam Profiles, Average Includes 96W and 124W

The best fit curve fit from using the 96W and 124W data can be described mathematically as:

$$(I[r]) = 5.3080e24r^5 - 3.9410e21r^4 + 8.0511e17r^3 - 5.0729e13r^2 \qquad (2.25)$$
$$- 2.2572e9r + 4.1284e6$$

where I is the normalized laser intensity at a distance r from the beam center axis, in meters. Using this average curve and removing the normalization, a comparison between the experimental data and the standardized shape from curve fitting can be compared, as displayed in Figure 2.22.
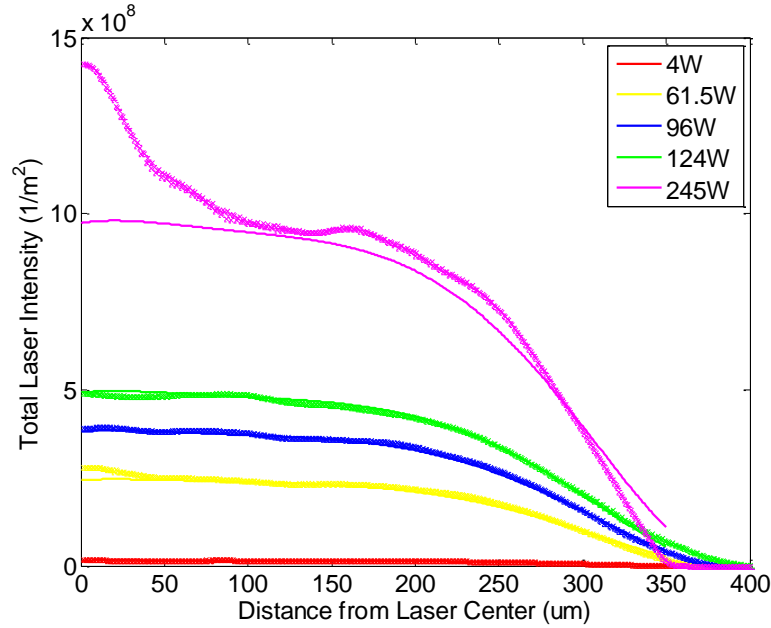
Figure 2.22: Comparison Between Curve Fitting and Experimentally Determined Profiles

The mean error associated with the fifth-order curve fits was 13.0% and was found when comparing the curve fits against the highest laser power (245W), as shown in Table 2.2. The average error for the remaining laser powers is less than 6%, providing evidence of high correlation for the curve fit selected.

Table 2.2: Average Error for Laser Intensity Curve Fit

Laser Power (W)	5th Order Fit
4	3.74%
61.5	5.51%
96	2.30%
124	1.82%
245	13.01%

2.1.4   Capture Efficiency Modeling

To handle capture efficiency of powder, a heuristic was implemented on the source terms of equations in section 2.1.1 to only allow the addition of incoming powder when the combination of the molten pool and the impinging powder mass have sufficient thermal energy to maintain a temperature above the liquidus temperature of the material. If this condition is not met, the powder is reflected. This is a reasonable assumption since non-melted powder will not be absorbed by the deposited tracks. Since the only material that could be added is above the surface of the substrate, the mass added to the system can be calculated using equation (2.26).

$$\dot{m}_{capture} = \rho v_\perp \int (H(x) - H_o) dx \qquad (2.26)$$

where $v_\perp$ is the feed rate velocity, $\dot{m}$ is the calculated mass captured, ρ is the density of the feed powder, and $(H(x) - H_o)$ denotes the height of the track at a given location along the cross-section. Once the captured mass is calculated, the capture efficiency can be determined via equation (2.27), by dividing the mass flow rate of captured powder ($\dot{m}_{capture}$) by the mass flow rate of feed powder ($\dot{m}_{feed}$).

$$\eta_{cap} = \frac{\dot{m}_{capture}}{\dot{m}_{feed}} \qquad (2.27)$$

2.2   Case Studies of Modeling Blown Powder AM

This section showcases the utility of the developed blown powder additive manufacturing model for different materials and blown powder operations. Each subsection below describes the methods and results for different materials or blown powder processes.

2.2.1   H13 Multi-track Deposition

Experimentation of the deposition process was performed using an H13 tool steel substrate with Micro Melt H13 powder. Operating parameters of the Optomec LENS 750 included a laser power of 350W with a laser waist diameter of 0.66 mm, scanning speed of 14.82 mm/s, and a powder feed rate of 8.5 g/min. The particle size of the H13 tool steel powder ranged between 50 μm and 150 μm. The laser and powder feeder nozzles move vertically on the Z-axis and are focused on an XY-table. The system is enclosed in an environmental chamber charged with argon

gas with an oxygen level below 20 ppm. The determination of the optimal LDD parameters of H13 powder is not the focus of this work, but the experimentally-determined optimal parameters for this deposition system are given in Table 2.3. These parameters are used in all experiments and simulations throughout this work.

Table 2.3: Optimal operating parameters for multi-layer LDD of H13 tool steel

Laser Power	350	W
Laser travel speed	35	in/min
Powder flow rate	8.5	g/min
Track spacing	0.300	Mm

A series of experimental validation images were collected with Figure 2.23 showing one representative track cross-section with the track geometry, and molten pool ($T_{solidus}$=1588 K) and heat affected zone ($T_{austenite}$=1023 K) boundaries accentuated. Similar images were collected for multi-track depositions, with details of the experimental procedure discussed in (Bailey et al., 2017).
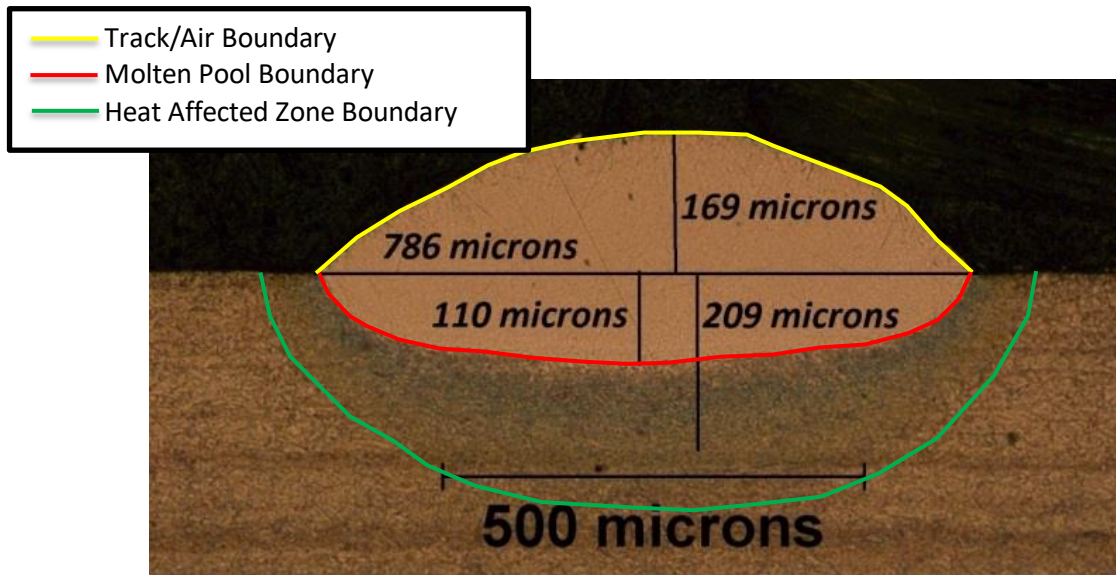
Figure 2.23: Cross-section view of single track H13 deposition

The computational domain consisted of a 12mm x 5mm x 12mm substrate composed of H13 tool steel to which H13 powder was being deposited via the LDD process. A total of 343,728

elements arranged in a structured mesh arrangement but with non-uniform grid spacing were utilized to obtain a numerical temperature field and surface profile. The thermal and physical properties of the H13 tool steel are provided in Table 2.4. The substrate was assumed to be initially at 300K, and convective boundary conditions were utilized at all faces of the steel substrate using a constant heat transfer coefficient of 10 W/m^2-K with an ambient temperature of 300K. To validate the model, a series of experiments were performed using an Optomec LENS 750 to acquire track geometry, as well as heat-affected zone (HAZ) and molten pool depth and width for both single and multiple track depositions. The deposition parameters used in the simulations correspond to those used for experimentation and measurement, and are provided in Table 2.4 for reference.

Table 2.4: Material properties of H13 tool steel and laser parameters for the deposition simulation.

Property	Units	Solid phase	Liquid phase
Density	kg/m^3	7835(Lin et al., 2007)	7835(Lin et al., 2007)
Specific heat	J/kg-K	658 (He et al., 2010)	804(He et al., 2010)
Thermal conductivity	W/m-K	28.6(Lin et al., 2007)	28.6(Lin et al., 2007)
Liquid viscosity	kg/m-s	-	0.005(He et al., 2010)
Thermal expansion coefficient	1/K	1.45e-5(He et al., 2010)	
Absorptivity	-	0.15	
Emissivity	-	0.70	
Latent heat	kJ/mol	2.72e5(He et al., 2010)	
Solidus temperature	K	1588(Lin et al., 2007)	
Liquidus temperature	K	1727(Lin et al., 2007)	
Surface tension coefficient	N/m-K	-4.3e-4(He et al., 2003)	
Laser power	W	350	
Laser waist diameter	mm	0.74	
Scanning speed	mm/s	14.82	
Track spacing	mm	0.30	
Powder flow rate	g/min	8.5	

Using the powder concentration and velocity from section 2.1.2, a source term for the levelset function was identified. Figure 2.24 shows the steady-state results for the track profile,

heat-affected zone, and molten pool with a comparison to the extracted boundaries previously shown in Figure 2.23. The track width and height were extracted from the cooled region in the model and were found to be 802 µm and 174 µm, respectively, compared to 786 µm and 169 µm from the experimental track, resulting in an error of 2% and 3% for the track width and height, respectively. Calculating the capture efficiency using equations (2.26) and (2.27) resulted in a 7.5% capture rate in experimentation compared to 7.7% from simulation, or a 2.6% difference.
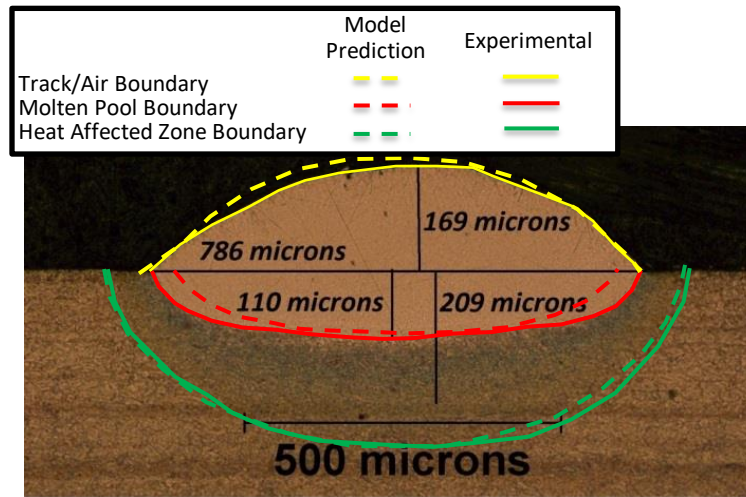
Figure 2.24: Comparison of H13 tool steel LDD simulation results to experimental measurements

The as-received substrate was composed of α-ferrite and pearlite, which upon heating, the pearlite colonies would transform into γ-austenite since carbon in the iron carbide will diffuse into the α-ferrite plates. Upon further heating, as the temperature passes the austenitic transformation temperature of H13 (T=1023 K), all of the ferrite will have transformed into austenite, which is governed by carbon diffusion. However, since rapid heating processes are observed during LDD, carbon diffusion can be neglected and material which has exceeded the austenitic phase transformation temperature will be fully converted from pearlite to austenite. Furthermore, since the cooling process is so rapid, all of the austenite of a single track will be transformed into martensite, though subsequent tracks may cause transformation of previous material into austenite during reheating (Bailey et al., 2017).

The heat-affected zone was compared against a curve created from the observation of the microstructure via optical microscopy, and was found to match both with respect to size and shape. Finally, for the molten pool region (T=1588 K), the shape was found to be sufficiently close,

though the width of the molten pool was found to be 40 µm less than the molten pool observed experimentally, or a 5% deviation. A laser beam diameter of 0.66 mm was modeled, but uncertainty exists depending on the actual lens distance from the substrate. Nonetheless, modeling results show a good correlation to all three validation points from the experimental data.

Using the experimental data of LDD of H13 tool steel powder onto an H13 substrate, the model was validated for a single track deposition to ensure the model accurately captured the molten pool and heat-affected zone shapes as well as the track geometry. Figure 2.25 provides an isometric view of the deposition of the 1st track showing the temperature isocontours upon completion of the single track simulation. Trends observed in the temperature field have also been observed by previous researchers (Wang and Felicelli, 2007, Wen and Shin, 2010, Wen and Shin, 2011, Momin et al., 2012). Based on the shape and location of each of the contours shown in Figure 2.24 and Figure 2.25, it can be seen that the deposition process was reasonably well captured in the simulation model for a single track simulation.
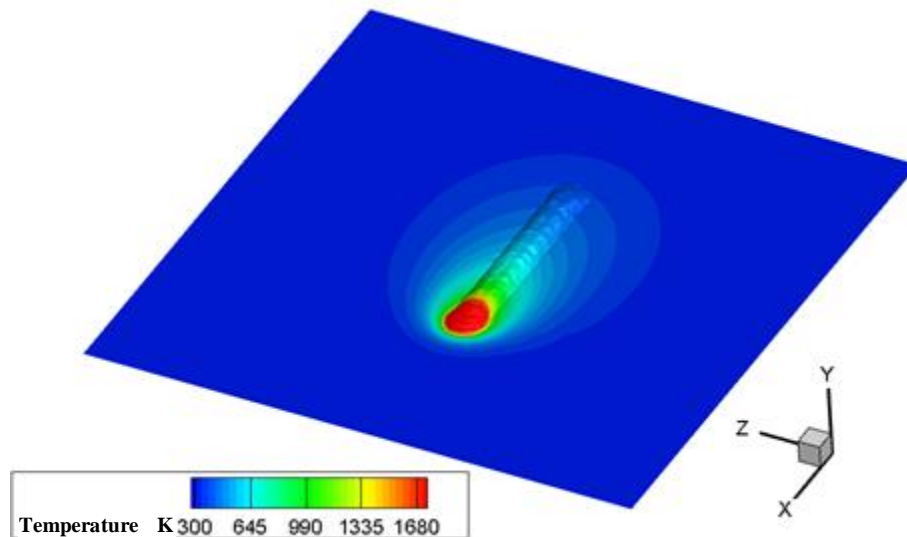
Figure 2.25: Isocontours at the conclusion of simulation for the 1st track deposited on H13 substrate.

Simulation of the LDD process involves a high computational cost. Since the goal of this simulation was to acquire the geometry and temperature profile of bulk deposition, the model must successfully calculate results for a multi-track scenario. From experimentation it was determined

that the cross-sectional profiles of the first two tracks in a multi-track deposition sample were unique, but the third and all subsequent track cross-sectional profiles were similar. Therefore, three subsequently deposited tracks provided an average steady-steady profile which essentially remained unchanged upon sufficient additional deposited tracks. Similar trends have been observed in the literature (Mazumder et al., 2012). Thus, to minimize the amount of simulation time, a solidified multi-track cross-sectional profile was captured based on a two-track experimental sample, as shown in Figure 2.26, and was used as the initial surface condition for the simulation of the third track deposition process.

The profile of the two track surface was created via a manual selection of the interface points at 10 μm intervals along the cross-section of the two-track sample, and was compared to additional multi-track experiments to ensure a reasonable and non-extreme track profile was being selected as the basis for further work.
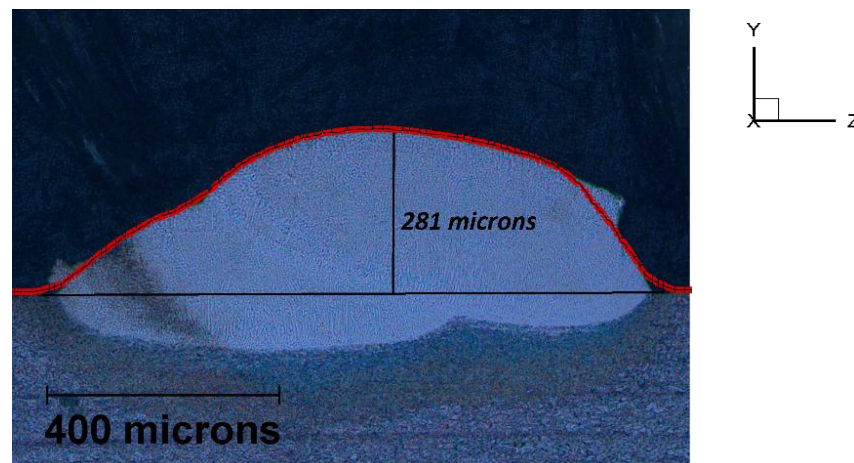
Figure 2.26: Extracted track geometry for the initial seeding of the three-track simulation.

Once the first two tracks were created, simulation of the third track commenced using the same laser parameters used during experimentation. The simulation was allowed to run until a pseudo-steady profile developed with respect to the direction of travel. This required approximately 4.5 mm of travel in the positive x-direction. Figure 2.27 shows an isometric view of the simulated three-track deposition process with temperature isocontours at the end of the simulation. Figure 2.28 compares the results of the simulated three-track deposition to an experimentally acquired three-track deposition. The heat-affected zone, molten pool and solidified

free surface are shown as dotted black, dashed black, and solid red lines, respectively. Although some discrepancy exists within the molten pool and heat-affected zone shapes with respect to the experimental results acquired for a three-track deposition, it was considered reasonable since variability was found between experiments using the same conditions, and an average representation was necessary for residual stress modeling efforts.
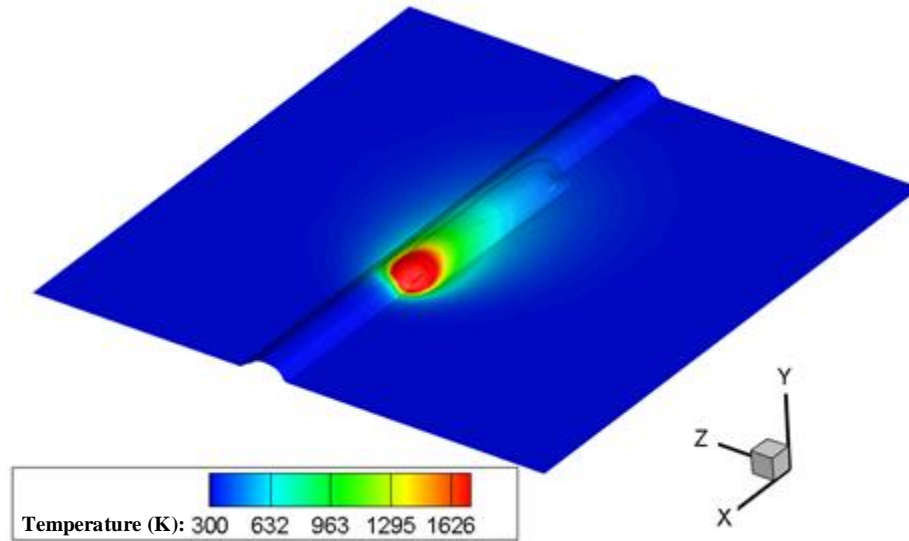
Figure 2.27: Results of the three-track simulation – surface after deposition.
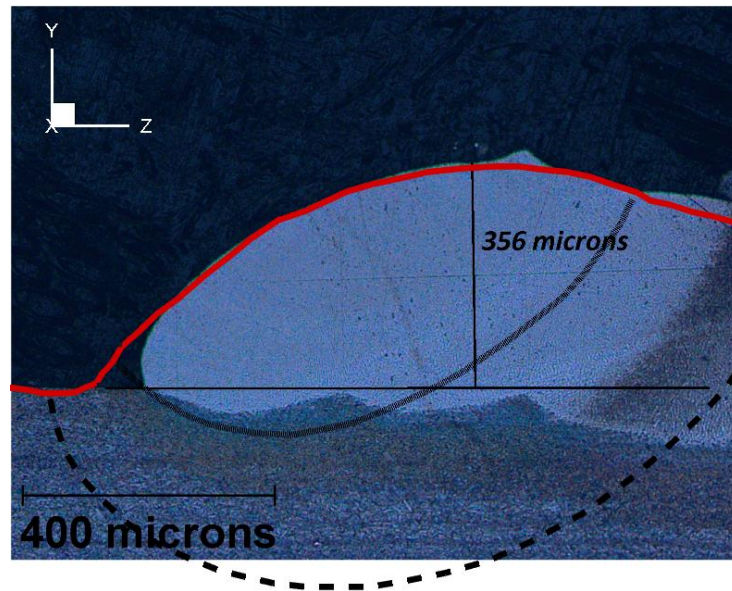
Figure 2.28: Molten pool (solid black), heat affected zone (dashed black), and deposited track geometry (solid red line) for the three-track deposition simulation compared with experiment.

66

Ultimately, the computational fluid dynamics model to describe the particle concentration from section 2.1.2 was developed for the four nozzle system found in an Optomec LENS 750 machine and has been shown to provide the predictive capability of the particle concentration and velocity. The error between the developed model and experimental data was quantified for two powder flows and showed a deviation of approximately 15% in particle concentration. Using the results from the CFD model, the powder concentration and velocities were used as boundary conditions in a direct laser deposition model to assess capture efficiency, which predicted the track height and width within 3% of experimentally observed values and predicted shape and size of the molten pool within 5% of experimental results. Both shape and size of the heat-affected zone matched observations, although there is some degree of uncertainty in clearly identifying the boundary. From the single track geometry prediction, capture efficiency was calculated and found to deviate 2.6% from experimental capture efficiency. With experimental data available, simulation time was reduced significantly staging the simulation result with the deposited material, and was successfully used in (Bailey et al., 2017) to extract the temperature field and track geometry necessary to perform residual stress calculation in a multi-layered component.

2.2.2 Ti-6Al-4V Multi-track Deposition

A computational domain was composed of a 12mm x 8mm x 12 mm volume with two sub-domains: one comprised of the original substrate, and the other being a gas. Figure 2.29 provides a diagram of the domain and the discretization used for the simulation. A 12mm x 5mm x 12mm substrate is arranged such that the substrate is located in the negative y-plane of the domain, while the volume located above the substrate consists of gas. Discretization of the domain was performed such that 343,728 computational volumes were created as shown in Figure 2.29. A region 6.0mm x 1.0mm x 2.5mm was created using uniform grid spacing to allow for simplicity of the numerical schemes within the region where the most complex physics occur. Beyond this region of interest, a non-uniform grid was used to minimize the number of elements within the domain to allow for a reduction of computation time when compared to using a uniform mesh throughout. Within the refined computational region, levelset reinitialization is performed to ensure the gradients of the levelset field remain close to unity, which is necessary to ensure source terms are applied correctly (Sussman et al., 1994).
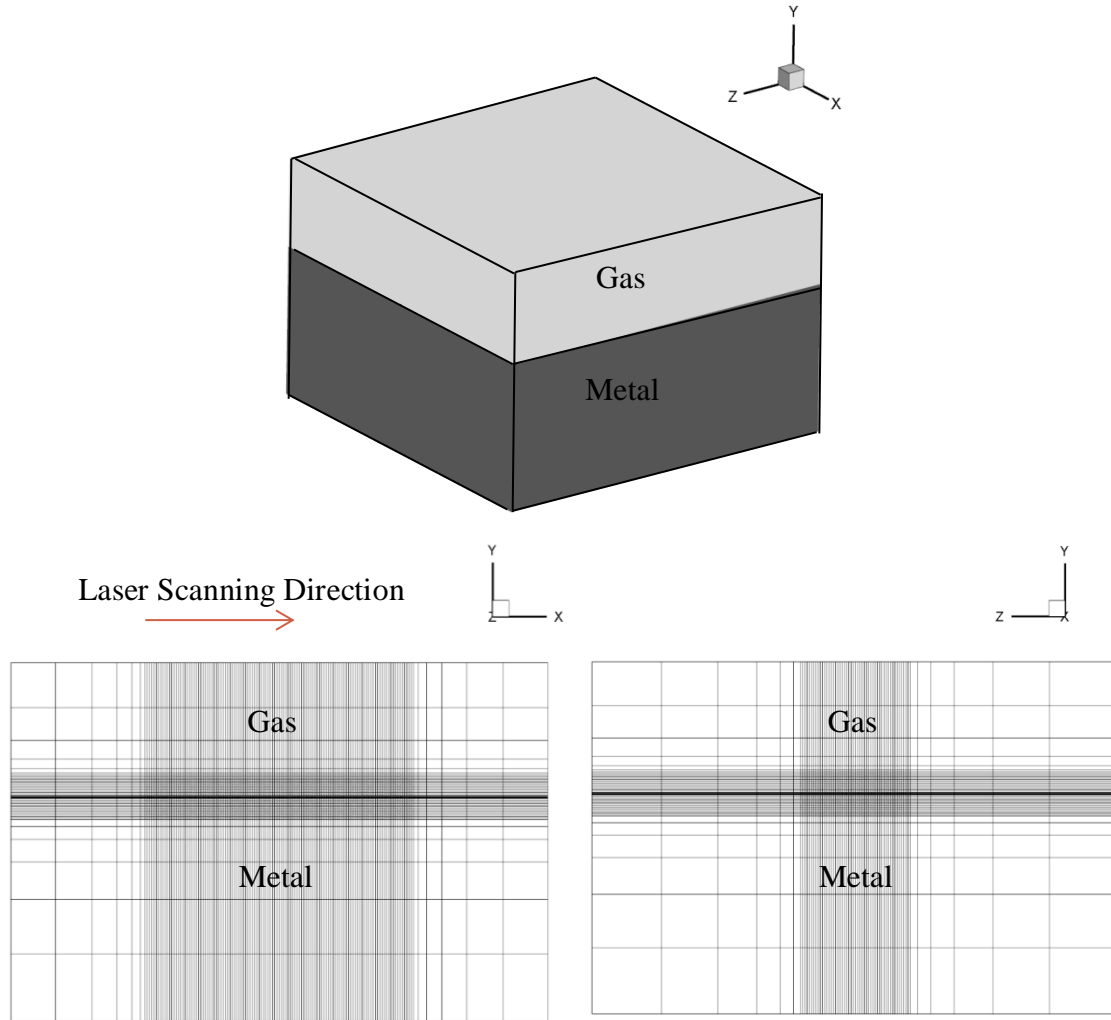
Figure 2.29: Discretized domain used for Ti-6Al-4V LDD simulation

The governing equations were solved numerically using an in-house finite volume solver developed in FORTRAN. A dual time stepping algorithm, a method which has been shown to solve both compressible or incompressible flows (Li and Merkle, 2006), was employed since source terms within the governing equations are dependent on the conserved quantities. Temporal discretization was performed implicitly with second-order accuracy using time steps of 1.0e-5s with 25 pseudo-time steps for each physical time step to ensure the stability of the current time step prior to continuing. Residuals for conserved quantities were monitored throughout the simulation and were observed to be less than 10e-6 for continuity and momentum, while the energy residual was less than 10e-9 before time advancement occurred. The simulation was allowed to continue for 0.25 seconds of LDD process time to guarantee that pseudo-steady conditions would

be observed, and corresponded to 3.74mm of laser beam travel. The model required 102 hours of run time on 20 cores of an Intel Xeon E5-2660 v3 operating at 2.6 GHz to simulate the LDD process traveling 3.74 mm in the scanning direction. To ensure the levelset gradient at each computational cell within the domain was near unity, levelset reinitialization was performed during each pseudo-time step using the method described by Min (Min, 2010). Sethian and Smereka (Sethian and Smereka, 2003) have explained that the levelset method does not yield a mass conservative approach due to inaccuracies of being able to obtain a sharp interface over time and also a movement of the interface during reinitialization of the levelset field; however, using a dual time-stepping algorithm while performing reinitialization at every pseudo-time step allows for mass correction during the solution procedure. Large density differences between phases are known to cause numerical instability when using diffuse interface methods such as the levelset method if large driving forces are included (Ghods and Herrmann, 2013), and thus a gas with a density similar to that of the substrate material was used to prevent excessive numerical interphase mass and momentum transfer.

Thermal and physical property data was collected and corroborated among various sources from suppliers and literature, as shown in Table 2.5. Thermal conductivity is known to vary significantly as a function of temperature, and must be updated correctly during the numerical solution to ensure proper thermal transport during simulation. Data from (Boivineau et al., 2006) and (Mills, 2002) were corroborated throughout the solid phase range and were fitted using a linear curve fit, which is shown in equation (2.28). The R^2 value of the curve fit was 0.993.

$$k\{W/m - K\} = 0.01327 * T\{K\} + 2.770 \tag{2.28}$$

For temperatures above 1650°C, an expression for the thermal conductivity as a function of temperature was found in (Boivineau et al., 2006). Liquidus and solidus temperatures were corroborated between (Mills, 2002, Boivineau et al., 2006). Absorptivity and emissivity of Ti-6Al-4V were found from prior experimental results collected by Yang et al. (Yang et al., 2010) which were found to be 0.34 and 0.25, respectively, for irradiation in the infrared region of 1064nm. To replicate the setup during the LDD process, the laser beam was profiled and a fifth-order surface was used to approximate the laser intensity profile for use during the simulation. The equation of the intensity is shown as equation (2.29)

$$I(\tilde{r})\left[\frac{W}{m^2}\right] = P_{laser}\alpha(2.1004e-6\tilde{r}^5 - 1.9880e-3\tilde{r}^4 + 5.7769e-1\tilde{r}^3$$
$$- 7.3899e1\tilde{r}^2 + 2.6673e3\tilde{r} + 3.971e6) \tag{2.29}$$

where $\tilde{r}$ is the distance of a given location away from the center of the laser beam scaled to microns to minimize numerical roundoff error, P_{laser} is the laser wattage, and α is the absorptivity of Ti-6Al-4V. Beyond a distance $\tilde{r}$=463 μm from the laser beam center, the intensity is set to zero since the laser profile showed a negligible laser intensity at such a distance from the beam center. During the simulation, the scanning speed was set to 15.0 mm/s, the laser power was 350W, and the powder feed rate was 1.5 g/min to replicate experimental conditions.

Table 2.5: Thermal and physical properties of Ti-6Al-4V

Property	Units	Solid phase	Liquid phase
Density	kg/m³	4506	4506
Specific heat	J/kg-K	560	560
Thermal conductivity	W/m-K	0.01327T+2.770	0.0183T-6.66[Boivineau et al., 2006]
Liquid viscosity	kg/m-s	-	3.2e-3[Westerberg et al., 1998]
Thermal expansion coefficient	1/K	8.9e-6	
Absorptivity	-	0.34[Yang et al., 2010]	
Emissivity	-	0.25[Yang et al., 2010]	
Latent heat	J/kg	3.65e5	
Solidus temperature	K	1878[Mills, 2002, Boivineau et al., 2006]	
Liquidus temperature	K	1933[Mills, 2002, Boivineau et al., 2006]	
Surface tension	N/m	1.65[Westerberg et al., 1998]	
Surface tension coefficient	N/m-K	-2.4e-4[Westerberg et al., 1998]	

Boundary conditions for the simulation include insulated non-slip walls around the entire periphery of the domain. Since the laser heating and fluid flow phenomena are significantly far away from the boundaries of the domain, this assumption is reasonable. Finally, convection was

modeled using a constant convective heat transfer coefficient at the free surface with a value of 100 W/m-K.

Validation images for the Ti-6Al-4V LDD process were collected from experimentation which is described in (Katinas et al., 2019). As the determination of the optimal LDD parameters of Ti-6Al-4V powder (resulting in a deposition with no porosity and full melting of captured powder) is not the focus of this work, the experimentally-determined parameters after preliminary experimental studies are given in Table 2.6.

Table 2.6: Summarized laser deposition parameters for Ti-6Al-4V single tracks

Laser power (W)	350
Laser scan speed (mm/s)	15
Powder feed rate (g/min)	1.5
Stand-off distance (mm)	9.5
Laser spot size (μm)	926

A prepared cross-section was analyzed via optical microscopy to acquire the correct location of the heat-affected zone profile for validation of the simulation result, as shown in Figure 2.30. The microstructure of the as-deposited single track is clearly shown within the Ti-6Al-4V bead and the hot-rolled Ti-6Al-4V substrate. The boundaries between the fusion zone (FZ), the heat-affected zone (HAZ) and the Ti-6Al-4V substrate can be identified by the microstructure differences as shown in Figure 2.30. During the LDD process, rapid heating and cooling take place in a concentrated area as the result of highly localized laser irradiation. In fact, cooling rates as high as ~10^4 K/s (Murr et al., 2009) have been observed in previous literature. In the heating cycle, the laser irradiation will increase the surface temperature of the deposition area in excess of the liquidus temperature and produce a molten pool which will be quenched by the addition and melting metallic powder. As the laser beam moves away, the molten pool solidifies rapidly. As the temperature further decreases below the solidus point, the molten pool completely solidifies and a weld bead is formed, as can be seen in Figure 2.30. The difference between the liquidus and solidus temperatures is small, thus they are difficult to distinguish from the microstructure view.
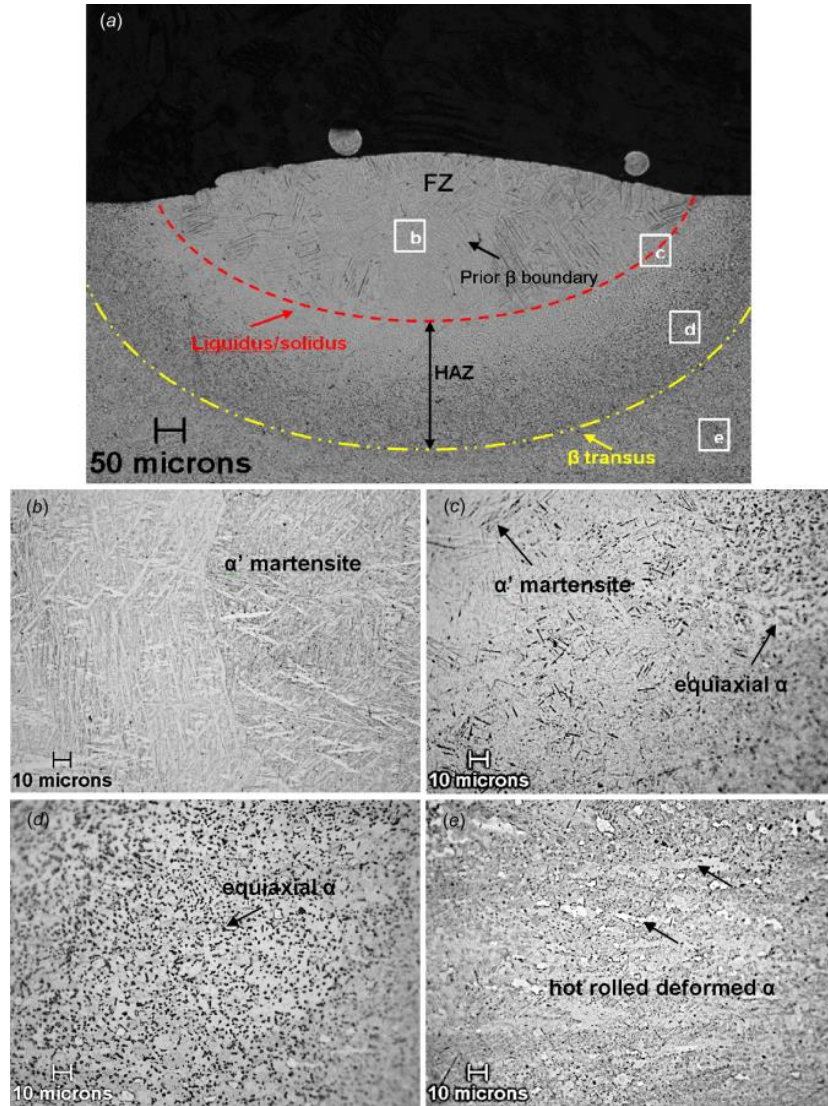
Figure 2.30: Microstructures of the laser direct deposited Ti-6Al-4V bead and the hot-rolled Ti-6Al-4V substrate (Katinas et al., 2019)

With the experimentally-determined location of the heat-affected zone, molten pool, and free surface, a cross-section of the numerical simulation results for the direct laser deposition process was compared to experimental data. Figure 2.31 provides a comparison of the model results as compared to the experimental results of a single track at the pseudo-steady condition (i.e. track, molten pool, and heat affect zone geometry do not change along the travel direction). The free surface boundary has both a similar shape and size when comparing the experimental and simulation results. Experimental and simulated track widths are 941 μm and 910 μm, respectively, while corresponding track heights are 87 μm and 85 μm, respectively. By using equation (2.26)

to calculate the amount of mass captured by the molten pool, the capture efficiency was found to be 12.0% experimentally, while the simulated capture efficiency was 11.7%, or a 2.5% error in capture efficiency prediction. Next, the simulated molten pool width and depth closely resemble those found experimentally with a depth of 211 μm and a width of 858 μm (compared to 195 μm and 894 μm for experimental depth and width, respectively). The maximum dimensional error in the profile of the molten pool shape was 36 μm at the edge of the deposited material. Finally, the heat-affected zone was simulated to have a width and depth of 1310 μm and 543 μm, respectively, while the experimental width and depth were found to be 1331 μm and 470 μm, respectively, corresponding to an error of 1.5% in the width and 15.5% in the depth of the heat-affected zone region. Root mean squared error was calculated for the free surface, and molten pool and heat-affected zone boundaries based on the closest distance to the experimental profiles every 50 μm along the horizontal direction, and were found to be 1.1 μm, 17 μm and 73 μm, respectively. One possible reason for the discrepancy in the heat-affected zone profile while the free surface and molten pool boundaries show the good agreement is that the temperature-dependent thermal and physical properties of the solid phase could differ from those shown in Table 2.5 which could result in enhanced or inhibited thermal diffusion. Additionally, the convective heat transfer coefficient might need to be estimated more accurately based on the shielding gas flow rate.
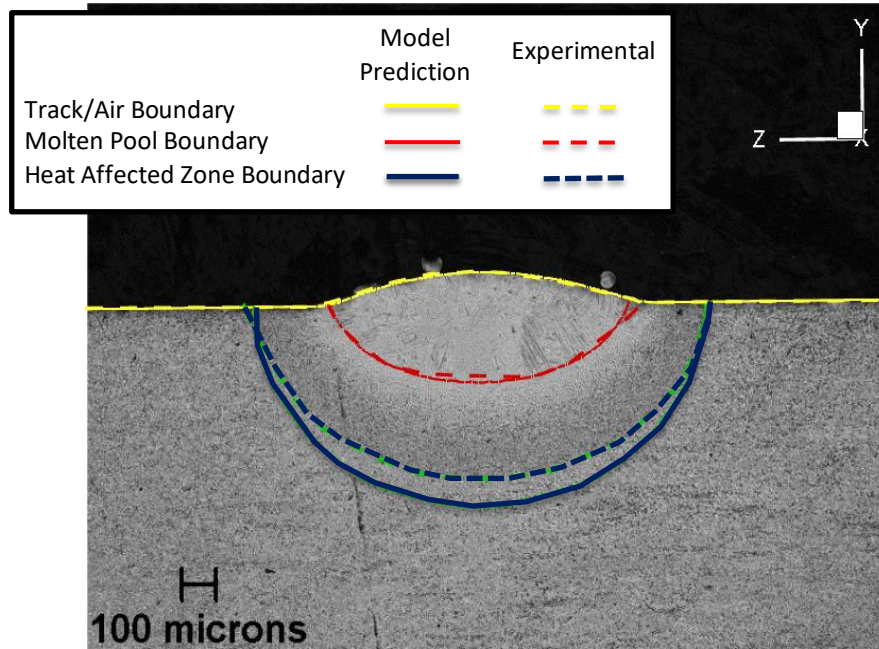
Figure 2.31: Cross-sectional view of Ti-6Al-4V single track deposition

A summary of the comparison between model and simulated results are shown in Table 2.7. Errors calculated in Table 2.7 are shown as positive if the model overpredicts a given experimentally-determined quantity.

Table 2.7: Comparison of experimental and modeled deposition

		Experimental	**Simulation**	**Error**	**Error (%)**
Track	Width (μm)	941	910	-31	-3.3
	Height (μm)	87	85	-2	-2.3
Molten Pool	Width (μm)	894	858	-36	-4.0
	Depth (μm)	195	211	16	8.2
HAZ	Width (μm)	1331	1310	-21	-1.6
	Depth (μm)	470	543	73	15.5
Capture efficiency	(%)	12.0	11.7	0.3	-2.5

The temperature profile and track geometry throughout the deposition process were analyzed by investigating the symmetry plane of the simulation domain, as shown in Figure 2.32. The free surface of the deposition is signified by the interface between the white background and colored contours; hence, deposited Ti-6Al-4V is represented by any material which resides below the free surface and above the original surface of the substrate, while gas is found above the free surface. Any material within the domain which exceeds the liquidus temperature of Ti-6Al-4V is shown in red, and is either within the heating region of the laser beam or behind the laser irradiation source. From the center plane, it can be seen that the heat-affected zone, which is defined by the region between the liquidus and beta transus temperatures extends approximately 543 μm below the original surface of the substrate. During the simulation, the effect of evaporation was neglected due to the relatively low laser fluence during LDD. This assumption is valid because the boiling point of Ti-6Al-4V in literature was found to be 3315K (Rai et al., 2007), while the maximum temperature observed within the simulation is 2781 K, or 534 K less than the boiling point. Using the average free surface temperature of the molten pool region (2212 K), evaporation would account for less than 0.2 μm of the track height and is insignificant with respect to the track geometry (Ivanchenko et al., 2003).
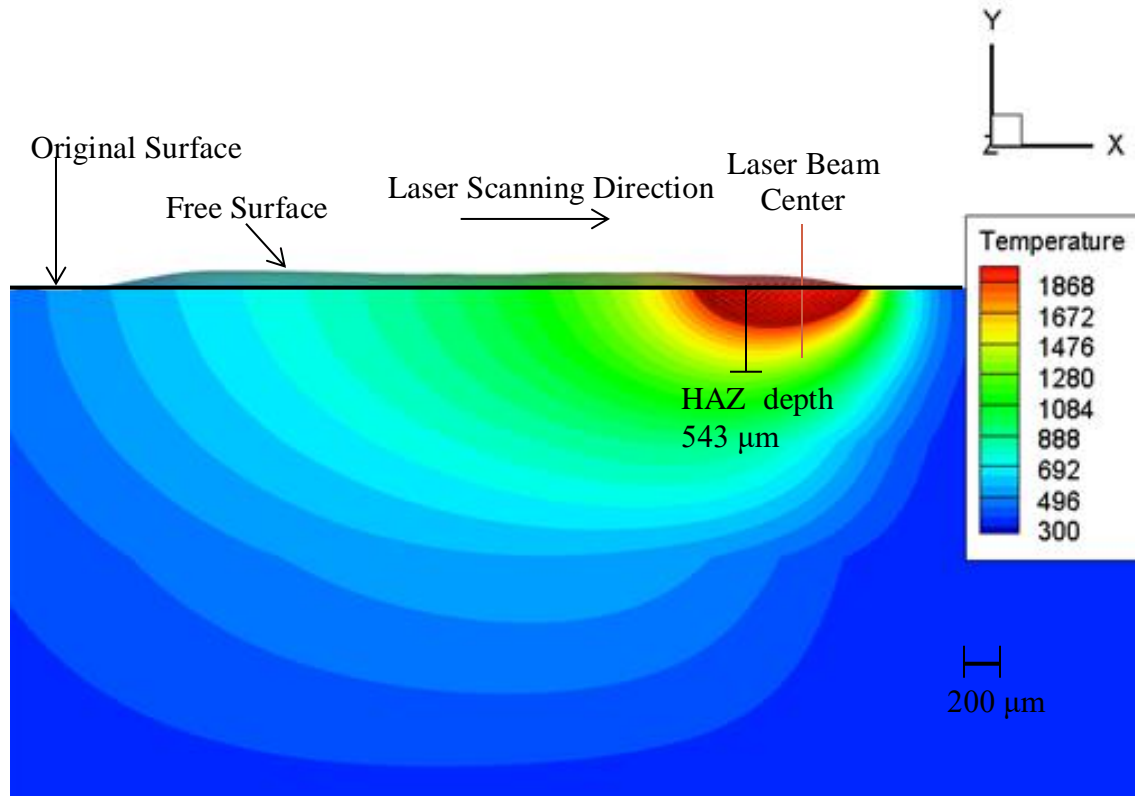
Figure 2.32: Temperature field at center plane during the LDD process at 0.25 s (Temperatures in Kelvin)

As a final basis for verifying the simulation results, the velocity field of the molten pool at various slices is shown in Figure 2.33. The driving force behind the flow within the molten pool is primarily due to Marangoni shear stress (Pirch et al., 1996), which is a surface force developed by large surface temperature gradients as well as the temperature derivative of the surface tension. Therefore, velocities observed at the surface of the molten pool point away from the beam center at the surface and backfill beneath the surface of the molten pool, which drives a toroidal flow pattern as shown in Figure 2.33(a), (b), (c). Several authors have shown the effect of laser irradiation on molten pool flow, such as counter-rotating vortices in the molten pool during laser heating (Pirch et al., 1996, He and Mazumder, 2007, Manvatkar et al., 2015a). The counter-rotating vortices are clearly depicted in Figure 2.33(a) and (c) and have a maximum velocity magnitude of 0.148 m/s, which is representative of the flow conditions simulated. The maximum velocity observed within the domain is located at the free surface and has a magnitude of 0.192 m/s. If the LDD process is simulated in FEA, fluid flow effects may not be considered and can

subsequently change the shape and size of the molten pool. Therefore, it is necessary to consider the molten pool dynamics to accurately determine the free surface shape, and ultimately, the capture efficiency. Since this model provides a physical representation of the LDD process, its usefulness extends beyond the simulation of single-track configurations on a large substrate, and can be used to simulate multiple-track or multiple-layer configurations, deposition on the edge of a substrate, or tracks following a non-linear contour.
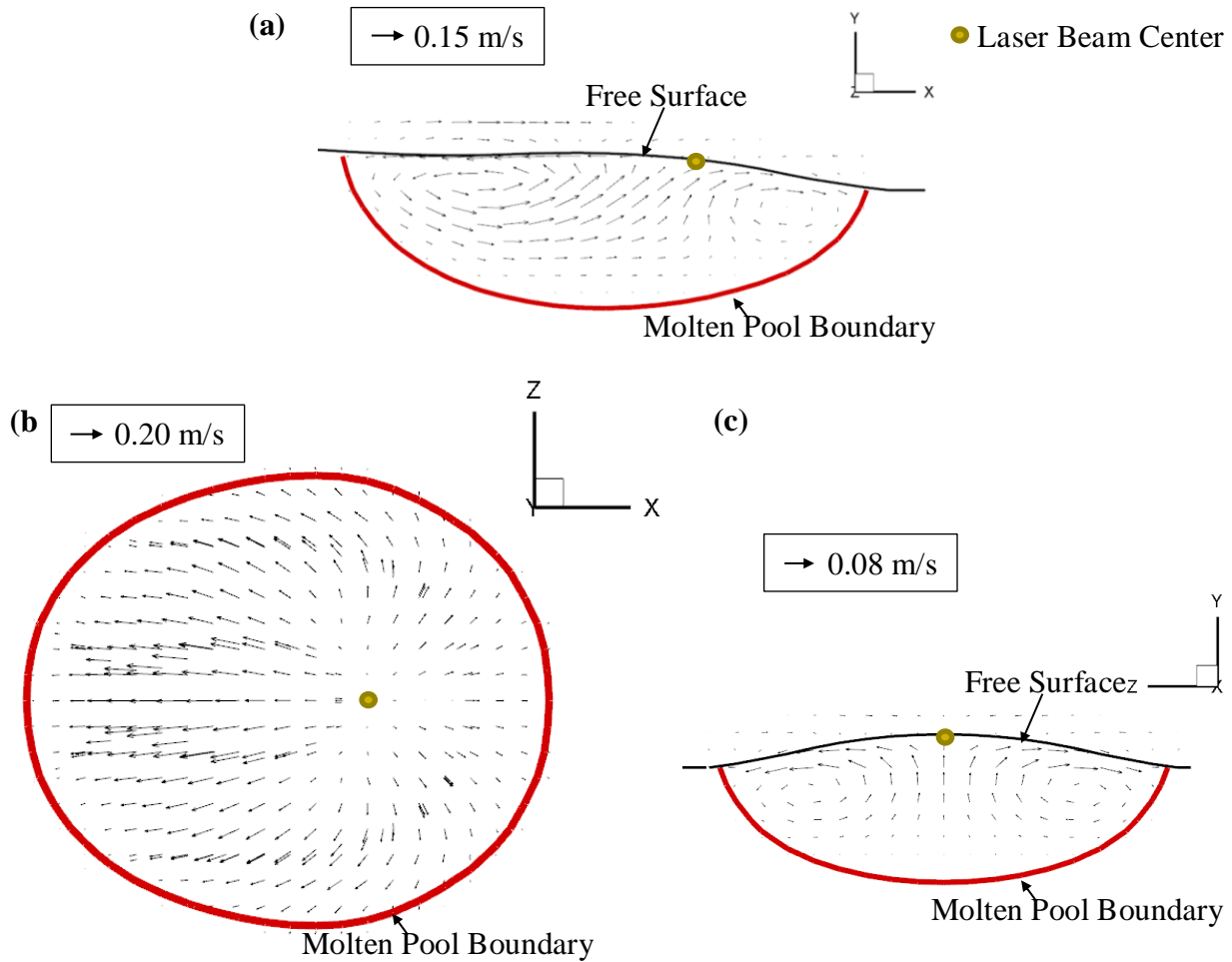
Figure 2.33: Molten pool velocities (a) side view (b) top view (c) front view at laser beam center

The modeling effort was then extended to predict the multi-track deposition of Ti-6Al-4V. To simulate additionally deposited tracks, the results from the previous track were utilized as the

starting point for the next track. The deposition process was simulated in a manner similar to what was observed during experimentation. However, to avoid the excessive computational cost to simulate the delay time between adjacent tracks, the temperature field was reset to a uniform starting temperature (300 K) and the laser was positioned to begin deposition with the topography from the previous track. Figure 2.34 illustrates the predicted free surface and temperature distributions for sequential tracks, up to a three-track deposition. The free surface was acquired by plotting the zero levelset isocontour, which indicates the interface between the gas and metal phases. In Figure 2.34(d), the 3D view of temperature distributions along the scan direction (XY plane) and on the central cross-section (YZ plane) is shown. In order to depict the molten pool, temperatures in excess of the liquidus temperature (1933 K) were plotted red. In Figure 2.34, it is shown that deposition of subsequent tracks results in part of the overlapping region to re-melt and solidify again. If the distance between adjacent tracks is selected appropriately, the resulting deposition will have minimal surface roughness.
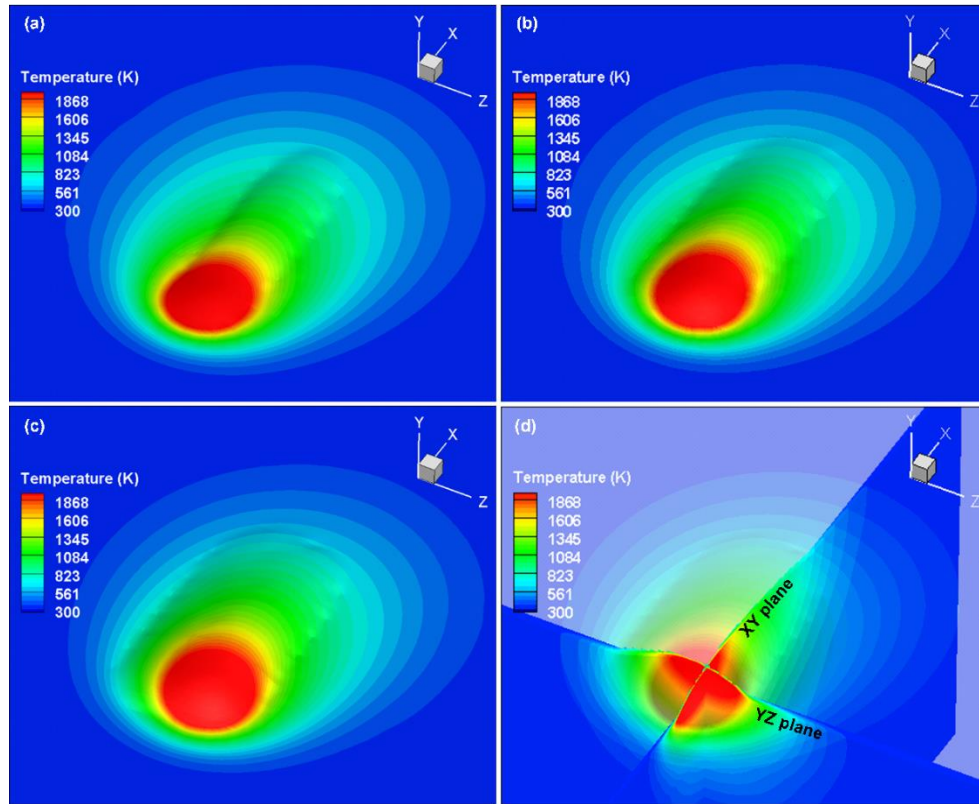
Figure 2.34: Isometric views of predicted free surface indicated by the levelset value of zero and temperature distributions for the laser direct deposited (a) single-track, (b) two-track, (c) three-track Ti6Al4V deposits. (d) A 3D view of temperature distributions on different planes.

Validation of the deposition model was performed via comparison of the predicted free surface and temperature field on the central cross-sectional images of experimentally obtained depositions (YZ plane in Figure 2.34(d)). Figure 2.35 depicts the predicted free surface and extracted isotherms for the fusion zone (liquidus temperature, 1933 K) and the heat-affected zone boundaries (β transus, 1269 K) which have been superimposed on the experimental microstructure for each of the experiments: one, two, and three track depositions, with solid lines representing simulation results while the dashed lines indicate experimental observations. As shown in Figure 2.35, the free surface, fusion zone and heat-affected zone boundaries are predicted by the LDD model, though the error associated with the prediction increases with the increase of track numbers. Throughout the prediction of the deposition process, the depth of the heat-affected zone is accurately captured by the model, although the width deviates from the experimental data by up to 120 μm for the three-track case. The geometry of the free surface for single and two-tracks agrees well with experimental results, with a profile error of nearly 50 μm for the third track. It should be noted that the cross-sectional profile of the track and thermally-dependent features may not be consistent throughout a long track due to the factors such as the adhesion of partially melted particles to the track surface, potential contamination on the substrate surface and/or the sudden instability of the argon flow; therefore, an estimated error within 5% is expected for the experimental profile. From previous literature, the track geometry of a third parallel track on a substrate is known to be representative of that from any additional tracks (Mazumder et al., 2012). The temperature field and free surface profiles will not change significantly for subsequent tracks and can therefore be extracted as inputs to predict the material phases of any multi-track deposition process.

By modeling the multi-track AM process, thermal features such as heating and cooling rates can be extracted anywhere within the computational domain. Figure 2.36(a) depicts the extracted pseudo-steady temperature fields at various depths within the molten pool shown via the yellow line in Figure 2.36(b). The selected locations are positioned in the Y-Z plane with a distance of 0.07 mm between adjacent points. The temperature field and heating/cooling rate field on the central X-Y plane (Z=0) are depicted in Figure 2.36(c) and Figure 2.36(d), where the contours of the liquidus and β-transus temperatures are plotted, indicating the molten pool and heat-affected zone boundaries, respectively. The model predicted a maximum temperature of about 2650 K near

78

the free surface of the molten pool. By using equation (2.9), the local heating rate was found to be in excess of 2×10^4 K/s and was located at the leading edge of the molten pool. Similarly, the average cooling rates in the fusion zone and heat-affected zone were calculated to be approximately 10^4 K/s and 5×10^3 K/s, respectively. Since thermal energy will conduct away from the surface being irradiated, the peak temperature, as well as heating and cooling rates, decreases downwards along the straight line in Figure 2.36(b).
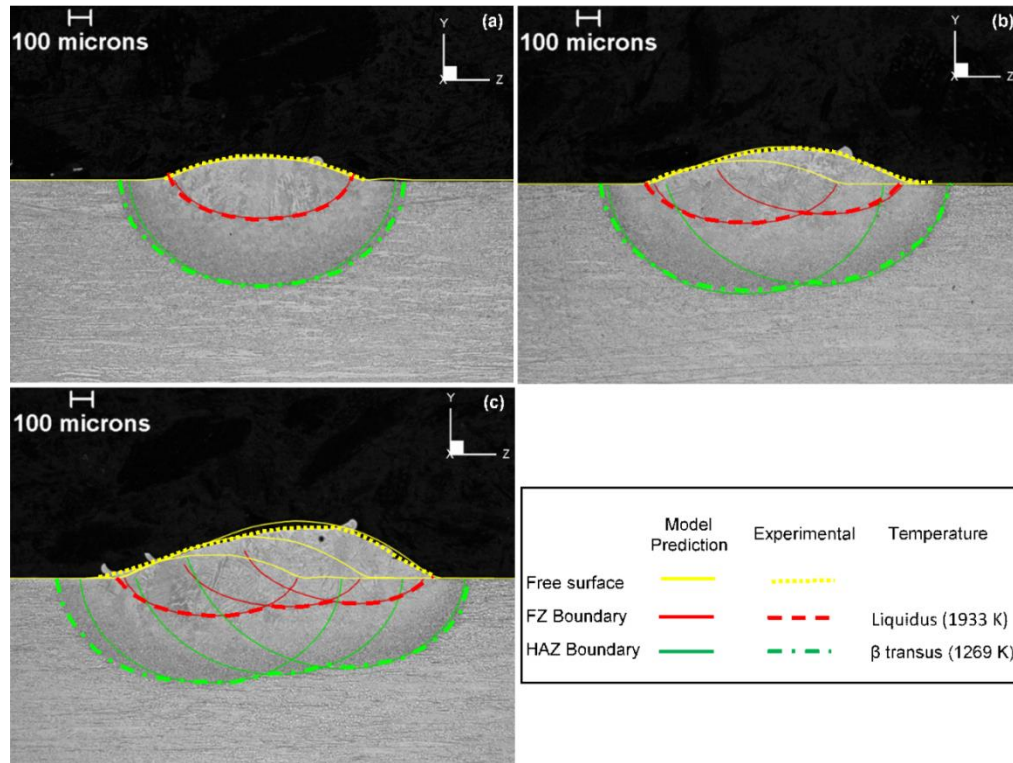
Figure 2.35: Cross-section views of predicted free surface, fusion zone (FZ) and heat-affected zone (HAZ) boundaries compared with experimental observations for (a) single-track, (b) two-track, (c) three-track Ti6Al4V deposits built by laser direct deposition.
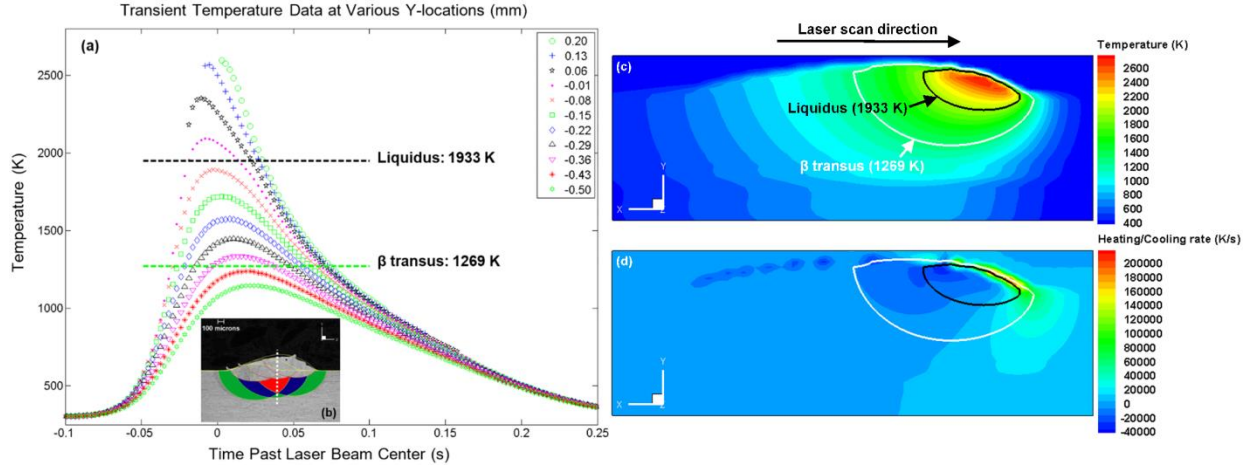
Figure 2.36: (a) The extracted temperature profiles at different locations along (b) Y direction from fusion zone to the substrate of the three-track Ti6Al4V deposition. The green, blue and red zones in (b) indicate single-track, two-track overlapped and three-track overlapped heat-affected zones while the other section is fusion zone. (c) The temperature field and (d) cooling rate field on the central XY plane (Z=0).

A model describing the direct laser deposition of Ti-6Al-4V powder to a Ti-6Al-4V substrate has been developed, and effectively predicts the capture efficiency within 2.5% of the physical value by using experimentally-verified information for powder flow and laser irradiation profile to eliminate the need for capture efficiency assumptions for a complex powder feed nozzle. During the simulation of the LDD process, it was shown that the laser irradiation increased the temperature sufficiently high such that complete melting of any Ti-6Al-4V powder entering the molten pool was observed; however, the temperature never exceeded the boiling point of the deposited material. The location of the heat-affected zone from the experimentation was verified with microstructure examination. Microstructure testing of the as-deposited material was shown to provide insight into the phase transition which enabled contours of the β-transus and liquidus temperature to be extracted and compared with simulation results. The predictive error associated with the track height and width of the deposited material is 2 μm and 31 μm, respectively, for a maximum error of 3.3% of the experimentally determined deposition. For the molten pool, a maximum of 11.1% error was observed in the molten pool profile compared to the experimental profile. The highest temperature field error was observed in the heat-affected zone, which corresponded to a maximum dimensional error of 73 μm, or 15.5%.

2.2.3 Stellite-6 on Mild Steel Cladding

To further demonstrate the capability of the modeling methodology, a cladding operation of Stellite-6 on mild steel substrate was modeled and validated against experimental data of a different AM machine. As opposed to the previous blown powder cases, the system used for this cladding is a custom-built system, further referred to as the Gantry system. The Gantry system is an open-air deposition machine with a coaxial argon-assisted powder feeder nozzle and a fiber laser irradiation source. A commercially-available Precitec YC50 coaxial powder feed nozzle is installed selected due to availability and installation on a variety of cladding systems (Köhler et al., 2013, Ng et al., 2009). The Gantry system is equipped with a 1000 W IPG fiber laser operating at 1075 nm wavelength and configured such that the laser center axis was coincident with the powder nozzle axis. At the laser focal plane, the beam diameter was found to be 248 μm with a Gaussian intensity distribution. Figure 2.37 shows the experimental setup and details of the laser and nozzle geometry.
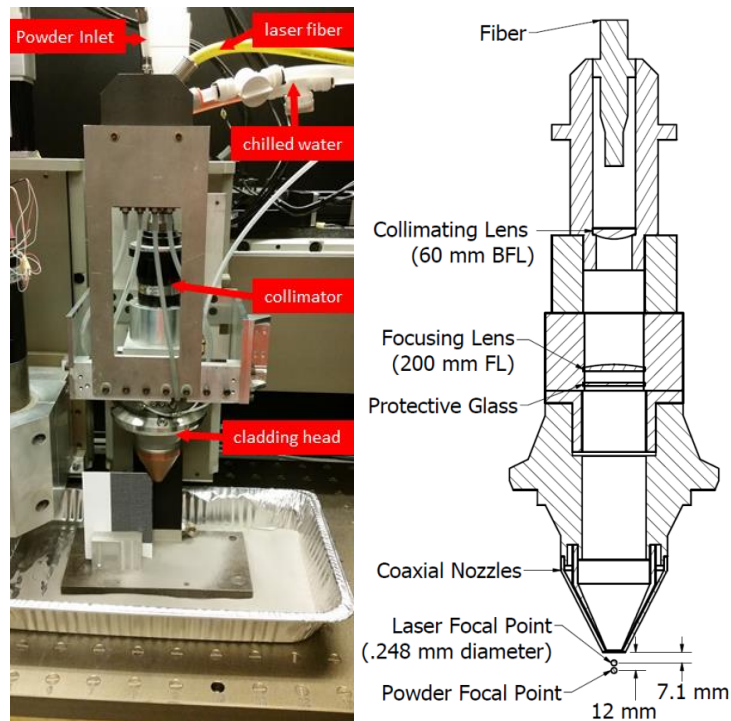
Figure 2.37: Experiment setup of the Gantry system (left) and a cross-sectional view of laser/nozzle geometry (right)

Back-reflection of the laser irradiation source was a concern, and it was determined that either the nozzle or substrate needed to be tilted so as to prevent the surface normal to be collinear with the laser beam axis. Previous researchers have found that the nozzle orientation will affect the powder flow, and thus, the available powder and laser irradiation at the surface for cladding (Lin and Hwang, 1999), but that inclining the substrate will also change the characteristics of the clad (Pinkerton and Li, 2004a). A brief powder flow study was performed at different nozzle incline angles and showed that the powder velocity was not sufficiently high to prevent a change of the powder distribution at even a minimal angle, as shown in Figure 2.38. Since the powder flow was impacted so significantly with nozzle tilt angle, the nozzle remained vertical and the substrate was inclined by 10°.
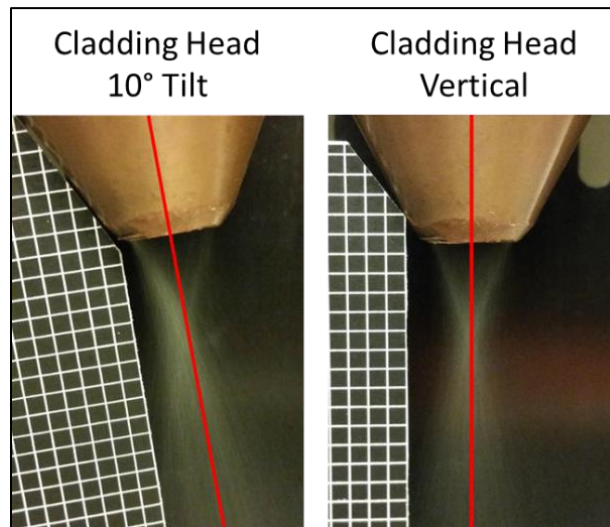
Figure 2.38: Powder flow for 10° cladding head tilt (left) and cladding head vertical (right) at 30 g/min powder flow 20 SCFH carrier gas

Modifiable cladding system parameters were discussed in previous literature by Weerasinghe and Steen (Weerasinghe and Steen, 1987). These parameters, as well as an additional degree of freedom since the focal lens is adjustable with respect to the powder nozzle, are shown in Table 2.8. Parameters which are have not been modified in this study are laser beam shape, and the particle injection velocity, shape and size, as changing the beam shape would require a laser source change, and the Stellite-6 powder was provided from a single supplier with the powder size of 50-150 μm.

The predictive modeling of the cladding process was developed such that it could be used for a variety of cladding materials and system process parameters. Simulation of the process is completed by minimizing assumptions associated with the laser beam irradiation source, powder concentration profile, and powder velocity profile by modeling the powder distribution process with computational fluid dynamics. Simulation of the cladding process was performed by analyzing each interaction of the process individually, and then combining the results to provide the necessary boundary conditions for a model with a sequential approach as follows:

1) Simulate the powder flow for a known powder feed rate for laser-powder interaction
2) Determine the laser power attenuated by the particle cloud
3) Simulate the cladding process using the powder concentration and laser power profiles from (1) and (2) to quantify powder-substrate and laser-substrate interactions

Table 2.8: Gantry System Adjustable Parameters

System Variable	Units	System Range	Parameter Range Used
Laser Power	W	0-1000	200-800
Beam Diameter	μm	248-1940	500-1940
Beam Shape	-	Top-Hat	**Fixed**
Powder Mass Flow Rate	g/min	0-40	0-40
Particle Injection Velocity	m/s	0-10	**Fixed**
Particle Shape	-	Flake to Spherical	**Fixed Shape**
Particle Size	μm	45-150	**Rosin-Rammler (Mean diameter 96 μm, 50/150 min/max dia.)**
Laser Scanning Speed	mm/s	0-100	0-40
Hatch Distance	μm	0- 30000	0-1500
Nozzle Stand-off Distance	mm	5-50	8-14

Successful modeling of the cladding process can be validated against experimental data to match three profiles: the free surface, the molten pool (if it exists), and the heat-affected zone (HAZ). All three profiles simultaneously matching against a cross-sectional slice of the clad

indicates material properties, laser energy distribution, and powder absorption are modeled in a manner consistent with the physical deposition process.

Powder flow modeling was performed using computational fluid dynamics (CFD) simulation of the gas and particle flow and its interaction in the free stream via conservation of mass and momentum coupled with a standard k-ε turbulence model (Launder and Spalding, 1983, Katinas et al., 2018). A method similar to that demonstrated in section 2.1.2 was used for this study; with the exception of modified geometry since the aforementioned study used a four-nozzle powder feed system, whereas this nozzle is coaxial. Similar to directed energy deposition (DED) or laser direct deposition (LDD), powder concentration for blown powder processes such as cladding is typically low enough such that a discrete phase model doesn't necessitate the need for modeling of powder particle collisions. Physical properties of the gas and powder phases used for modeling are provided in Table 2.9 and Table 2.10. The simulation was performed assuming an incompressible gas since velocities observed during the particle ejection process are less than 5% of the speed of sound. Additionally, particle size distribution was incorporated into the model based on a Rosin-Rammler distribution for the Stellite-6 particles utilized in experimentation (ANSYS, 2009).

Table 2.9: Physical Properties of Gas Used in Simulation

Property	Units	Value
Density	kg/m^3	1.225
Viscosity	kg/m-s	1.81e-5
Specific Heat	J/kg-K	1000
Temperature	K	300

Table 2.10: Physical Properties of Stellite-6 Powder

Property	Units	Value
Density	kg/m^3	8480
Mean Particle Diameter	μm	96
Particle Size Range	μm	45-150
Shape Factor	-	0.80
Distribution Spread Factor	-	4.23

Conditions for the powder simulation were selected based on the experimental conditions for a cladding scenario which was expected to yield minimal dilution; hence, a powder flow rate of 25 g/min was selected. Since particle-particle interactions were neglected from the model, particle concentrations can be scaled linearly with the powder flow rate provided that a sparse particle cloud remains. From (Katinas et al., 2018), it was shown that substrate need not be modeled to account for the powder concentration when particles are not influenced by the gas stream, as particles that do not directly impact the molten pool will not be absorbed, but rather reflect off of the substrate surface. Thus, free stream modeling can be used to simulate the particle trajectories within the domain of interest, and the powder concentration for a given standoff distance can be used by extracting cross-plane results from the CFD model and curve fitting to obtain a continuous function.

With the particle concentration known, scattering through the particle cloud was performed in a manner similar to that of Jouvard et al. (Jouvard et al., 1997), with the exception that the powder concentration obtained from the CFD model is to obtain local laser attenuation values which can be integrated throughout the region of interest to obtain the overall laser attenuation. This method provides the benefit that if an alternative powder delivery method than a coaxial nozzle is chosen, such as side-impinging powder flow, the powder concentration map and laser irradiation source can be modified as necessary to produce attenuation for that configuration. Furthermore, as opposed to analytical models to determine the attenuation such as in (Jouvard et al., 1997, Liu et al., 2005), this method enables calculation of the attenuation in a general case, even when non-coaxial nozzles are used for cladding.

The attenuation model is based on a Beer-Lambert approximation (Jouvard et al., 1997) to determine an effective local attenuation coefficient throughout the particle cloud. For a given ray, the amount of laser intensity reaching the substrate can be calculated by multiplying the effective localized calculated attenuation from the laser source to the substrate, as shown in equation (2.30)

$$I_{att} = I_o \prod \exp(-\alpha_i \Delta z) \tag{2.30}$$

where I_o is the raw laser beam intensity, α_i is the local attenuation factor based on the particle concentration from the CFD model over the region with length Δz, and I_{att} is the attenuated laser intensity through a region with a thickness $\sum \Delta z$. The beam attenuation was calculated for 100 points across the laser beam diameter; however, this will only provide a set of points that need to be interpolated to determine the beam intensity for a boundary condition for the cladding model,

and increases computational effort when compared to a mathematical function. Thus, a neural network was trained to acquire a continuous function of the attenuation as a function of the radius and stand-off distance, enabling a variety of combinations of cladding beam diameters and nozzle stand-off distances to be simulated. Calculated local attenuation coefficients were extracted in 0.1 mm slices along the nozzle axis and 0.0862 mm radially, spanning 10 mm along the nozzle axis and 1.25 mm radially with the data centered at the powder focal point. Using MATLAB, a feed-forward neural network (FFNN) was configured with 120 hidden nodes to calculate the local attenuation using the radial and axial location. To train the FFNN, 50% of the attenuation data was used as training data and the remaining data was used for validation.

Process parameters for the modeling of the deposition process of Stellite-6 powder on mild steel were selected based on a single-track clad: 648W laser power with 960 μm beam diameter, scanning speed of 15 mm/s and a powder feed rate of 25 g/min and 12 mm stand-off distance. Thermal and mechanical properties used within the analysis for Stellite-6 and mild steel are shown in Table 2.11 and Table 2.12

Table 2.11: Thermal and physical properties of mild steel (Nandan et al., 2007, Seli et al., 2010, Seibold et al., 2000, Park and Rhee, 2001, Nishi et al., 2003)

Property	Units	Solid phase	Liquid phase
Density	kg/m^3	7870	7870
Specific heat	J/kg-K	470	470
Thermal conductivity	W/m-K	43	34
Liquid viscosity	kg/m-s	-	5.0e-3
Thermal expansion coefficient	1/K	14.5e-6	
Absorptivity	-	0.37	
Latent heat	J/kg	2.72e5	
Solidus temperature	K	1588	
Liquidus temperature	K	1727	
Surface tension	N/m	1.65	
Surface tension coefficient	N/m-K	-4.3e-4	

Table 2.12: Thermal and physical properties of Stellite-6 (H.-J. and Kim, 1999, Hultgren and Desai, 1973, Bedenko et al., 2016, Katinas et al., 2021, Jouvard et al., 1997, Lemoine et al., 1993)

Property	Units	Solid phase	Liquid phase
Density	kg/m^3	8480	8480
Specific heat	J/kg-K	423	688
Thermal conductivity	W/m-K	14.82	45
Liquid viscosity	kg/m-s	-	5.0e-3
Thermal expansion coefficient	1/K	8.9e-6	
Absorptivity	-	0.47	
Latent heat	J/kg	2.45e5	
Solidus temperature	K	1588	
Liquidus temperature	K	1630	
Surface tension	N/m	1.65	
Surface tension coefficient	N/m-K	-3.4e-4	

Using the FFNN representation of the attenuation coefficient, a spatially-dependent representation of the laser intensity field at the given stand-off distance is applied as a boundary condition to the surface of the substrate, where powder is added at room temperature to quench the molten pool. This method serves a significant purpose: The laser energy reaching the surface can be applied without needing to determine the fraction of energy used to heat the particles, thus bypassing a step to determine individual particle temperatures, which would require accounting for particles shadowing the laser intensity of other particles and/or the substrate. Physically, the energy not reflected away by the particle cloud is used to heat the particles, or pass through the particle cloud and either reflect from or absorb into the substrate. By adding the energy to the substrate directly and modeling the powder concentration to allow mass addition only where the substrate surface exceeds the liquidus temperature, individual particle temperatures do not need to be calculated directly, but rather, added mass is used to quench the molten pool to the point the substrate surface remains above the liquidus temperature. Since the total energy being added to the substrate is either from the attenuated beam or from the effective contribution of heated powder adhering to the substrate surface, this method maintains the energy balance. In the event the cladding process is mass-limited (i.e. more laser energy is available at the substrate surface than

powder to be absorbed), the substrate will experience sub-surface melting, whereas in energy-limited cladding, mass will be added to the surface with minimal substrate melting.

Powder concentration using a 25 g/min powder flow rate was simulated to obtain a steady-state representation of the particle concentration throughout the gas domain, as shown in Figure 2.39. From the simulation, a powder focal plane was observed at approximately 12 mm below the nozzle, and consisted of a powder waist diameter of approximately 2.0 mm, similar to the observation during experimentation with the nozzle (Figure 2.38).

Particle Concentration (kg/m^3)
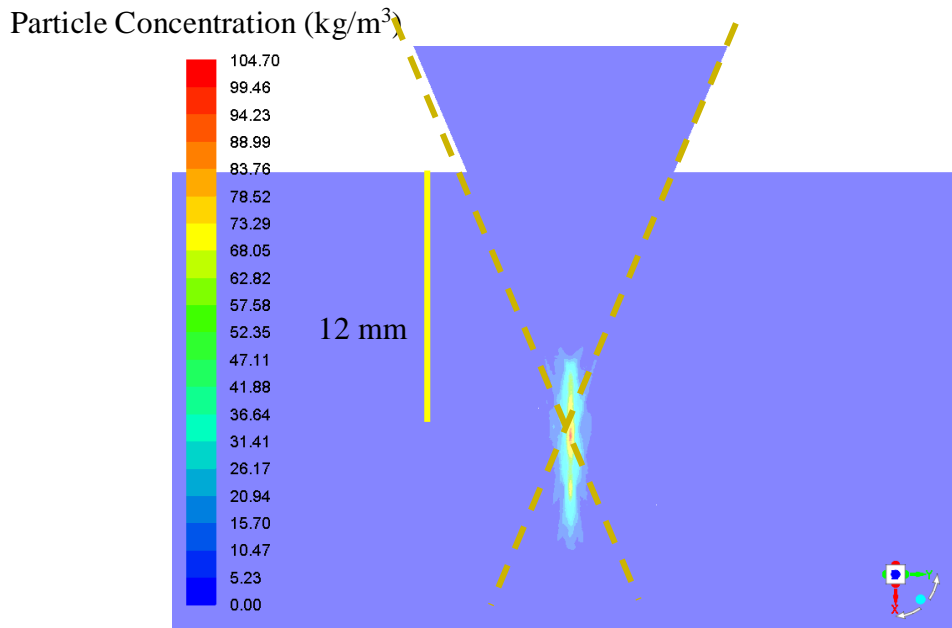
Figure 2.39: Particle concentration distribution with 96 µm mean diameter particles

From the powder profile, a scattering calculation was performed to obtain localized laser attenuation spatially within the particle cloud. A neural network (NN) representation of the local laser attenuation factors was generated from a set of training data composed of 50% of the model-generated attenuation factors and compared to the attenuation coefficients calculated from the local powder concentrations of the computational fluid dynamics model, as shown in Figure 2.40. The highest amount of laser attenuation is found near the center of the beam, which is consistent with the highest particle concentration predicted by the model, whereas attenuation becomes less as the distance from the beam center. The results of the NN show that the overall trends of the laser attenuation profile clearly resemble that of the direct calculation of laser attenuation from the CFD

model. Using the NN-based calculation, a uniform profile beam (from the manufacturer's data sheet) was attenuated through the particle cloud using parallel rays spaced 2 μm apart and aligned coaxially with the laser beam to determine the laser intensity upon emerging from the particle cloud, with the result being shown in Figure 2.41. By integrating the local attenuation factors within Figure 2.41, the overall beam attenuation was calculated and used to reduce the energy input from the uniform laser source within the cladding model. From the scattering calculation, it was found that 67% of the laser intensity sourced from the laser would reach the substrate, while the other 33% is scattered by the particles.
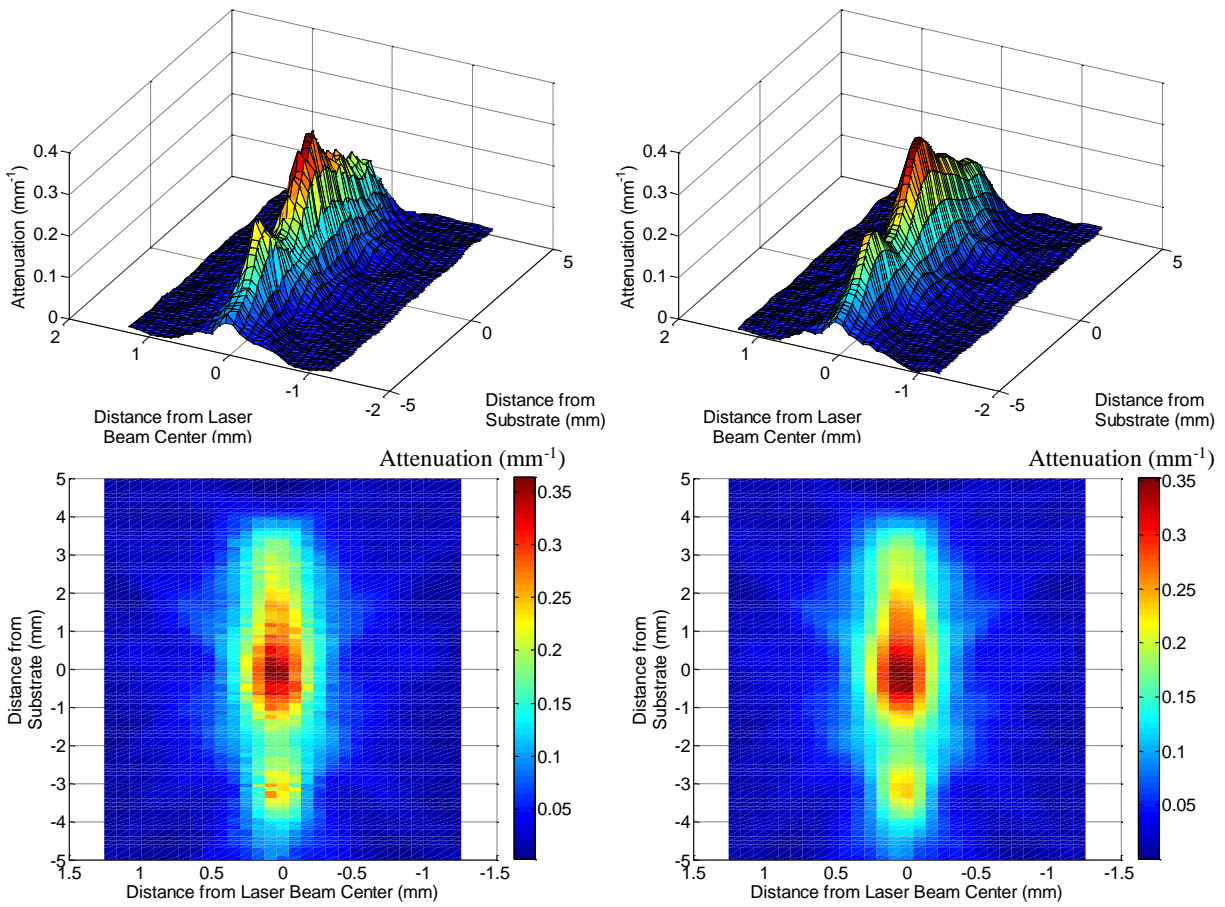
Figure 2.40: Original attenuation map (left) and neural network representation (right)
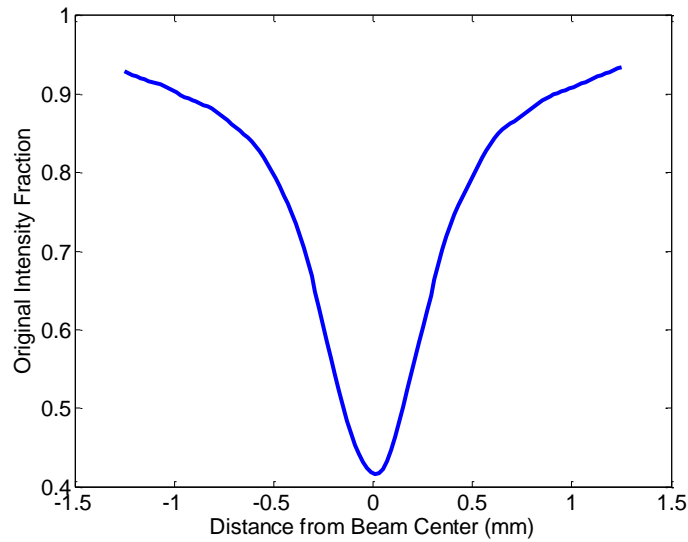
Figure 2.41: Fraction of intensity emerging from particle cloud with the top hat beam profile

Process parameters for the modeling of the deposition process of Stellite-6 powder on mild steel were selected based on a single-track clad with minimal dilution: 648W laser power with 960 μm beam diameter, scanning speed of 15 mm/s and a powder feed rate of 25 g/min and 13 mm stand-off distance. Figure 2.42 shows the results obtained from the cladding model once the clad height and temperature profiles reached their steady-state shape. A deviation of less than 4 μm in the molten pool profile was observed, while the clad profile deviation was less than 40 μm. A comparison of the modeled and visually determined heat-affected zone was also performed, but since the sample was not etched, an uncertainty region was drawn and compared to the heat-affected zone temperature contour obtained from the model.
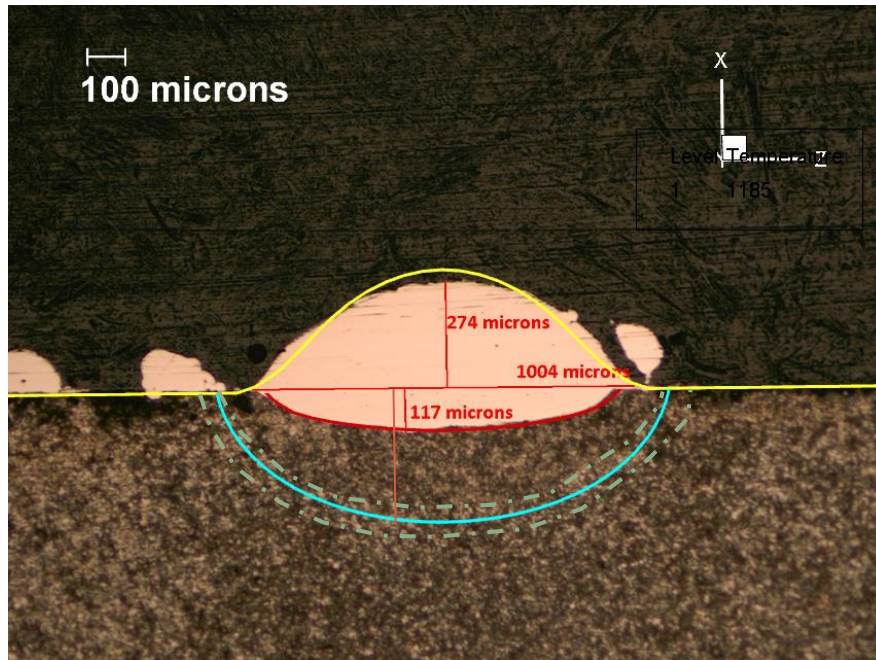
Figure 2.42: Cladding model result at 648W laser power with 960 µm beam diameter, scanning speed of 15 mm/s, 25 g/min powder feed rate, and 13 mm stand-off distance. (yellow=free surface, red=molten pool boundary, blue=HAZ boundary)

To ensure the model was independent of the process conditions, a second track with less dilution was modeled. Process parameters were changed to 550W laser power with 880 µm beam diameter, scanning speed of 15 mm/s and a powder feed rate of 25 g/min and 15mm stand-off distance. Results obtained from the simulation are compared with two separate cross-sections of the single-track experiment in Figure 2.43. It can be observed that variability exists within the experimental data for the track; thus the model should be considered to provide an average view of the cladding process for a given condition. For the second simulation, the amount of dilution is overpredicted by the model for both experimental cross-sections (50 µm), although the clad height and heat-affected zone profiles are within 100 µm of both experimental profiles.
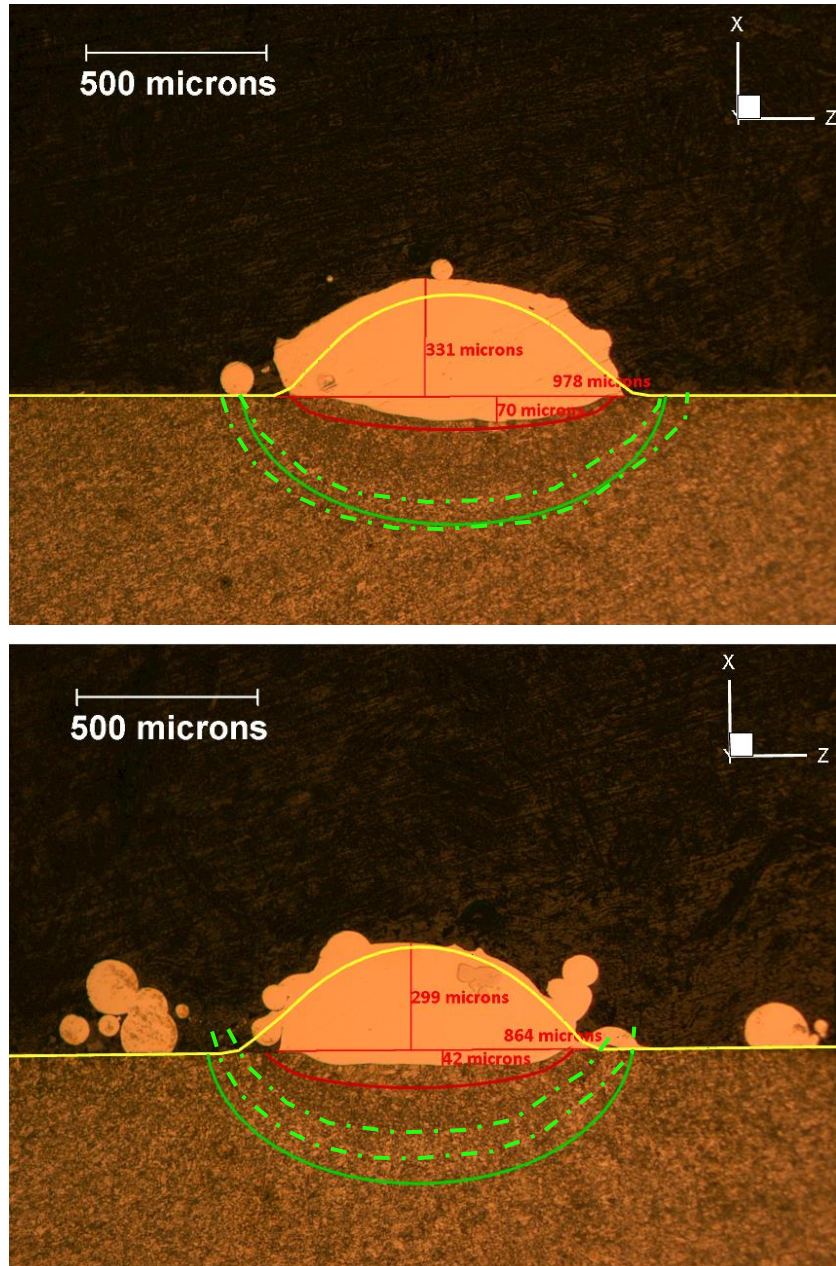
Figure 2.43: Cladding model result at 550W laser power with 880 μm beam diameter, scanning speed of 15 mm/s, 25 g/min powder feed rate, and 15 mm stand-off distance. (yellow=free surface, red=molten pool boundary, green=HAZ boundary)

The validated cladding model was used to determine cooling rates throughout the substrate and cladded single track for the case shown in Figure 2.44. Adjacent to the molten pool region, cooling rates in excess of 10^4 K/s can be observed, whereas at the austenitic phase transformation temperature (1023 K), cooling rates are sufficient to allow for the formation of martensitic steel

92

upon substrate cooling. This region of phase transformation, which is visible in etched samples, is able to explain why hardness within the substrate will vary from the original substrate hardness since laser heating and cooling during the cladding process will locally affect the substrate's microstructure.
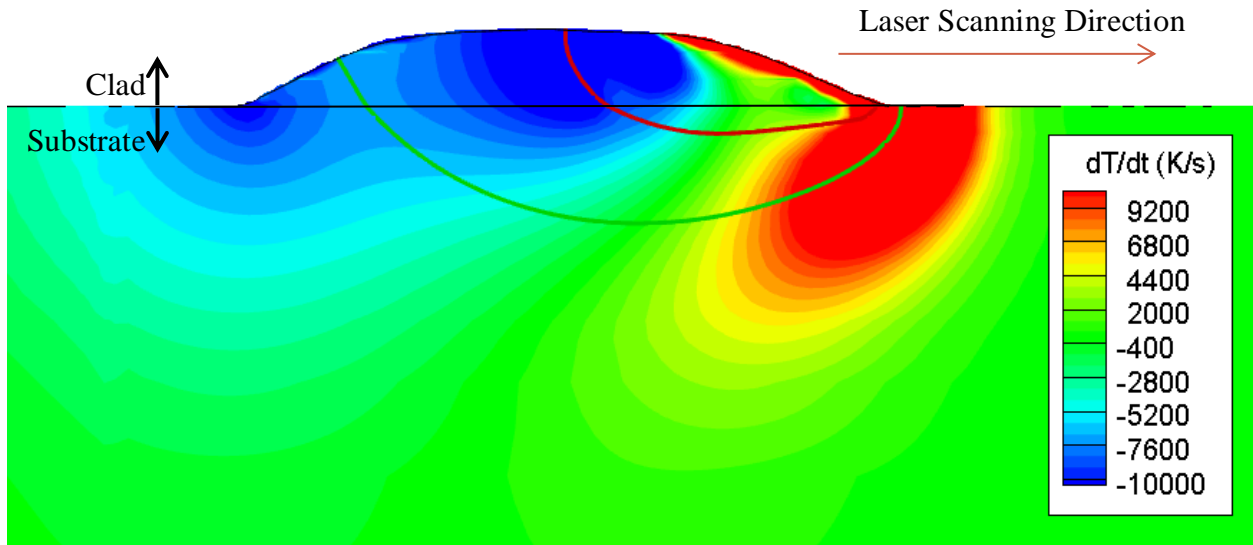
Figure 2.44: Temperature heating/cooling rate contour plot of validation case from Figure 2.42 with molten pool boundary line (red), austenite starting temperature line (1023 K) (green)

Mild steel had been selected as a surrogate material due to similar thermal and physical properties when compared to HY80, and showed that if such a surrogate is selected appropriately, material cost and waste can be reduced to identify process parameters suitable for cladding of the desired material. During the initial investigation, a beam diameter less than the powder waist diameter had been used, which though not optimal, was able to produce single-track clads with low dilution. However, as this was extended to multi-track cladding, the potential for unheated powder to impact the molten pool increased and causes excessive porosity and surface roughness. Even with increasing laser power in an attempt to absorb powder, if the laser beam diameter isn't aligned with the powder focal diameter, higher surface roughness and the potential for increased dilution would result. When performing the laser spot adjustment study, an increase in powder catchment was seen in the limited range of 0.55 mm to 1.01 mm laser spot diameter and was expected to continue until the beam diameter was the same size as the powder focal spot. Increasing the laser focal spot diameter beyond that of the powder focal diameter would cause

laser energy to be wasted since there would be no more powder for the laser irradiation to interact with. The decrease in energy density with increasing laser spot size could also, while not seen in the experiment shown here, limit the melting of powder and reduce powder catchment. By modeling the cladding process with three distinct models which link to each other at the process level, each physical interaction can be investigated independently, regardless of the powder delivery system, laser beam shape, or distance between the laser beam and powder focal planes. The information from one model becomes used as a boundary condition for the next, and is practical for systems in which particle spray is both sparse and either cleanly absorbed or reflected by the substrate. Results obtained by the cladding model provide substantiation that the method used to model the process is reasonable, and could be used for modeling additional cladding material pairs. Even more importantly, the model was shown to be capable of obtaining temperatures and cooling rates throughout the process to understand the impact of the cladding process on the original substrate and solidified clad. For example, in the validation scenario, even though the dilution was found to be 117 μm, a phase transformation occurred up to 372 μm within the mild steel substrate, which can affect the strength and durability of the as-cladded product. In mild steel, a martensitic phase results from the cladding process, and yields a higher strength material than a corresponding forged component; however, certain materials, such as Ti-6Al-4V, experience a ductility reduction with even moderate cooling rates (Liu and Shin, 2019). Thus, care must be taken when considering using laser cladding for repair operations to prevent damage to the base material. Rather than obtaining temperature and cooling rate information experimentally, an effort which requires substantial cost and time, modeling and post-processing the results of a predictive model can be used to provide insight into material behavior of the substrate during the cladding process, as was demonstrated in this study.

Cladding of Stellite-6 on an HY80 substrate was successfully performed by developing process parameters on a surrogate substrate with similar material properties. When selecting constant parameters for cladding of multi-track (single-layer) clads, it is necessary to have at least some amount of dilution to ensure that subsequent cladded tracks adhere to the surface without porosity. Additionally, the coaxial powder feed system used in this study provided the most favorable clads when the beam diameter and powder focal diameters were similar in size. The cladding model presented showed that for different process conditions, the amount of error associated with the geometry and temperature field predictions was within the uncertainty of the

experimentation, and is able to acquire additional information about mass flux and energy flux in the event nozzle stand-off distance and/or beam diameter is varied.

CHAPTER 3.   LASER POWDER BED FUSION ADDITIVE MANUFACTURING PROCESSES

This chapter describes a model to predict the initial transient behavior of an L-PBF process using a volumetric heat source to track particle melting, and has been coupled to a laser welding model to predict the process of keyhole formation during processes with significant surface evaporation. As opposed to other models using a volumetric heat source, this model tracks individual particle temperatures in a relatively thick powder bed and couples the mass addition to a full-physics computational fluid dynamics model to predict molten bead and keyhole geometry throughout the L-PBF process. The method described herein is able to account for energy from an arbitrary beam profile on an arbitrary powder bed arrangement (both single-layer and multi-layer arrangements), and allows for energy to pass directly through to the substrate in the event of a localized void created by thin or sparse powder beds, as would be observed during powder bed fusion. Validation of the model is performed against experimentation which used a stationary laser irradiation source to guarantee highly localized powder bed melting and sufficient powder and surface evaporation. Hence, in this chapter, a spatial energy distribution is used on a physically-representative powder bed to track particle temperatures independently, which enables prediction of the highly transient process of powder melting on the substrate surface without the need for additional assumptions for arbitrary process parameters, including powder bed thickness, scanning speed and laser profile.

3.1   Methodology

The general process to model powder bed fusion processes resembles that of modeling blown powder AM systems with minimal differences, as shown in Figure 3.1. The differences between the processes are the focus of this section, and are described in addition detail within subsections 3.1.1 through 3.1.5. In blown powder processes, the laser fluence (power per unit area) is typically low enough to prevent significant material evaporation at the surface, thus keyhole dynamics do not need to be considered. However, powder bed fusion processes use laser beam diameters which are typically smaller than those found in blown powder processes; thus, increasing the laser fluence and the potential for material evaporation to drive molten pool dynamics.

The model is segmented into 2 primary components: (1) a powder bed placement model using discrete elements to model powder particle interaction for the initial powder bed configuration, and (2) a multi-phase laser welding model to investigate the powder and energy addition to the substrate surface and model the complex dynamics associated with laser-powder and laser-substrate interaction. The following subsections describe the methods used to develop the model.
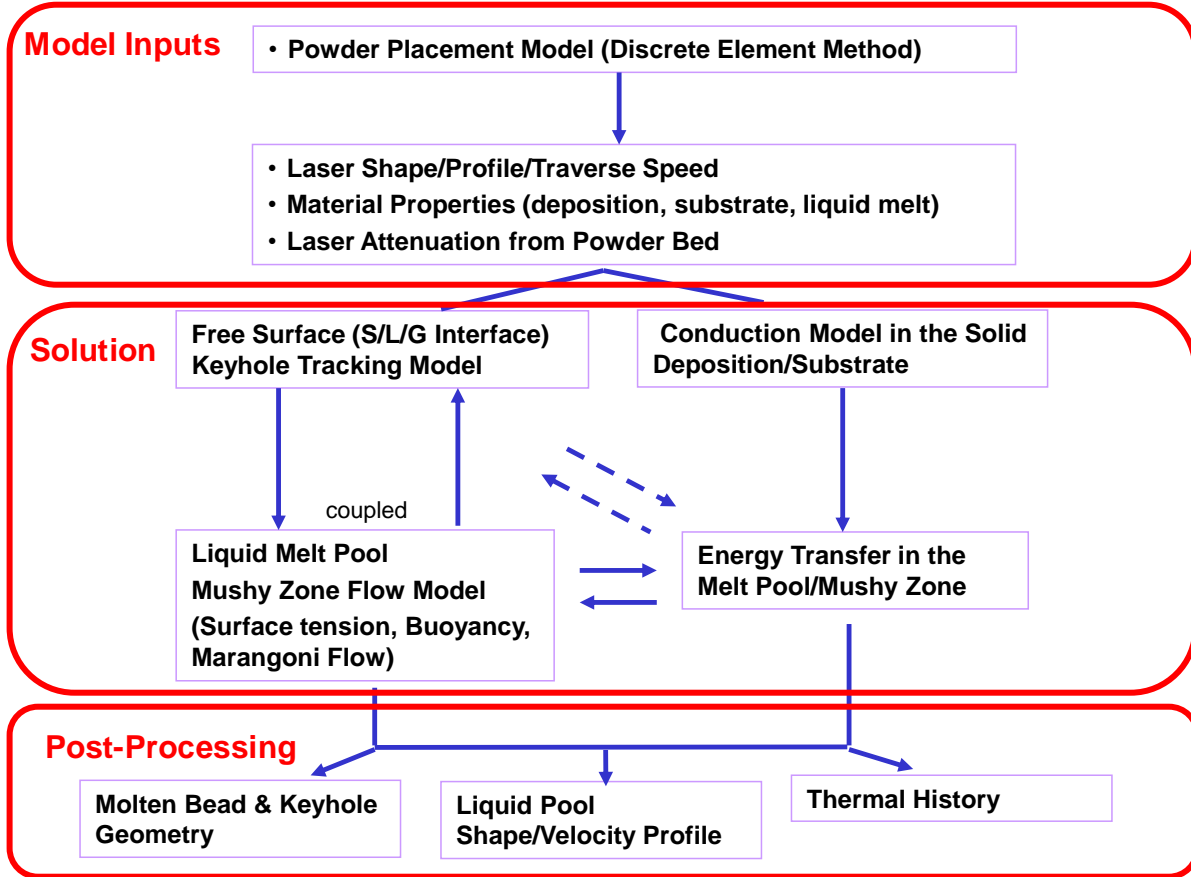
Figure 3.1: Solution flow diagram for powder bed fusion AM processes

3.1.1   Modeling of the Powder Bed Process

Because of the potential for high laser fluence, it becomes necessary to model evaporative effects and how the molten pool shape is changed. The laser welding model of Tan and Shin was used as the starting point of the powder bed modeling effort, with details of the model outlined in (Tan and Shin, 2014). Tan and Shin's model is a full-physics conservation model describing the keyhole welding process using a sharp interface method. The Ghost Fluid Method (GFM) (Fedkiw

et al., 1999) is used to model a sharp interface between the gaseous and liquid/solid domains. By accounting for the jump condition at the interface (which is tracked via the levelset method (Osher and Sethian, 1988)), the governing equations can be applied to each of the subdomains, and interactions at the free surface can be applied to each of the domains as a boundary condition. Modeling of the L-PBF process is performed by solving mass, momentum, energy, and species governing equations throughout the computational domain, as shown in equations (3.1) through (3.4) (Tan and Shin, 2014).

$$\frac{\partial \rho}{\partial t} + \nabla \cdot (\rho \boldsymbol{V}) = \dot{S}_{mass} \tag{3.1}$$

$$\frac{\partial (\rho \boldsymbol{V})}{\partial t} + \nabla \cdot (\rho \boldsymbol{V} \boldsymbol{V}) = -\nabla P + \nabla \cdot (\bar{\bar{\tau}}) - \frac{\mu \boldsymbol{V}}{K} + \frac{\partial \gamma}{\partial T} \nabla_s T \delta(\varphi) + \rho \vec{\boldsymbol{g}} \beta (T - T_{ref}) + \dot{\boldsymbol{S}}_{mom} \tag{3.2}$$

$$\frac{\partial (\rho h)}{\partial t} + \nabla \cdot (\rho \boldsymbol{V} h) = \nabla \cdot (k \nabla T) + \dot{S}_{energy} \tag{3.3}$$

$$\frac{\partial (\rho \chi)}{\partial t} + \nabla \cdot (\rho \boldsymbol{V} \chi) = \nabla \cdot (D \rho \nabla T) \tag{3.4}$$

where ρ is the density V is the velocity, P is pressure, $\bar{\bar{\tau}}$ is the fluid shear tensor, μ is the viscosity, K is the isotropic permeability through a porous media as described by the Kozeny-Carman equation, γ is the surface tension, $\vec{\boldsymbol{g}}$ is the gravitational vector, β is the coefficient of thermal expansion, T_{ref} is a reference temperature, h is the enthalpy, k denotes the thermal conductivity, T is the temperature, χ is the mass fraction of metallic vapor within the gaseous phase, D is the diffusion coefficient for the metallic vapor within the gaseous phase, and $\dot{S}_{mass}$, $\dot{\boldsymbol{S}}_{mom}$, and $\dot{S}_{energy}$ are source terms for the mass, momentum, and energy equations, respectively. The Dirac Delta function shown in equation (3.2) ($\delta(\varphi)$) uses a levelset function to apply surface-based source terms, such as Marangoni shear stress, only at the interface between gas and metal phases (Tan and Shin, 2014).

The governing equations are solved using a dual-mesh algorithm, in which a fine mesh moving at the laser beam velocity is used to solve fluid dynamics due to evaporation and fluid motion above the substrate surface and within the molten pool, while a coarse mesh is used to solve for heat transfer effects between the fine mesh region and the remainder of the substrate.

3.1.2 Discrete Element Method for Powder Placement and Interaction

The powder bed initial placement uses a discrete element method (DEM) model to investigate particle-particle and particle-boundary interactions and provide a physical

representation of the arrangement of individual powder particles during powder placement prior to laser beam irradiation. The DEM model solves for translational and rotational accelerations of each particle within a domain by determining the forces and torques imparted due to interactions between other particles and boundaries (Tsuji et al., 1993). The governing equations for the DEM are force and torque balances, as shown in equations (3.5) and (3.6)

$$\sum_j \vec{F}_{i,j} = m_i \vec{a}_i \tag{3.5}$$

$$\sum_j \vec{\tau}_{i,j} = I_i \vec{\alpha}_i \tag{3.6}$$

where a_i and α_i and the translational and rotational accelerations, respectively, on particle i with mass m_i, and inertia I_i due to imparting forces and torques, $F_{i,j}$ and $\tau_{i,j}$ from interactions with gravity, particles and/or domain boundaries, j. Collision forces were obtained using equations (3.7) and (3.8) for the normal and tangential directions, respectively (Tsuji et al., 1993)

$$F_{normal,i} = -kx_{i,j}^n - 2\gamma\sqrt{m_i k}v_{i,j}^n \tag{3.7}$$

$$F_{tang,i} = -kx_{i,j}^t - 2\gamma\sqrt{m_i k}v_{i,j}^t \tag{3.8}$$

where k is the spring constant of the material, $x_{i,j}^n$ and $x_{i,j}^t$ are the normal and tangential displacements between particles i and j, $v_{i,j}^n$ and $v_{i,j}^t$ are the relative normal and tangential velocities between particles i and j, and γ is the coefficient of viscous damping determined from equation (3.9) (Tsuji et al., 1993)

$$\gamma = \frac{-\ln(r)}{\sqrt{\pi^2 + \ln(r)^2}} \tag{3.9}$$

where r is the coefficient of restitution for the particles. It should be noted that contact forces are set to zero for a given particle pair in the event contact between the particles does not exist.

3.1.3 Powder Spreading Processes

Particles spreading processes are a vital aspect of laser-powder bed fusion processes, specifically since commercially-available systems use powder reservoirs to ensure a sufficient amount of powder is available to form a uniform powder layer on the substrate surface (Bhavar et al., 2017). The overall process for obtaining a powder bed that can be used as a starting point for the L-PBF model is described in Figure 3.2. Initially, a powder size distribution is required, as it can play a significant role in the final arrangement of powder placed and spread upon the substrate,

99

not to mention the impact of particle sizes during the irradiation process (Sutton et al., 2017). Particle size distribution can be obtained either experimentally using optical microscopy or based on supplier information; however, the former is a superior method since variances in manufacturing will exist and should be accounted for. Optical microscopy of sparse powder will provide 2-D images which require post-processing via image recognition to identify particle diameters of the sample of powder. By using multiple images, a histogram of the particle diameters can be obtained and used to initiate a simulation for the initial particle placement process, which places particles on the surface of the substrate via the raindrop packing method (Jia et al., 2011) through accelerating particles from gravitational acceleration. Once particles have negligible velocity, the powder arrangement is stored for use to simulate the first spreading pass. Though simulations for particle spreading commonly utilize a rectangular blade mechanism, the spreading bar used in simulations for this research has a circular cross-section to reduce the effort of describing multiple moving boundaries, and instead can be expressed as a moving cylindrical "particle" with a large mass. Once a single spreading pass has been performed, the resulting powder bed will change from the original powder placement by increasing packing density via rearrangement of the smaller particles where voids in large particles are observed. Additional spreading passes may be required to replicate a given experimental setup, and can be simulated using the final simulation result of a previous spreading pass. If after any subsequent spreading pass, the powder bed height remains unaffected, additional passes are not necessary.
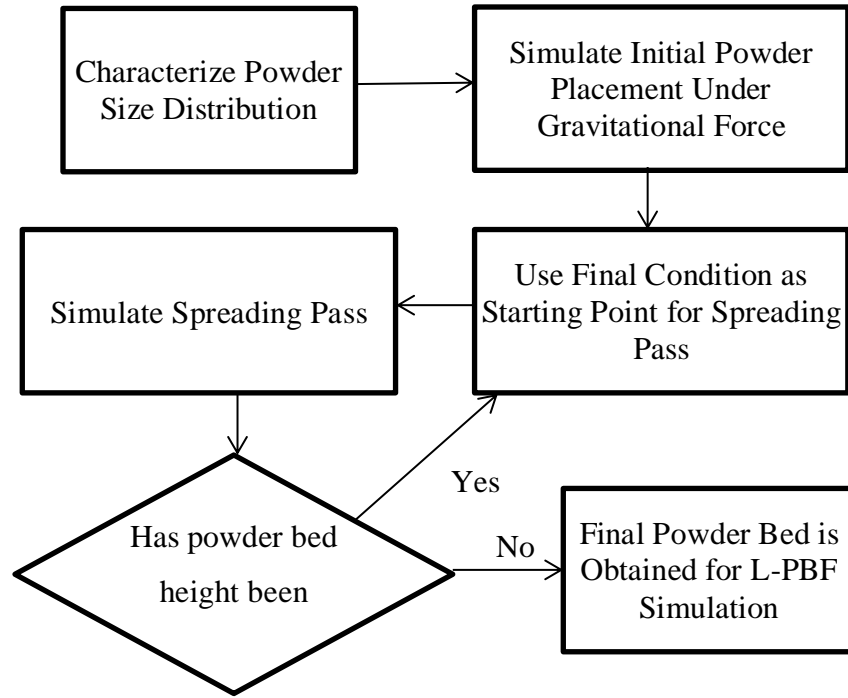
Figure 3.2: Diagram of Powder Spreading Process Simulation

In each step of the simulation, care must be taken to ensure the critical time step of the DEM model is not exceeded (Burns et al., 2019), which will lead to numerical instability and result in excessive particle acceleration of the smallest particles used. The most commonly used criterion for the time step is based on the square root of the ratio of the stiffness and mass of a given particle to ensure that discretization of the equations of motion is not violated during time advancement (Belytschko and Hughes, 1983). Unfortunately, using material-based spring constants would necessitate time steps which would be too restrictive to perform meaningful simulation of the powder bed; thus, the spring constant is typically reduced by several orders of magnitude to reduce collision-based forces from particle overlap (Silbert et al., 2001). Even with such an assumption, small particles (<2 μm) continue to require restrictive time steps and provide insignificant mass addition during L-PBF, providing the case to exclude them from the simulation.

3.1.4   Laser Energy Distribution in Powder Bed

The next consideration is the handling of the laser-particle and laser-substrate interaction. Optical penetration depth (OPD) of laser irradiation of a powder bed is known to be a function of

the powder size and particle arrangement (Wang et al., 2002). For fully dense metals, the penetration depth is typically on the order of 100 nm, while powder beds have been shown to have an OPD of a similar order of magnitude of the powder bed depth (Wang et al., 2002). From King et al. (King et al., 2015a), the total absorptivity of the powder bed was determined based on similar particle size, though with a different powder bed thickness. As particles melt and adhere to the substrate, the effective thickness of the powder bed will decrease, which in turn, changes the distribution of energy absorbed by the particles and energy transmitted through to the substrate. To mitigate this issue, laser energy is added to the powder bed volumetrically, rather than using a more computationally expensive ray tracing model (Boley et al., 2015), and is done so using a Beer-Lambert attenuation law (King et al., 2015a, Gusarov and Kruth, 2005) as shown in equation (3.10)

$$I_{eff}(z) = I_o \exp(-\alpha z)$$

(3.10)

where I_{eff} is the effective laser irradiation at a depth z from the powder bed surface, I_o is the laser intensity at the surface, and α is the effective optical penetration depth of the powder bed. To allow for a Beer-Lambert curve fit such that implementation of a volumetric heat source could be implemented, an effective absorption coefficient of Ti-6Al-4V powder was required. From Criales and Özel, the value for the OPD was 500,000 cm^{-1} (Criales and Özel, 2017), indicating the laser beam intensity would only penetrate the top particle of the powder bed. This was compared to the effective absorptivity from the ray tracing model presented in (Boley et al., 2015), which was fitted to an exponential decay to obtain the OPD of the powder bed for similarly sized particles (70000 m^{-1} at an absorptivity of 0.64), and is expected to provide a more representative energy distribution through the depth of the powder bed.

Energy addition to each individual particle must be considered to provide the most representative portrayal of the laser-particle interaction; thus, an algorithm was developed to allow for heating of particles depending on both the distance from the laser beam center axis as well as the particle's distance from the surface of the powder bed. Since the laser intensity from the experimental data varies in a Gaussian distribution from the beam center axis, a radially symmetric profile for the beam intensity is used, as shown in equation (3.11)

$$I_{laser}(r) = \frac{2P_{laser}}{\pi R^2} \exp\left(-\frac{2r^2}{R^2}\right)$$

(3.11)

where I_{laser} is the laser beam intensity at a radial distance r from the beam center axis, P_{laser} is the laser power, and R is the effective beam radius.

A slicing algorithm was developed to identify the amount of energy that should be added to a given particle based on its spatial location and its depth from the surface of the powder bed. The concept uses rectangular prismatic columns parallel to the laser beam axis to determine the mass of each particle contained within a region of laser intensity and to provide the effective contribution of that mass for the energy absorption, as defined by the following algorithm:

1) Identify the particle centroid location and map the amount of mass from each particle with mass m_p to a column (i,j), storing the contribution of each particle in each column in a matrix $\boldsymbol{m}(i,j,p)$.

$$\boldsymbol{m}(i,j,p) = m_p \ located \ in \ column \ i,j$$
(3.12)

2) Determine the maximum particle bed height $z(i,j)$ for each column (i,j), using the centroids and radius of each particle, where the contribution of particle p in $\boldsymbol{m}(i,j,p)$ is non-zero. The amount of laser energy reaching the substrate within column (i,j) can be found using equation (3.10).

3) Weight the amount of mass of each particle within each column as a function of the distance of the particle centroid from the particle bed height, per equation (3.13)

$$\boldsymbol{W}(i,j,p) = \boldsymbol{m}(i,j,p) * \exp(-\alpha z(i,j))$$
(3.13)

4) The amount of energy added to particle p in column (i,j) is found by multiplying the available laser energy $\boldsymbol{E_{laser}}(i,j)$ absorbed by the particles by the fraction of the weighting function $\boldsymbol{W}(i,j,p)$ to the summation of the weighting function in column (i,j), as shown in equation (3.14).

$$\boldsymbol{E}(i,j,p) = \boldsymbol{E_{laser}}(i,j) * \frac{\boldsymbol{W}(i,j,p)}{\sum_{k=1}^{p} \boldsymbol{W}(i,j,k)}$$
(3.14)

5) Determine the total amount of energy $(\boldsymbol{E_{add}})$ added to particle p by summing the contribution from each column

$$\boldsymbol{E_{add}}(p) = \sum_{\substack{1 \leq i \leq N \\ 1 < j < M}} \boldsymbol{E}(i,j,p)$$
(3.15)

From a practical perspective, the size and location of the grid used to perform the slicing algorithm should coincide with the fine mesh used for the solution of the governing equation. Figure 3.3 shows a top view of a hypothetical two-layer powder bed using the prismatic columns arranged in Cartesian axes. For thicker powder beds, each column will likely contain some amount of particle mass as shown in the figure; however, in the case where no powder mass is encompassed within a column, the algorithm will allow all energy to pass through to the substrate directly.
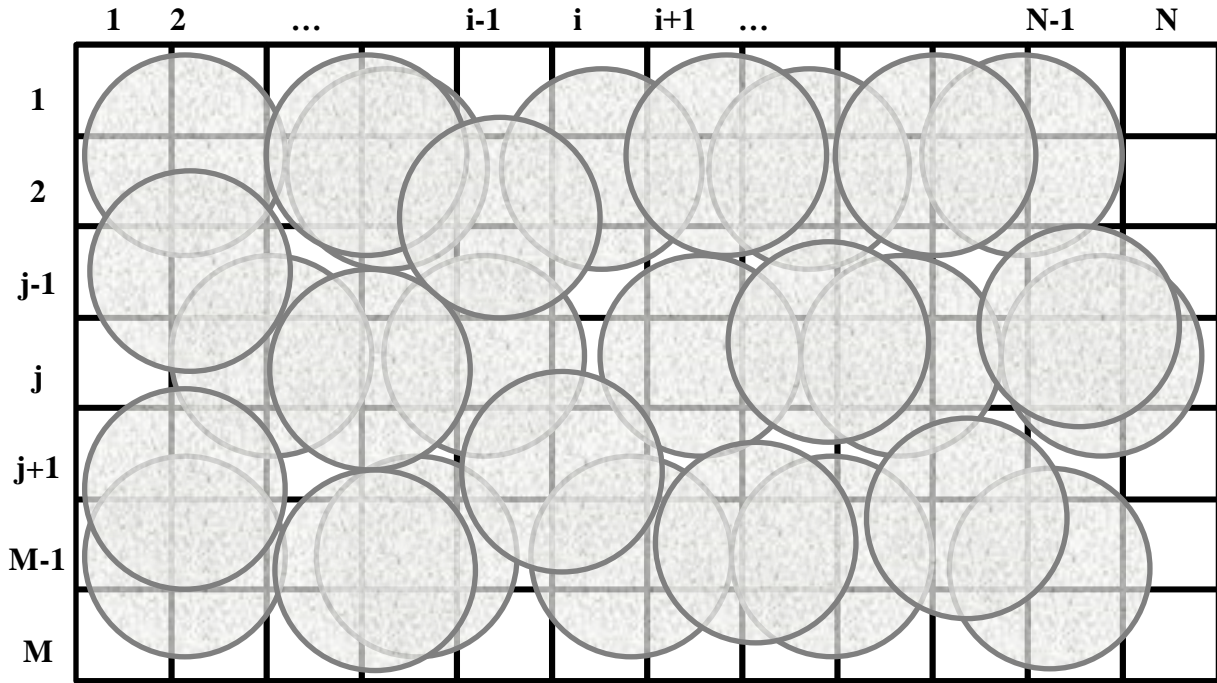
Figure 3.3: Example of particle arrangement within structured mesh (top view)

This algorithm assumes that the powder bed attenuates the laser beam by the same attenuation factor (α) regardless of the amount of mass spanning into each column, unless no mass is present within a given column. Furthermore, heat conduction within the powder bed is considered negligible, since the amount of contact area between adjacent particles is small compared to a bulk substrate, thus limiting energy transfer by direct irradiation only. By assuming minimal contact area between particles, the effective thermal conductivity of the powder bed is nearly that of air; thus, energy added to a given particle is used solely to heat the particle, with the assumption that they can be modeled as lumped capacitance masses.

The final step in linking the powder bed model to the laser welding model is to account for molten mass addition to the substrate while simultaneously removing it from the powder bed particles. This is performed by accommodating phase change of the particles as they are being irradiated, with the energy added to each particle to determine the effective enthalpy of the particle and assess what amount of a given particle, if any, could be molten. This is a two-step process: (1) calculate the final enthalpy of a given particle to determine if the enthalpy exceeds the enthalpy at solidus temperature, (2) calculate the amount of molten mass if the particle exceeds solidus temperature. To simplify the analysis, it is assumed that as the particle heats up and mass is shed to the surface, the particle will maintain a spherical shape. The final enthalpy of each particle is determined from an energy balance between the added laser energy, as shown in equation (3.16).

$$m_p\left(h_{p,t} - h_{p,0}\right) = \boldsymbol{E}_{add}(p)$$

(3.16)

where m_p is the mass of a given particle with the initial and final enthalpy of $h_{p,0}$ and $h_{p,t}$, respectively after adding the energy from the slicing algorithm ($\boldsymbol{E}_{add}(p)$). The amount of mass shed by a given particle is then determined via simultaneous solution to equations (3.17) and (3.18)

$$m_{melt} h_{liq} + m_{sol} h_{sol} = m_p h_{p,0} + \boldsymbol{E}_{add}(p)$$

(3.17)

$$m_{melt} + m_{sol} = m_p$$

(3.18)

where h_{liq} and h_{sol} are the enthalpy of the particle's material at liquidus and solidus temperatures, respectively, and m_{melt} and m_{sol} and the molten and solid mass of the particle, respectively. The molten mass is then shed from the particle and added to the free surface of the substrate, via a levelset source per equation (3.19)

$$f_p(i,j) = \frac{\dot{m}_{melt}(i,j)}{\rho A_\perp}$$

(3.19)

where $f_p(i,j)$ is the levelset source term (free surface velocity) due to the addition of $\dot{m}_{melt}(i,j)$ of molten mass rate in column (i,j), and $A_\perp$ is the cross-sectional area of the column. Similarly, energy addition is a function of the mass addition, and can be expressed via equation (3.20).

$$\dot{E}_{add,surf}(i,j) = \dot{m}_{melt}\left(h_{liq} - h_{disp}\right)$$

(3.20)

where $\dot{E}_{add,surf}(i,j)$ is the energy added below the free surface in column (i,j), and h_{liq} and h_{disp} are the enthalpy of the powder at its liquidus temperature and the gas above the free surface, respectively.

As the gas phase is displaced by the added molten powder, changes of the free surface are tracked and the impact of the free surface motion due to powder addition is incorporated as source terms for the momentum and energy governing equations. Since a GFM-based solver is used to solve the governing equations, as the free surface location changes, the solver partitions the low and high density phases with the levelset function; thus, no explicit mass or species source terms are applied, and instead mass and species change at the interface is calculated based on the temporal change of the levelset free surface. On the other hand, energy and momentum source terms must be applied to incorporate the respective contributions to their governing equations, and are shown in equations (3.21) and (3.22), respectively.

$$\dot{S}_{energy} = \frac{\dot{E}_{add,surf}(i,j)}{A_{\perp}\delta} \tag{3.21}$$

$$\dot{S}_{mom,i} = \frac{\rho_{metal}V_{metal,add,i}(i,j)f_p}{\delta} \tag{3.22}$$

where $\dot{S}_{energy}$ and $\dot{S}_{mom,i}$ are the source terms for the energy and momentum equations, respectively, δ describes a distance perpendicular to the free surface in which the quantities are added based on the levelset function (set to 15 μm to apply the source term over the length of one control volume in the fine mesh for these studies), and $V_{metal,add,i}(i,j)$ is the velocity of the molten metal as it is being added to the surface. For the simulations performed in this study, powder is assumed to be stationary upon the substrate surface at the time molten material is added, thus making the momentum source term zero.

3.1.5   Dual-Mesh Formulation

A dual-mesh solver (or Arbitrary Lagrangian-Eulerian solver), provides significant benefits over a corresponding single-mesh solver with regard to decreased simulation time. Two distinct meshes are generated, one being a fine mesh in which equations (3.1) through (3.4) are solved with all of the source terms of the energy, mass, energy, levelset equations due to laser heating, powder addition, and evaporation effects, while the other mesh is a coarsely discretized domain where only conduction-based energy transfer is considered. As the laser beam translates throughout the coarse domain, the fine mesh region tracks with the laser beam such that the laser beam center axis location remains unchanged with respect to the centroid of the fine mesh domain.

Typical additive manufacturing components have dimensions in the range of millimeters or larger. Simulation of the process using a single-mesh solver (and further, a uniform grid due to limitations in GEMS), would require excessive computational effort. For example, simulating a 5.0 mm x 5.0 mm x 3.0 mm substrate with a 2.0 mm gas region above using a uniform mesh with regular hexahedral control volumes of edge length 20 μm would require 15.625 million cells. Using a dual-mesh scheme with a fine mesh over 1.5 mm x 1.5 mm x 1.5 mm with the same control volume size as the single-mesh method, and a coarse mesh with control volumes having an edge length of 100 μm yields 125,000 cells in the coarse domain and 421,875 cells in the fine mesh region, or 3.5% of the cell count of the single-mesh solver. Though both solution processes can be parallelized with MPICH/OpenMPI (Gropp and Lusk, 1996), increased memory usage, hard disk storage, and processor load for the single-mesh implementation make a large-scale simulation of laser-powder bed fusion processes infeasible.

The original dual-mesh formulation described in (Tan and Shin, 2014) suffered from several significant limitations which were only observed during large-scale simulations, as would be seen during single-track laser-powder bed fusion scenarios. The first issue was the boundary condition on the leading edge of the fine mesh, which was assumed to be sourced from a room temperature thermal source. If the substrate is sufficiently large, this assumption is reasonable; however, in the case of a multi-track additive manufacturing process, energy accumulation within the substrate will invalidate the assumption. To provide maximum flexibility for the dual-mesh algorithm, the traversing of the fine mesh must accommodate multi-pass patterns, of which only unidirectional scans could be performed within the original formulation. The most critical flaw in the method involved the application of the boundary condition for the fine mesh/coarse mesh interface. In the method used by Tan and Shin, conservation of energy within the fine mesh region was solved using a temperature boundary condition obtained from the coarse mesh region. The resulting temperature field would then be used by the coarse mesh region to acquire boundary temperatures near the interface (via an interpolation scheme), allowing for the energy equation to be bounded on the coarse grid. An explicit time advancement scheme utilizing time steps one tenth of the size of the physical time step of the fine mesh region was implemented, and allowed the temperature field within the coarse mesh region to advance to the same physical time as the fine mesh region. Finally, the temperature for the fine mesh boundary cells was updated via interpolation from the coarse mesh temperature field. Unfortunately, the method described will

not always conserve energy between the fine mesh and coarse mesh regions, especially in the event of large temperature gradients being observed adjacent to the fine mesh boundary. By specifying a temperature boundary condition for both the fine mesh and coarse mesh boundaries, the solution for the temperature field is over-constrained.

To overcome the limitations observed in the original dual-mesh formulation, a method to prevent over-constraining of the temperature field at the boundary was implemented by solving conservation of energy within the fine mesh region and calculating a heat flux at the boundary face. Figure 3.4 provides diagrams of how boundary conditions are defined depending on which domain is being solved. Initially, a temperature defined at each cell of the fine mesh, interpolated from the thermal field within the coarse mesh region, at which point the governing equations within the fine mesh are solved. Using the boundary temperatures, a heat flux is calculated and used as the boundary condition for the coarse mesh, which is solved using a similar explicit time advancement as described earlier. Once the coarse mesh temperature field is solved, the fine mesh boundary temperatures are interpolated again to continue iterating the solution process. To further increase versatility of the dual-mesh algorithm, the capability to handle multi-track laser scans in multiple directions was included for future work with the laser-powder bed fusion model. The most significant limitation imposed by the new dual-mesh formulation is that boundary faces of the fine mesh must be coincident with faces of the coarse mesh; thus, the fine mesh will move one coarse mesh edge distance at a time as opposed to one fine mesh edge distance.
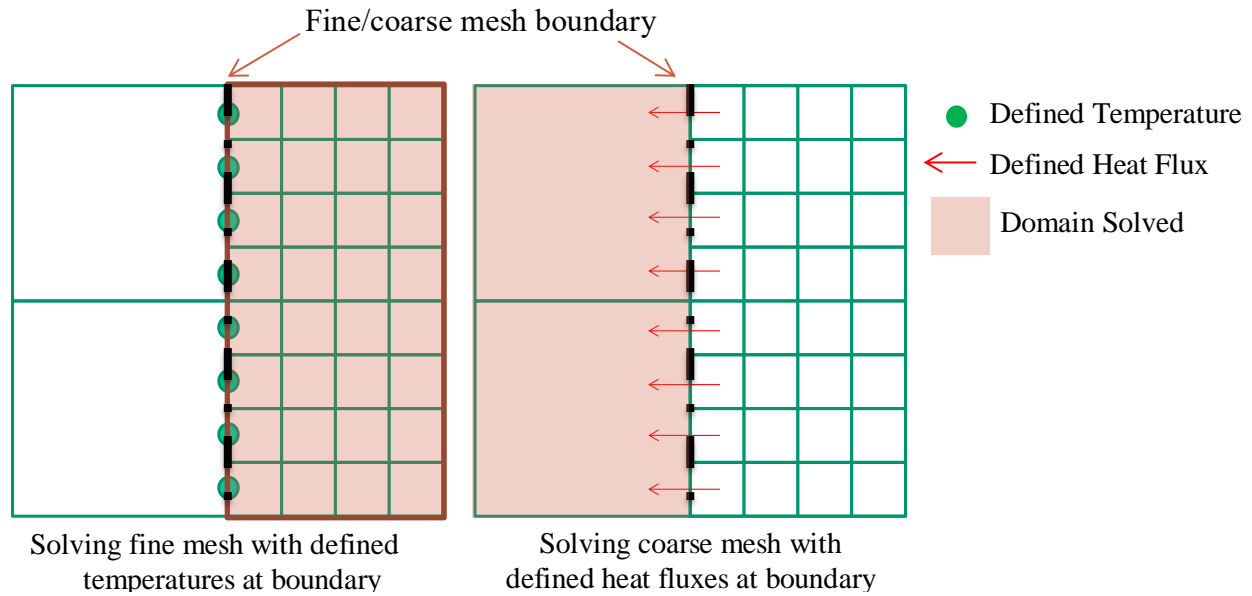
Figure 3.4: Dual-mesh solution strategy diagram

Verification of the method used was performed on a 2.0 mm x 2.0 mm x 5.0 mm substrate in which a six track zig-zag pattern was scanned with an 80.0 W irradiation source with a Gaussian distribution on a mild steel substrate scanning at 25 mm/s and a hatch distance of 0.35 mm. Results of the scan pattern are provided in Figure 3.5 and Figure 3.6, where isotherms are shown for the beginning and end states of each track within both the fine mesh and the coarse mesh. When observing the temperature contours at the boundary between the two mesh regions, the positional error of any given isotherm is less than one fine mesh increment, and is attributed to the interpolation error of the isotherms in the coarse mesh domain during image rendering. It can also be seen in each subfigure that the laser beam is not centered within the fine mesh region at the start or end of a given track. As the laser beam approaches the edge of the substrate, the fine mesh pauses at the boundary (since fine mesh boundary faces must remain congruent with coarse mesh faces at all times) and allows the location of the laser beam center axis to decouple from the centroid of the fine mesh, until such a time that the laser beam traverses in the other direction, at which point, the fine mesh begins moving when the center of the beam is realigned.
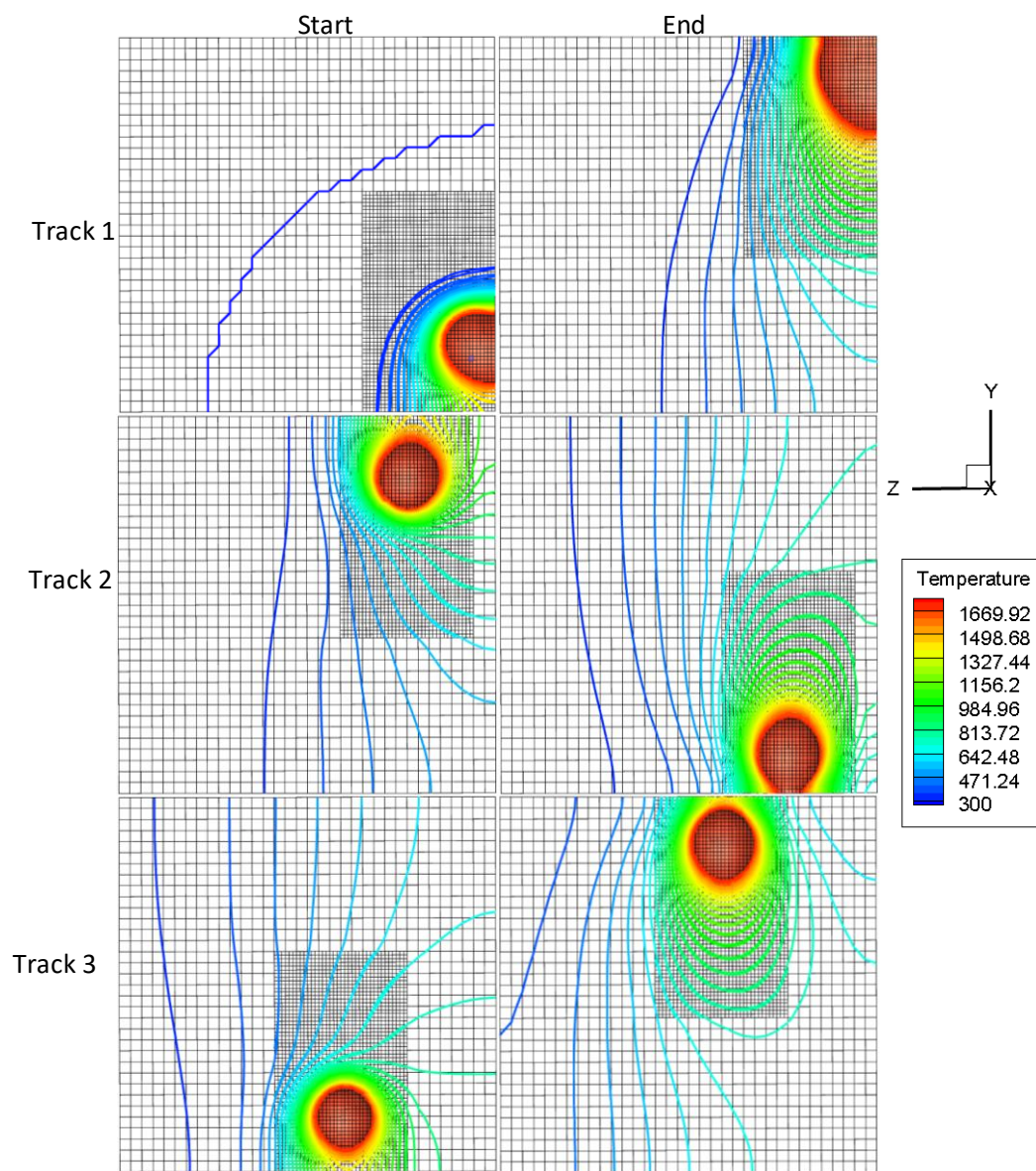
Figure 3.5: Verification of modified dual-mesh algorithm, tracks 1 through 3
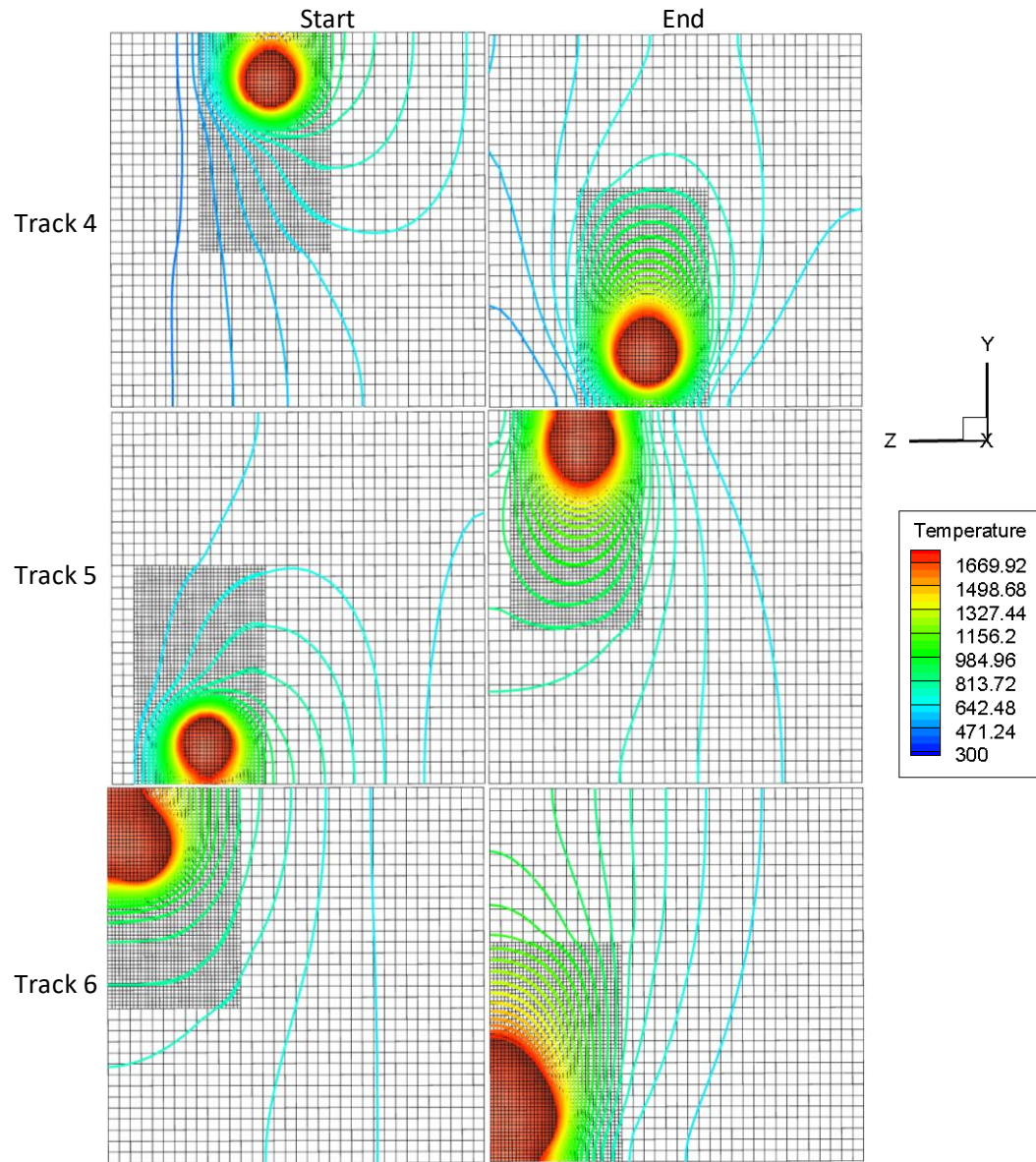
Figure 3.6: Verification of dual-mesh algorithm for laser scanning at 80.0 W, tracks 4 through 6

3.2   Case Studies of Powder Bed Fusion

This section documents validated case studies for the powder bed fusion modeling performed using the aforementioned framework in Figure 3.1.

3.2.1   Ti-6Al-4V Powder Bed Fusion

The validation case is based on the synchrotron experimental results of Zhao et al. (Zhao et al., 2017), which uses a Gaussian beam with spot size 220 µm of two distinct power levels (340 W and 520 W) to melt a 100 µm thick Ti-6Al-4V powder bed, with a powder size distribution between 5 µm and 45 µm and an average particle diameter of 30 µm. A 450 µm wide Ti-6Al-4V substrate with a thickness of 3.0 mm in the direction of the laser beam was used to place the powder bed upon, and was sandwiched between carbon plates which impede the motion of particles and evaporative gas flow beyond the width of the plate.

Still images of the powder bed fusion process were collected via high-speed X-ray imaging, which involves impinging the test area with a powerful X-ray source known as a synchrotron (Elder et al., 1947). When the electrons change direction due to the impedance of their path, energy is emitted and can be collected from an electron beam collector. In the experimentation of Zhao et al. (Zhao et al., 2017), the X-ray beam penetrates through the 450 µm powder bed into a collector approximately 300 mm away with an exposure time of 20 ns. This allowed images to be collected at 50 kHz (images collected each 20 µs) during each process to investigate the impact of the laser beam on the powder bed and heating/evaporation of the substrate. Figure 3.7 provides still frames at various instances of the heating process for each of the aforementioned laser power setting utilized in the L-PBF process.
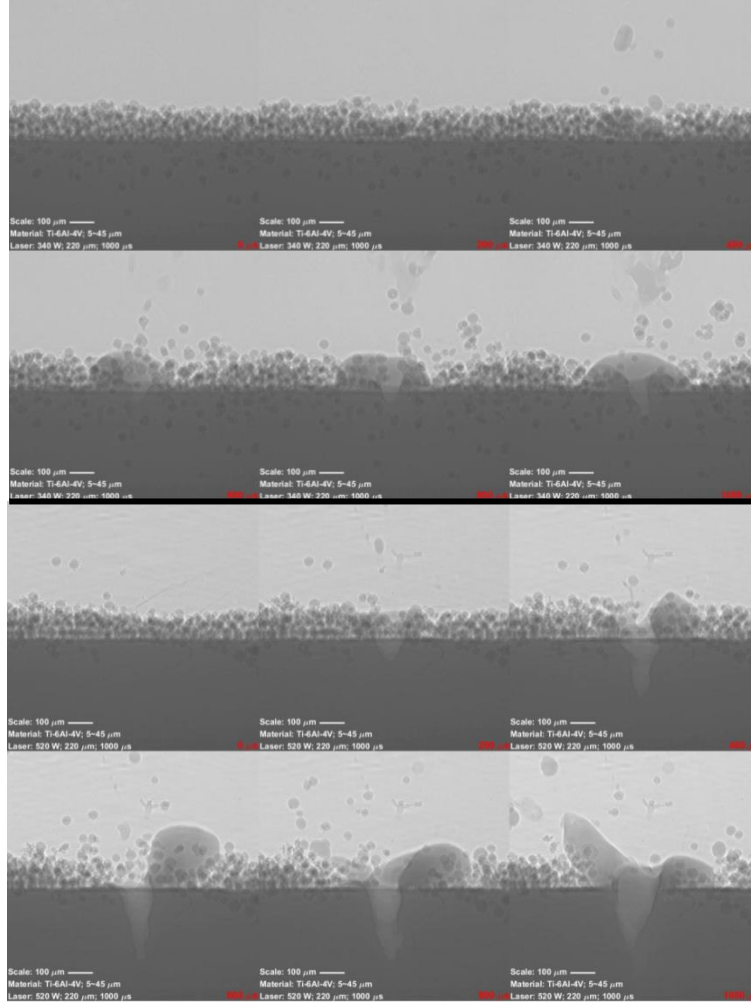
Figure 3.7: Synchrotron imagery collected from (Zhao et al., 2017) at 340 W (top) and 520 W (bottom)

Modeling of the powder bed with the DEM methodology was performed using 6000 uniformly-sized powder particles with a diameter of 30 µm, the average size of particles from the experimental study in (Zhao et al., 2017). A three-dimensional simulation space was created to allow the particles to move unimpeded within the domain, which was composed of a rectangular prismatic volume with dimensions 3.0 cm x 10.55 cm x 0.5 cm. Particles were initialized in a uniformly-spaced array with 8 particles in each of the transverse directions (x and z), and layers of particles stacked in the y-direction. Gravity in the negative y-direction was the only external force imparted on the particle besides particle-boundary interaction forces. Particle collisions were handled elastically using a spring constant of 1000 N/m, and required a time step of 1.0e-7 s to prevent excessive collision forces. Ultimately, the spring constant was selected to be high enough

to prevent particles from penetrating through each other, yet sufficiently small to prevent the need to use a calculation-prohibitive time step, which was similarly reduced in (Silbert et al., 2001). Parameters used within the simulation are provided in Table 3.1. The simulation was continued until the maximum particle velocity within the domain was less than 1e-5 m/s to obtain a powder bed at rest.

Table 3.1: Powder properties for DEM simulation

Property	Units	Solid phase
Particle Count	-	6000
Particle Diameter	μm	30 [Zhao et al., 2017]
Spring Constant	N/m	1000
Density	kg/m^3	4506
Coefficient of Restitution	-	0.95
Coefficient of Friction	-	0.10

Both the powder and substrate material were modeled as Ti-6Al-4V with material properties listed in Table 3.2.

Table 3.2: Thermal and physical properties for Ti-6Al-4V

Property	Units	Solid phase	Liquid phase
Density	kg/m^3	4506	4506
Specific heat	J/kg-K	650	831
Thermal conductivity	W/m-K	0.01327T+2.770 (Katinas et al., 2019)	0.0183T-6.66[Boivineau et al., 2006]
Liquid viscosity	kg/m-s	-	3.2e-3[Westerberg et al., 1998]
Thermal expansion coefficient	1/K	8.9e-6	
Refractive Index	-	n=3.4595+4.0065i[Johnson and Christy, 1974]	
Latent heat	J/kg	3.65e5	
Heat of Vaporization	J/kg	9.092e6[Westerberg et al., 1998]	
Solidus temperature	K	1878[Mills, 2002, Boivineau et al., 2006]	
Liquidus temperature	K	1933[Mills, 2002, Boivineau et al., 2006]	
Evaporation temperature	K	3573[Rai et al., 2007]	
Surface tension	N/m	1.65[Westerberg et al., 1998]	
Surface tension coefficient	N/m-K	-2.4e-4[Westerberg et al., 1998]	

Figure 3.8 depicts the final powder bed configuration once the particles remained static, which occurred after 0.6 s. The calculated void fraction of the powder bed was 0.379, compared to 0.375-0.391 in poured spherical beds of uniformly-sized particles (Benenati and Brosilow, 1962, Dullien, 2012); thus, the model built to simulate the Ti-6Al-4V particles is able to provide a physically relevant basis for dropped particles within a confined volume. For some powder bed placement scenarios, a scraper blade is used to compact the powder and provide additional contact between adjacent powder particles by reducing the void fraction and increasing the number of particle contacts; however, the powder bed in the experimentation in (Zhao et al., 2017) was created via pouring and using a spreader to unify the powder thickness, rather than compressing the powder layer. Thus, it was expected that the calculated void fraction is on the lower end of the range from literature.
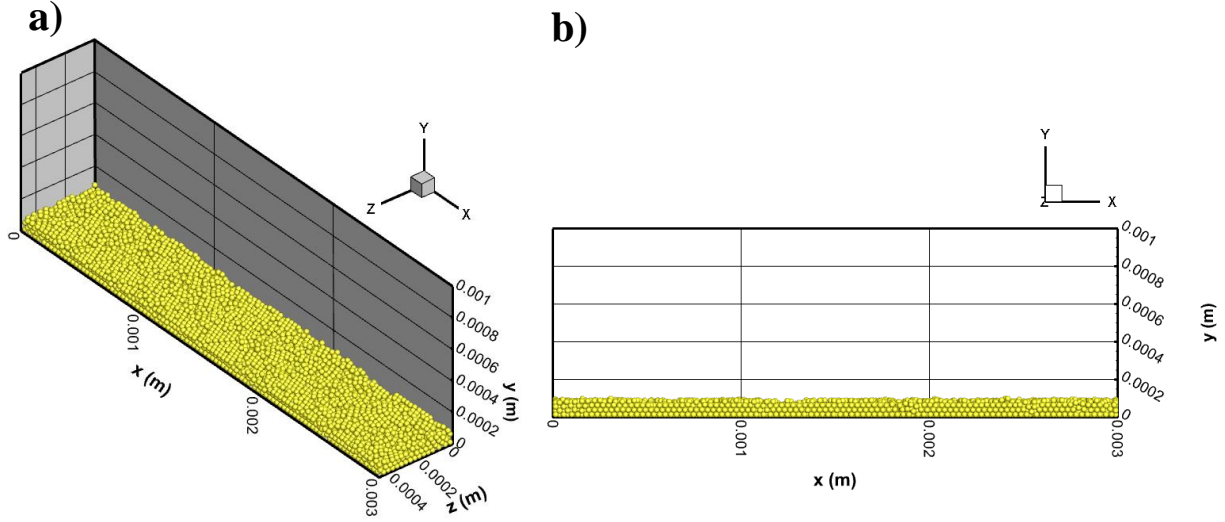
Figure 3.8: Particle bed generated for PBF process: (a) isometric view and (b) side view

The governing equations (equations (3.1) through (3.4)) are solved using a dual-mesh algorithm, in which a fine mesh moving at the laser beam velocity is used to solve fluid dynamics due to evaporation and fluid motion above the substrate surface and within the molten pool, while a coarse mesh is used to solve for heat transfer effects between the fine mesh region and the remainder of the substrate. The process was simulated using a substrate 450 μm wide, and 3.0 mm in depth to mimic the experimental domain as closely as possible. Uniform spatial discretization was used throughout both the coarse and fine mesh regions, with computational grid sizes of 50 μm and 15 μm within the coarse and fine regions, respectively. Temporal discretization was performed using an implicit second order dual-time stepping algorithm using 20 pseudo time steps per physical time step of 2.0e-7 seconds. Using the powder bed arrangement at rest from Figure 3.8, particles were placed upon the substrate surface. Since the laser beam center axis remains static throughout the simulation, the powder bed was placed to ensure the fine mesh region was covered by the powder bed, and the excess powder was located in the positive x-direction for the future capability of laser beam motion. Figure 3.9 depicts both the full domain as well as an enhanced view of the fine mesh region used for simulating the L-PBF process.
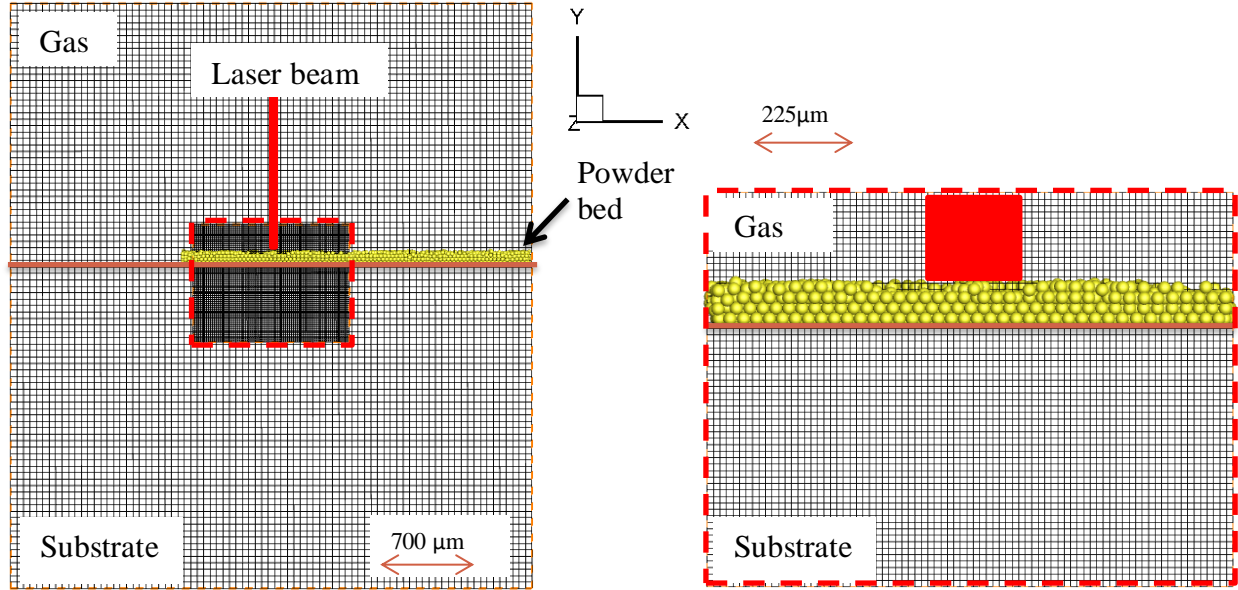
Figure 3.9: Domain used for simulation of the L-PBF process

During the initial stages of heating, particles will increase in temperature up to the solidus temperature of the powder material based on the assumptions used for the powder bed heating model. Figure 3.10 depicts the thermal evolution of particles adjacent to the laser beam center plane in 2 µs increments at a heating rate of 340 W. With a Gaussian beam, the highest laser intensity is located at the beam center axis, which would result in a higher heating rate for particles closer to the center. The particles at the surface begin to melt within the first 8 µs and start shedding mass to the substrate surface. Variation in the location of individual particles within the particle bed is observed to result in certain particles at the surface being heated at different rates.
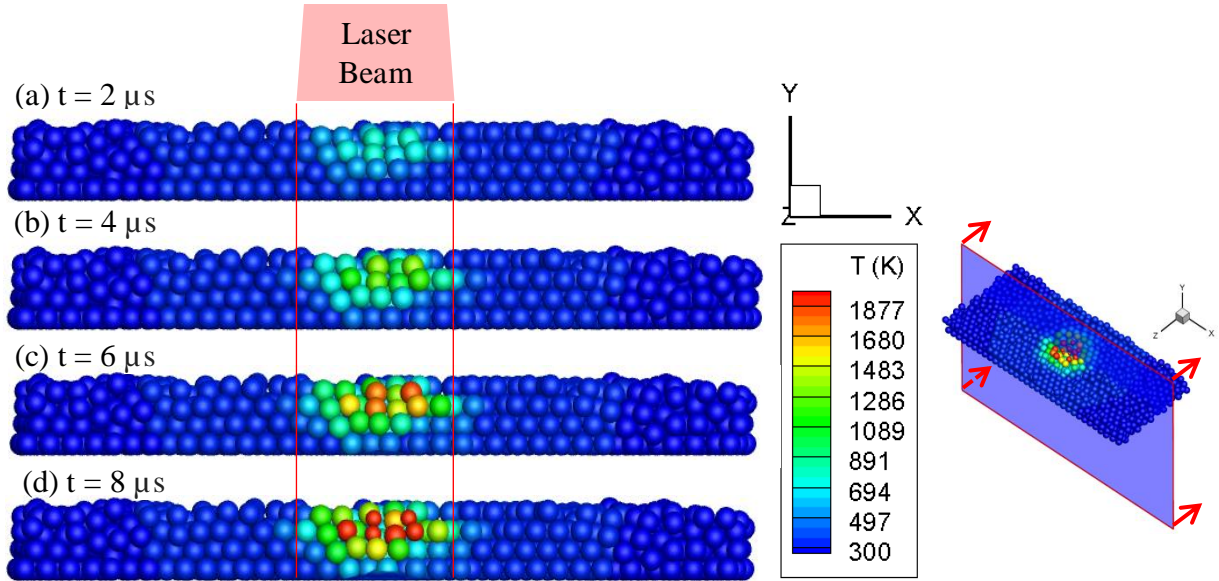
Figure 3.10: Powder bed temperature profile during 340 W heating after (a) 2 µs, (b) 4 µs, (c) 6 µs, (d) 8 µs

Upon allowing the simulation to reach the end of the heating cycle, images were generated every 20 µs showing the particle addition to the substrate surface for each of the laser power settings (520 W and 340 W). Selected frames were extracted from both the simulations and experiments to provide a comparison of the size and shape of the keyhole generated during the timeframe the laser beam is actively irradiating the powder bed and substrate. Figure 3.11 and Figure 3.12 provide a comparison between the modeled and experimental L-PBF processes every 200 µs. For the lower laser power (340 W), Figure 3.11 shows that approximately 400 µs is required to melt the powder fully prior to a keyhole forming. Initiation of the keyhole correlates well with the experimental data, with keyhole depths of 58 µm, 101 µm, and 156 µm being observed at 600 µs, 800 µs, and 1000 µs, respectively, compared to the experimentally-obtained keyhole depths of 56 µm, 53 µm, and 128 µm for the aforementioned times through the heating process. Keyhole widths measured at the free surface at 600 µs, 800 µs, and 1000 µs through the laser irradiation process were found to be 117 µm, 126 µm and 143 µm, respectively. After the L-PBF process had elapsed for 1000 µs, the molten bead was predicted to have a diameter and height of 392 µm and 156 µm, respectively, which correlates to the experimental diameter and height of 497 µm and 175 µm, respectively. In the case of 520 W laser power, any powder directly within the laser irradiation region had been added to the substrate by 200 µs, at which time, the start of a keyhole had begun to penetrate through the substrate surface. Figure 3.12 shows that the model

predicts a 35 μm keyhole penetrated the substrate surface at approximately 200 μs, after which the keyhole continued to expand to 146 μm, 250 μm, 338 μm, and finally 419 μm in subsequent 200 μs periods. The experimental data shows the keyhole depth as 100 μm, 238 μm, 288 μm, 290 μm, and 410 μm at the same periods in time.
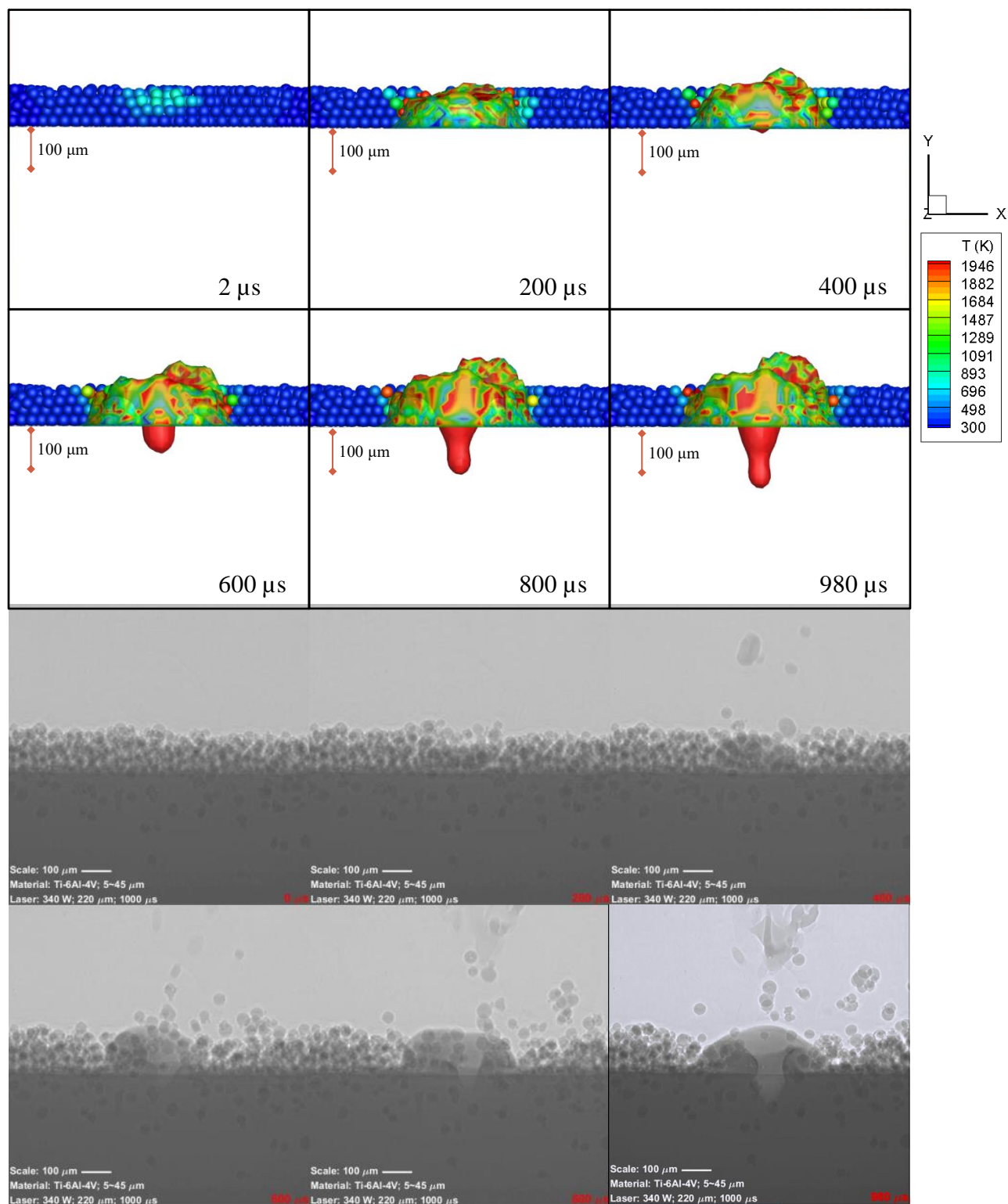
Figure 3.11: Comparison of model prediction and experimental results at 340 W
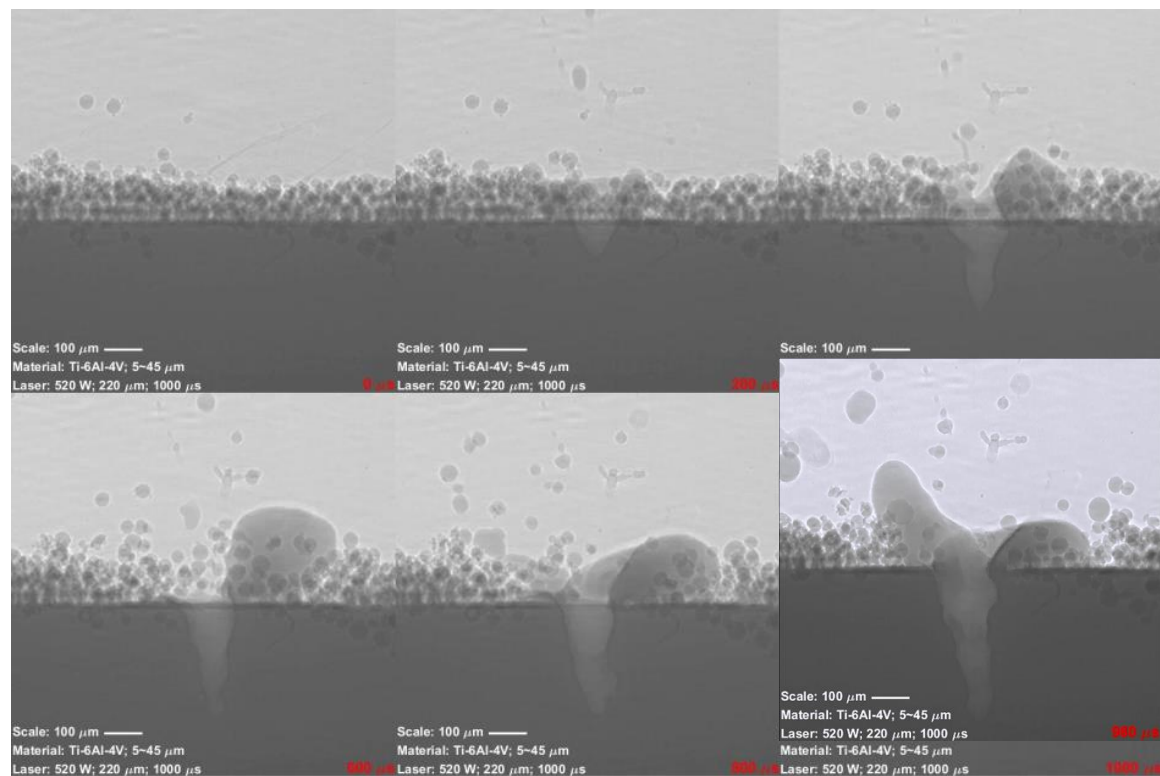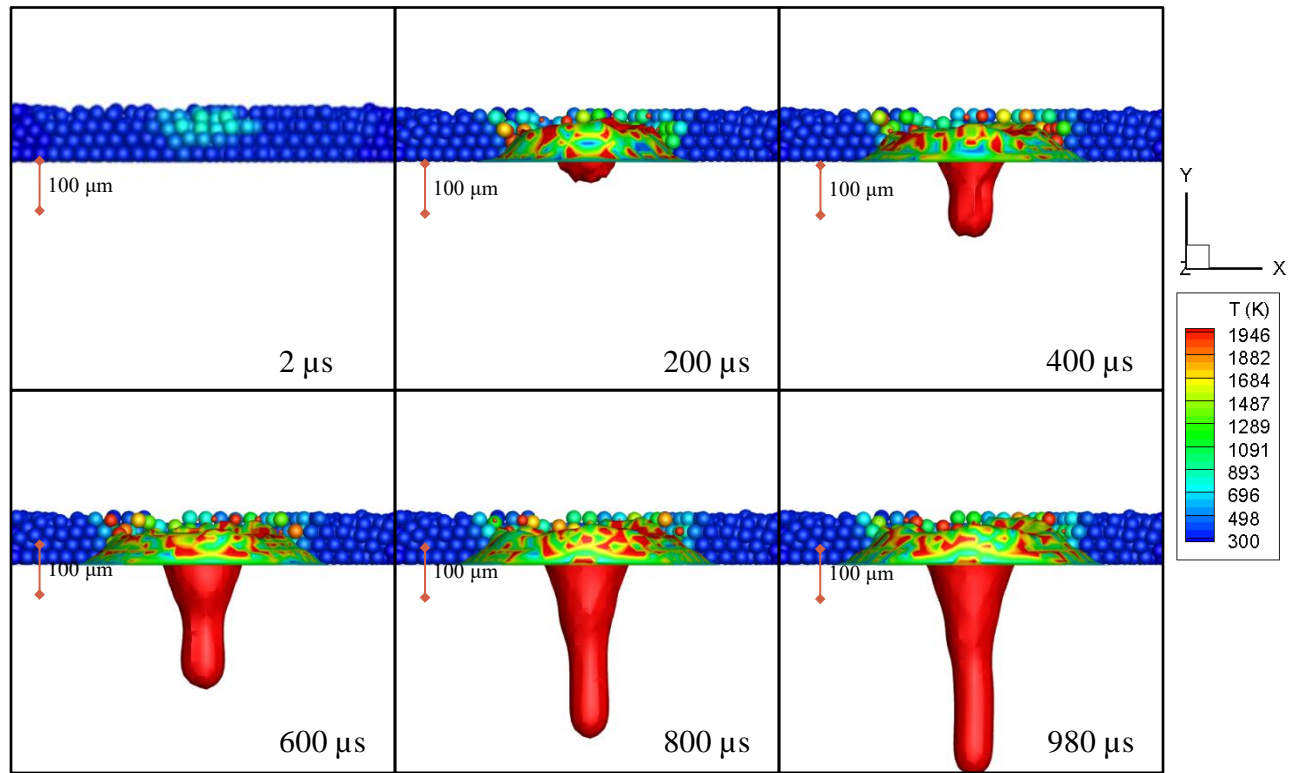
Figure 3.12: Comparison of model prediction and experimental results at 520 W

Figure 3.13 depicts a temperature contour plot at the centerplane of the fine mesh region extracted at the end of the 340 W irradiation cycle. A black line has been drawn to denote the free surface and clearly show the boundary between gas and liquid/solid phases. Velocity vectors have been included in the contour plot, with gas velocities being scaled by a factor of 0.001 to coincide closer to the range of velocities observed in the liquid region. A maximum gas velocity of 421 m/s was found at the laser beam center axis and the height of the molten pool, while the maximum liquid velocity was observed at the bottom of the keyhole and adjacent to the liquid-gas interface with a magnitude of 0.43 m/s. To assess the influence of the gas phase on the movement of particles within the particle bed, gas velocity within the region adjacent to the substrate was reviewed and was found to have a magnitude of 0.02 m/s, which is insufficient to generate large drag forces on the particles to explain the driving forces observed within the experimental results.
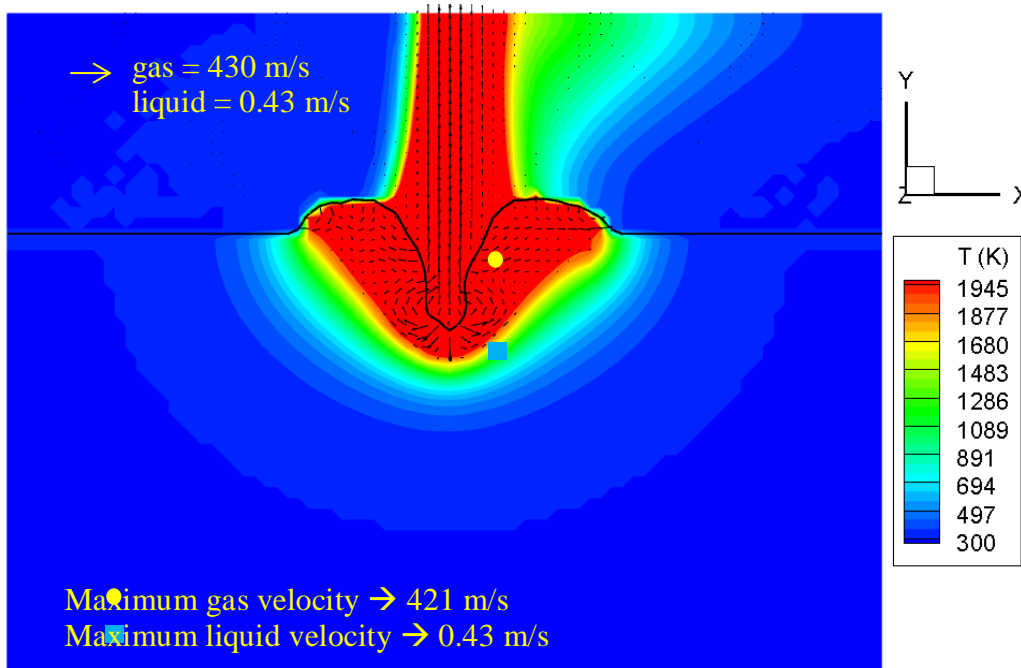
Figure 3.13: Temperature and velocity field at laser center plane (340 W, 1000 μs)

When the laser power is increased to 520 W, the maximum gas and liquid velocities increase to 634 m/s and 0.84 m/s, respectively, as shown in Figure 3.14 at the end of the heating cycle. Similar to the case of 340 W power, the maximum liquid velocity is found at the bottom

of the keyhole; however, the location of the maximum gas velocity has retreated inside the keyhole and is located at the height of the original substrate.
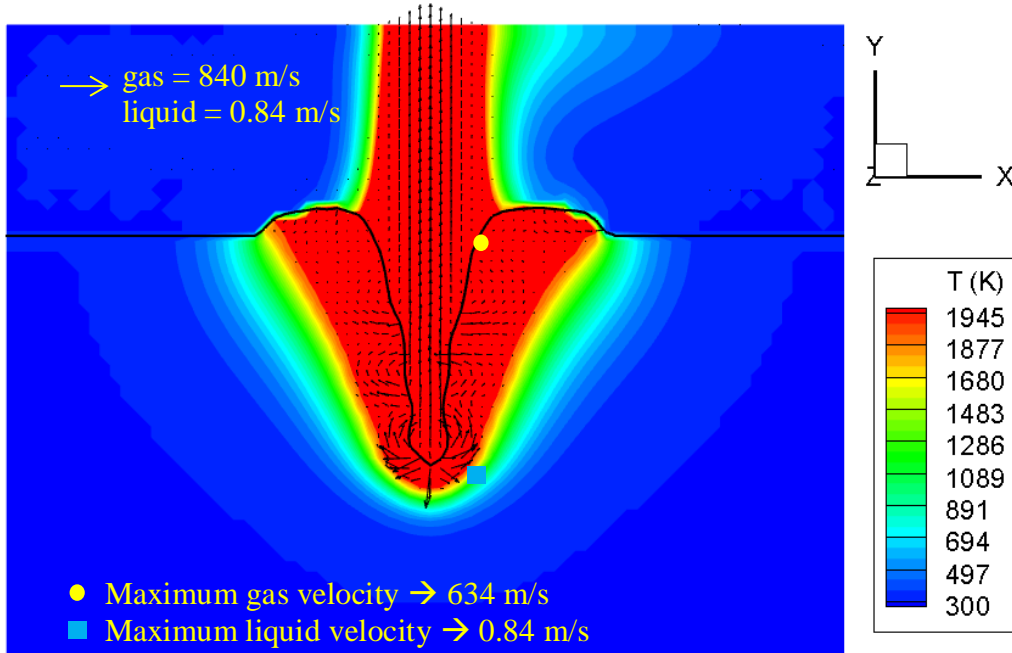
Figure 3.14: Temperature and velocity field at laser center plane (520 W, 1000 μs)

Particle heating occurs very rapidly, to the extent that conduction alone is unable to transfer heat away from the particle bed quickly enough for the laser irradiation, and hence why conduction with the powder bed is considered negligible and is not included within the powder bed model. For example, the effective thermal conductivity of the powder bed is essentially that of air due to the small number of spherical contacts within the powder bed allowing heat to transfer (Khairallah et al., 2016). The maximum rate of conduction through the powder bed is limited by the temperature differential and effective thermal conductivity of the powder bed. For single-layer powder beds, the melting of particles will bind to the substrate and increase the area for conductive heat transfer to occur, but when multiple-layer powder beds are considered, there is not sufficient contact between particles to enable conductive heat transfer into the substrate. Instead, particles will melt rapidly and wet adjacent particles, which continue to increase conductive heat transfer through the particle bed. In the event that laser power is insufficient to fully melt the particles of the modeled powder bed, particles of the non-zero radius will remain within the laser irradiation region at the surface of the substrate, since they are the last particles to receive laser energy. Thus,

the model will show mass added to the substrate surface even though particles will still be observed resting at the substrate surface.

The most significant deviation between the model prediction and the experimental result is with the height of the molten bead, as observed in the 520 W laser power case. There are a few explanations for this: (1) higher laser intensity increases turbulence, and therefore, randomness in the process, and (2) particles were confined to a 450 μm wide region, increasing the chance for particle-particle and particle-substrate collision when compared to an open-system. For example, after powder had adhered to the substrate surface in 520 W experiments (Figure 3.12), the molten bead rapidly shifted to one side of the keyhole, leaving essentially no mass on the opposite side of the molten bead. Since the goal of this modeling effort is to gain an average glimpse into the process, rather than create an identical match to a few specific instances of possible L-PBF outcomes, the molten bead height and keyhole depth should be comparable over the entire extent of the process, which is well-correlated in Figure 3.11 and Figure 3.12. To mimic the observations of the experimental data, the three-dimensional arrangement of the powder along with particle trajectories would be necessary to provide the correct attenuation of the laser beam and/or add to the molten pool, depending on the location of a given particle. Instead, the focus of the modeling effort is to provide an averaged scenario in which particles are heated and added to the substrate surface so that longer-term scenarios can be performed, including multi-track and multi-layer L-PBF processes.

In extreme cases of L-PBF (as were modeled in this study), such as with a stationary laser beam, a keyhole welding mode was observed, which can lead to sub-surface porosity and ultimately a weaker and more brittle product (King et al., 2014). In typical powder bed fusion processes, the laser heat source scans along the powder bed surface, thus preventing excessive surface evaporation: though depending on the process parameters, it remains possible that this potentially undesirable condition exists. The results from the model provide substantiation that a keyhole can be predicted in the event that excessive laser power is utilized for a given set of process parameters. Having the ability to model the deposition phenomenon alongside an evaporation model allows for determining laser scanning parameters to minimize negative effects due to modification of the substrate layer. In (King et al., 2014), a heuristic for keyhole formation was developed as a function of the laser processing parameters and material properties, which enabled the formation of a non-dimensional parameter to segregate conduction mode and keyhole mode

124

heating scenarios and can be used as an initial estimate of laser power required to achieve a favorable manufactured component from a given L-PBF process.

Denudation of the powder bed has been neglected as part of this analysis, primarily due to the amount of uncertainty included by allowing particle motion to influence the process. Particle drag force due to the induced gas flow from the laser plume was found to be insignificant from the velocity fields acquired from the model and does not explain particles being injected into the gas plume. From both Figure 3.13 and Figure 3.14, the predominant velocity component is in the positive y-direction, ejecting evaporated material in a direction normal to the original substrate surface. If a particle is found to cross the path of the evaporation plume, the high velocity gas (>420 m/s from the two scenarios simulated in this study) is sufficient to accelerate particles rapidly. In the experimental data, particles were observed to accelerate from near-rest to as fast as 5 m/s within the evaporation plume region within a 20 μs timeframe. Including denudation of the powder bed within the model would require determination of the predominant location of where a given particle is being heated, to apply the correct directionality of the evaporation force (Matthews et al., 2016).

In conclusion, a method to simulate and predict the powder bed fusion process was developed and shown to provide a reasonable representation of the deposition and evaporation processes that are observed in high intensity laser irradiation. Keyhole penetration depth after a 1000 μs heating cycle with laser power of 340 W and 520 W was predicted to be 156 μm and 419 μm compared to 128 μm and 410 μm, respectively. The molten bead width and height for the 340W laser power simulation was found to be 392 μm and 156 μm, respectively, compared to 497 μm and 175 μm, respectively, when observed experimentally. For the 520W laser power simulation, the molten bead measured 484 μm in width with a height of 87 μm, compared to experimental width and height of 515 μm and 115 μm, respectively. Profiles for the keyhole shape and molten bead size predictions resembled corresponding experimental data, with most deviation existing due to phenomena that can be explained by process randomness. Finally, although particles were held motionless during the process, the model showed that gas velocity adjacent to the substrate surface was insufficient by itself to propel particles directly into the path of the evaporation plume.

3.2.2   Single-Track Deposition of Ti-6Al-4V Powder Bed Fusion

The validation scenario in Section 3.2.1 made basic assumptions to decrease model computational effort. In an effort to address shortcomings of the aforementioned model, as well as other models in the literature, the model described in this section addresses aspects of powder bed placement, irradiation of the particle bed, and molten pool formation in a computationally efficient manner (reducing computational effort by up to 95%). This case study includes modeling the size distribution of particles as opposed to a uniform particle size distribution which could affect powder placement and localized melting of the powder bed. In addition, particle motion associated with absorption of powder by the molten pool as well as denudation effects associated with local gas dynamics has been included. To balance model accuracy and computational effort, a volumetric particle heating method using a Beer-Lambert attenuation law (Katinas and Shin, 2020) allows simulation of heating of a combination of thick and/or sparse powder beds, which may simultaneously exist as particles melt and adhere to the workpiece, while a ray-tracing model with multiple reflections is used to account for energy absorption by the substrate once the powder bed has been consolidated.

To begin the simulation, particles with a size distribution from experimentation were arranged in a rectangular prismatic arrangement above the substrate surface and allowed to fall onto the substrate surface via gravitational acceleration until the particles come to rest upon the surface of the substrate. A rectangular prismatic domain with dimensions of 1.8 mm x 15.5 mm x 0.6 mm was used to limit particle motion beyond a small area of interest. Once all particles within the domain achieved a velocity less than 1.0e-6 m/s, the simulation was stopped and the particle positions were recorded. To mimic the spreading method used in experiments, a roller with a diameter of 2.0 mm was traversed over the powder bed along the x-direction at a height of 100 microns and a roller velocity of 25 mm/s to spread and pack the powder bed. The rectangular boundary from the initial placement operation was increased along the x-direction from 1.8 mm to 2.3 mm to accommodate particles that have been displaced due to spreading. Spreading was performed three times, as had been completed during the experimental setup.

Simulations of both initial powder placement and powder spreading operations used the first-order forward Euler time advancement with a time step of 1.0e-7 seconds. Material properties for the DEM simulations are provided in Table 3.3. To prevent the need of using a smaller time step than the one chosen in this study, the material spring constant was reduced as it does not play

126

a significant role in the final location of particles, provided that particles do not penetrate into each other during the simulation (Silbert et al., 2001).

Table 3.3: Powder properties for DEM simulation for Single-Track Deposition

Property	Units	Solid phase
Particle Count	-	6000
Particle Diameter	µm	Experimental
Spring Constant	N/m	300
Density	kg/m^3	4506
Coefficient of Restitution	-	0.65
Coefficient of Friction	-	0.30

Table 3.4 provides the thermal and physical properties used for the single-track simulation of the L-PBF process.

Table 3.4: Thermal and physical properties for Ti-6Al-4V used in Single-Track Deposition (Katinas and Shin, 2020)

Property	Units	Solid phase	Liquid phase
Density	kg/m^3	4506	4506
Specific heat	J/kg-K	560	560
Thermal conductivity	W/m-K	0.01327T+2.770	0.0183T-6.66
Liquid viscosity	kg/m-s	-	3.2e-3
Thermal expansion coefficient	1/K	8.9e-6	
Absorptivity	-	0.34	
Emissivity	-	0.25	
Latent heat	J/kg	3.65e5	
Solidus temperature	K	1878	
Liquidus temperature	K	1933	
Evaporation temperature	K	3046	
Surface tension	N/m	1.65	
Surface tension coefficient	N/m-K	-2.4e-4	

To accommodate particle absorption into the molten pool, particles that become partially engulfed by the formed molten pool are subject to a capillary force that draws a given particle toward the laser beam radius, as described in equation (3.23).

$$F_{cap} = C(\vec{x}_{part} - \vec{x}_{laser})m_{part}\frac{\Delta\varphi}{\|\Delta\varphi\|} \qquad (3.23)$$

where F_{cap} is the capillary force applied, m_{part} is the mass of a particle to which the force is applied, φ is the levelset field value at a given particle centroid ($\vec{x}_{part}$), $\vec{x}_{laser}$ is the laser beam center axis location which coincides with the original surface of the substrate, and C is the force constant to denote the acceleration of the particle once it has been trapped within the molten pool. The force constant has been selected to be 1e4 to prevent the excessive acceleration of particles during simulation, which would otherwise require a smaller time step when numerically solving the governing equations. Equation (3.23) only applies to particles which touch the free surface of the substrate, as determined by the levelset zero isocontour such that the surface temperature at the collision site is greater than the solidus temperature of the material.

In addition, laser energy addition is coupled between the two models through the following mechanisms: (1) energy addition to the powder bed causing particle melting, and (2) direct heating of the substrate when unencumbered by powder bed particles. In the first energy addition mechanism, a Beer-Lambert attenuation law is applied as in Ref. (King et al., 2015b) throughout the depth of the powder bed thickness to determine the amount of laser energy that is applied to each of the particles within the powder bed, as well as the amount of energy which passes through the powder bed (in the event of a sparse particle arrangement). The remaining energy is reflected by the powder bed and is excluded from the analysis. As the particles melt, the powder bed becomes more and more sparse, leading to the second heating mechanism of direct laser heating, and is governed by the local absorptivity of the material and the angle of incidence of a given ray to the surface of the molten bead.

A dual-mesh algorithm (or Arbitrary Eulerian-Lagrangian algorithm) (Ahn and Kallinderis, 2006) was implemented to reduce computational effort as compared to obtaining a solution to all governing equations throughout the entire domain. Two distinct meshes are generated, one being a fine mesh in which equations (3.1) through (3.4) are solved with all of the source terms of the energy, mass, energy, levelset equations due to laser heating, powder addition, and evaporation effects, while the other mesh is a coarsely discretized domain where only conduction-based energy transfer is considered. A domain consisting of a 2.0 mm x 2.0 mm x 1.0 mm thick substrate with a 1.0 mm gas layer above the substrate was modeled. The fine mesh (measuring 1.0 mm x 0.75

mm x 0.75 mm, with the largest dimension along the laser scanning direction) was discretized using 15 µm regular hexahedral control volumes while the course mesh was discretized with 60 µm regular hexahedral control volumes, yielding 147,456 and 110,592 control volumes in the fine mesh and coarse mesh regions, respectively.

Temporal discretization of the domain is performed via a dual time-stepping algorithm (Li and Merkle, 2006) in which the physical time step is split into multiple pseudo time steps to stabilize the numerical solution for the governing equations prior to advancing to the next physical time step. For the L-PBF simulation, a physical time step of 5.0e-7 seconds with 10 pseudo time steps per physical time step was utilized. The process was simulated for a physical duration of 0.01 seconds to allow for the trailing edge of the deposition to reach quasi-steady conditions and corresponds to a scanning distance of 0.846 mm. Once the simulation was completed, results were post-processed to obtain information about the track geometry which had been added to the substrate surface.

Experimental

Spherical powder Ti-6Al-4V was obtained from Puris® and was measured with optical microscopy (Nikon Eclipse LV150) to verify the shape and size distribution of the as-received powder. The composition of Ti-6Al-4V Grade 5 is shown in Table 3.5. Figure 3.15 provides an image at 10x magnification of the powder used for all powder-bed experiments discussed herein. The powder is nearly spherical with few satellite particles that can hinder the spreadability of the powder to form a powder bed with uniform thickness.

Table 3.5: Chemical Composition of Ti-6Al-4V

Element	Al	V	Fe	C	O	N	Nb	Ti
(% wt)	6.1	4.0	0.1	0.02	0.03	0.01	0.01	Bal
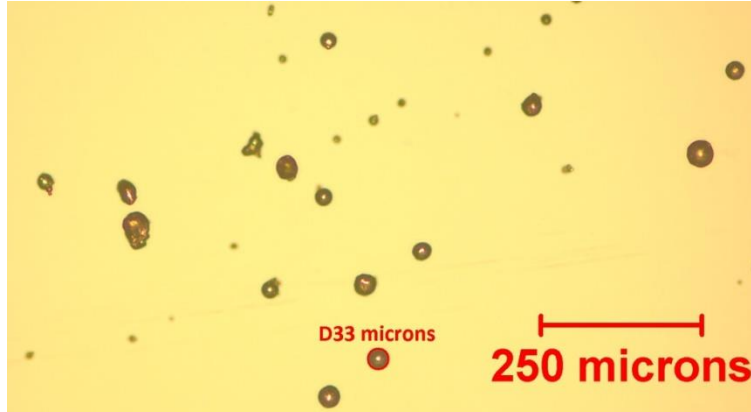
Figure 3.15: Optical micrograph of powder particles used in experimentation

Seventy five images of the powder were obtained and post-processed in Matlab to produce a histogram of the powder size distribution, which is shown in Figure 3.16. A total of 3875 particles were detected during the analysis, with an average particle size of 18.8 microns and ranged from 9.6 to 64.0 microns in diameter.
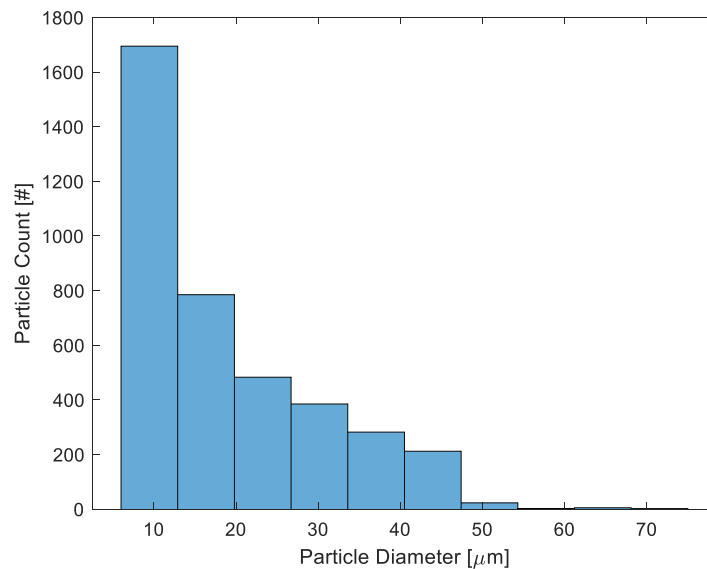
Figure 3.16: Histogram of powder size for as-received Ti-6Al-4V powder

A 2"x1"x0.5" bar of Ti-6Al-4V (grade 5) was used as the substrate which was prepared by face milling the bar to remove manufacturing marks and then cleaned with acetone and allowed to dry completely prior to use. The substrate was further prepared by milling a 100 μm deep slot

130

with a width of 0.5 inches to provide a channel for powder to accumulate to the exact height of 100 μm during powder spreading. The aforementioned Ti-6Al-4V powder was poured into the slot and was spread using a manual scraping mechanism to evenly distribute the particles. Since Ti-6Al-4V is highly susceptible to oxidation at elevated temperatures (as would be observed during L-PBF) (Casadebaigt et al., 2020), the laser powder bed fusion experiments were performed within an inert argon environment of the custom-designed laser powder bed fusion system. A schematic of the experimental setup is provided in Figure 3.19.

The laser irradiation source is a 1000 W fiber laser from IPG (IPG-1000), and focusing optics provided a beam diameter of 240 microns with a Gaussian irradiation profile at the focal plane. The maximum traverse speed of each axis is 84.6 mm/s, which was chosen as the scanning speed for all experiments, while commercial L-PBF processes are typically carried out at high speed with a smaller beam diameter. However, with the significantly larger beam diameter, despite lower scanning speed, the overall throughput is not greatly compromised since the beam can cover a large area. The parameters for the initial experiments were selected based on the work of (Karayagiz et al., 2019). Conditions from (Karayagiz et al., 2019) indicated a beam diameter of 70 microns with a laser power of 50 W at a scanning speed of 80 mm/s scanning over a 30 micron thick powder bed would provide favorable results. With a beam diameter of 240 microns, the line energy (laser power/beam diameter) would necessitate a beam power of 170 W.
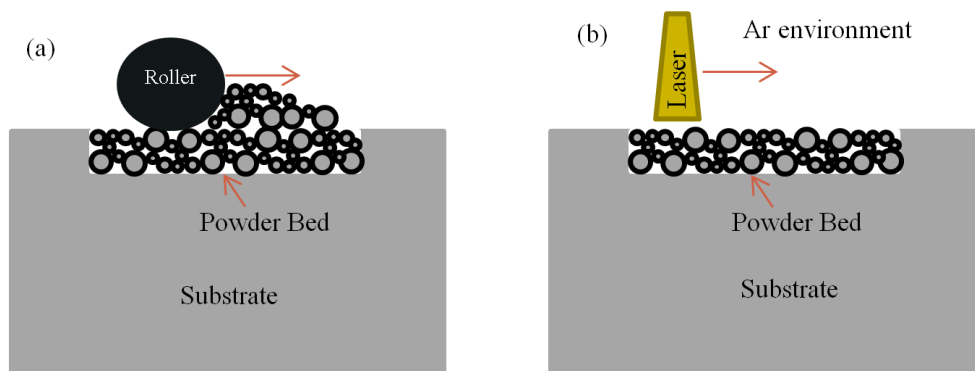
Figure 3.17: Schematic for L-PBF process (a) powder placed upon substrate surface being spread via roller and (b) laser scanning of the powder bed in an inert environment

A series of tests were performed to understand which laser power provided the highest continuous track height without causing excessive recoil pressure leading to keyhole formation and/or powder evaporation. Each scan lasted for a distance of 19 mm to ensure that quasi-steady conditions were obtained. Parameters for the parametric study are provided in Table 3.6. After single-track experiments were completed, the track surface and remaining powder were inspected using an optical profiler (Bruker ContourGT). An average track profile was obtained for each of the five tracks, of which the middle three laser power settings were simulated to investigate the effects of varying testing conditions on the L-PBF process.

Table 3.6: Experimental conditions for parametric study

Trial #	Laser Power (W)	Scan Speed (mm/s)
1	149.8	84.6
2	173.0	84.6
3	201.3	84.6
4	230.0	84.6
5	258.5	84.6

Results

DEM model results

Figure 3.18 shows a diagram of the powder placement process and the resulting powder bed which is used to simulate the remainder of the process. The initial arrangement of the particles is a structured rectangular prismatic configuration of particles as shown in Figure 3.18(a). With the particles being subject to gravitational acceleration, particles fall upon the substrate surface, but may not provide a powder bed with uniform height (Figure 3.18(b)). Hence, mechanical spreading operations are performed to ensure that a uniform powder bed thickness can be generated. Three powder spreading operations were performed, as shown in Figure 3.18(c)-(e), with each subsequent spreading pass causing the roughness of the initial powder bed to decrease. The

powder bed height after the first, second, and third spreading passes was found to be 129 μm, 116 μm, and 107 μm, respectively, as shown in Figure 3.19. Subsequent spreading passes did not reduce the powder bed height beyond 107 μm, hence the third pass was used as the basis for the powder bed for the L-PBF simulation. In comparison, the powder bed height obtained from the optical profile images was approximately 101 μm, with the DEM model overpredicting by roughly 6 percent.
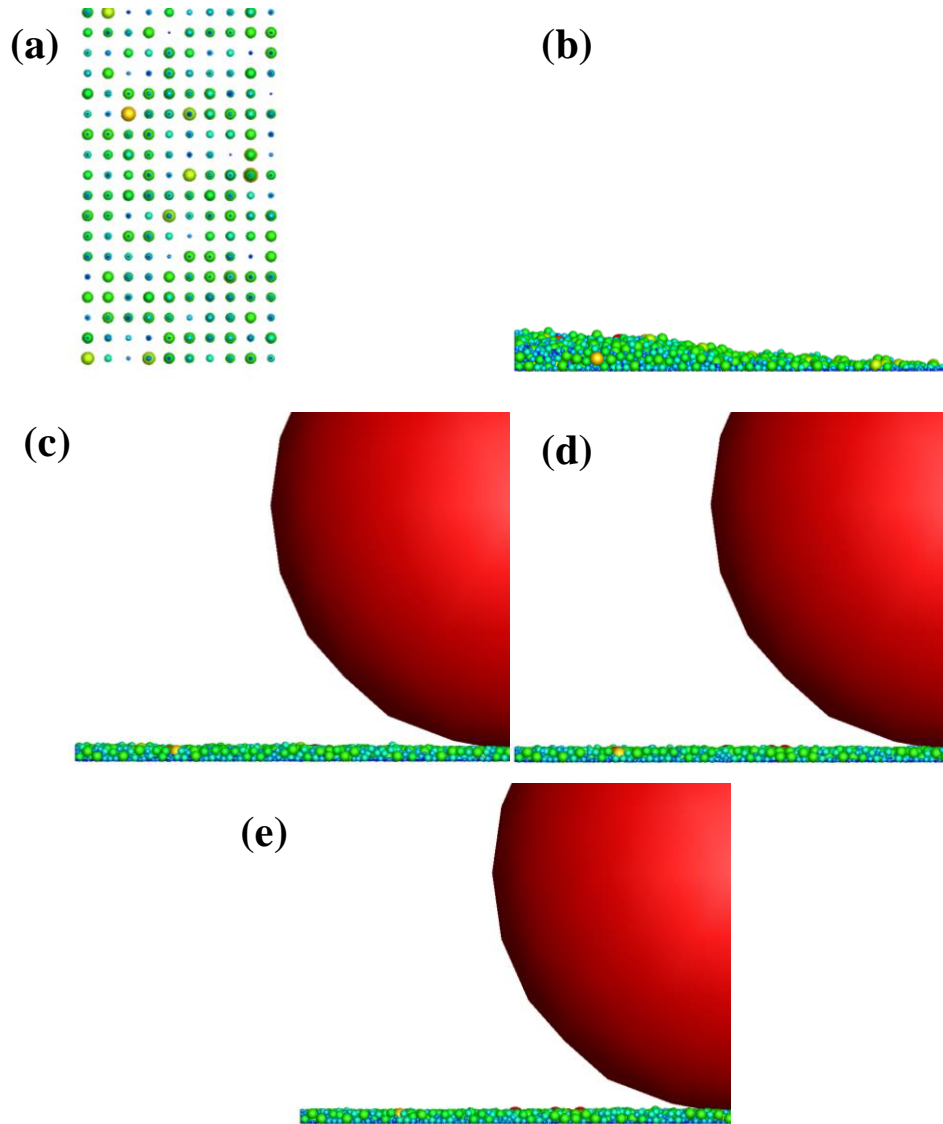
Figure 3.18: Powder placement process: (a) initial particle arrangement, (b) powder bed once particles reached zero velocity, (c) powder bed after 1st pass of spreading process, (d) powder bed after 2nd pass of spreading process, and (e) powder bed after 3rd pass of spreading process (particles colored by size)

1st pass – 129 microns

2nd pass – 116 microns

3rd pass – 107 microns
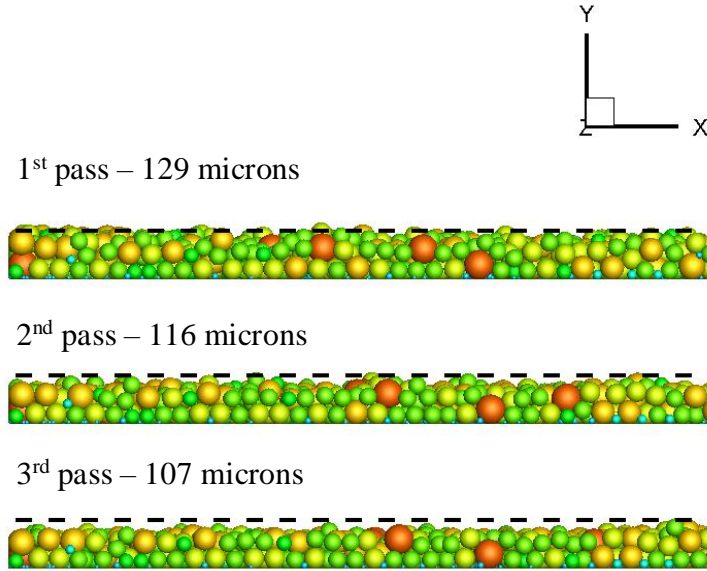
Figure 3.19: Powder bed thickness after: (top) 1st pass, (middle) 2nd pass, (bottom) 3rd pass {dashed line denotes average powder bed height after the first pass}

L-PBF Model/Experimental Validation

Figure 3.20 shows a depiction of the experimentally obtained surface observed via optical profiling with the remaining powder bed intact. The track height is based on the contour color with the darkest blue denoting the initial substrate height and the maximum height being shown in red. The powder bed height for each of the subfigures is shown to be roughly 100 microns, which was expected since the milled slot in the substrate was 100 microns deep and an excess of powder was used to reduce voids in the powder spreading process.

When comparing the track geometry, as the laser power is increased, the track height increases commensurately with the laser power setting, though the highest laser power setting (258.5W) yields a track height that is less than the previous setting (230.0W). For the 258.5 W laser power case, the denudation appears to be wider than in any of the lower laser power settings, leading to less powder near the molten pool region. Table 3.7 shows the tabulated track width and height for each experimentally-obtained track in Figure 3.20, along with the denudation region width based on the optical profile data based on 11 cross-sectional measurements. Both the track width and denudation regions are shown to be increasing as the laser power is increased; however, the increase in denudation width outpaces the track width as evidenced by the width ratios calculated in the last column of Table 3.7.
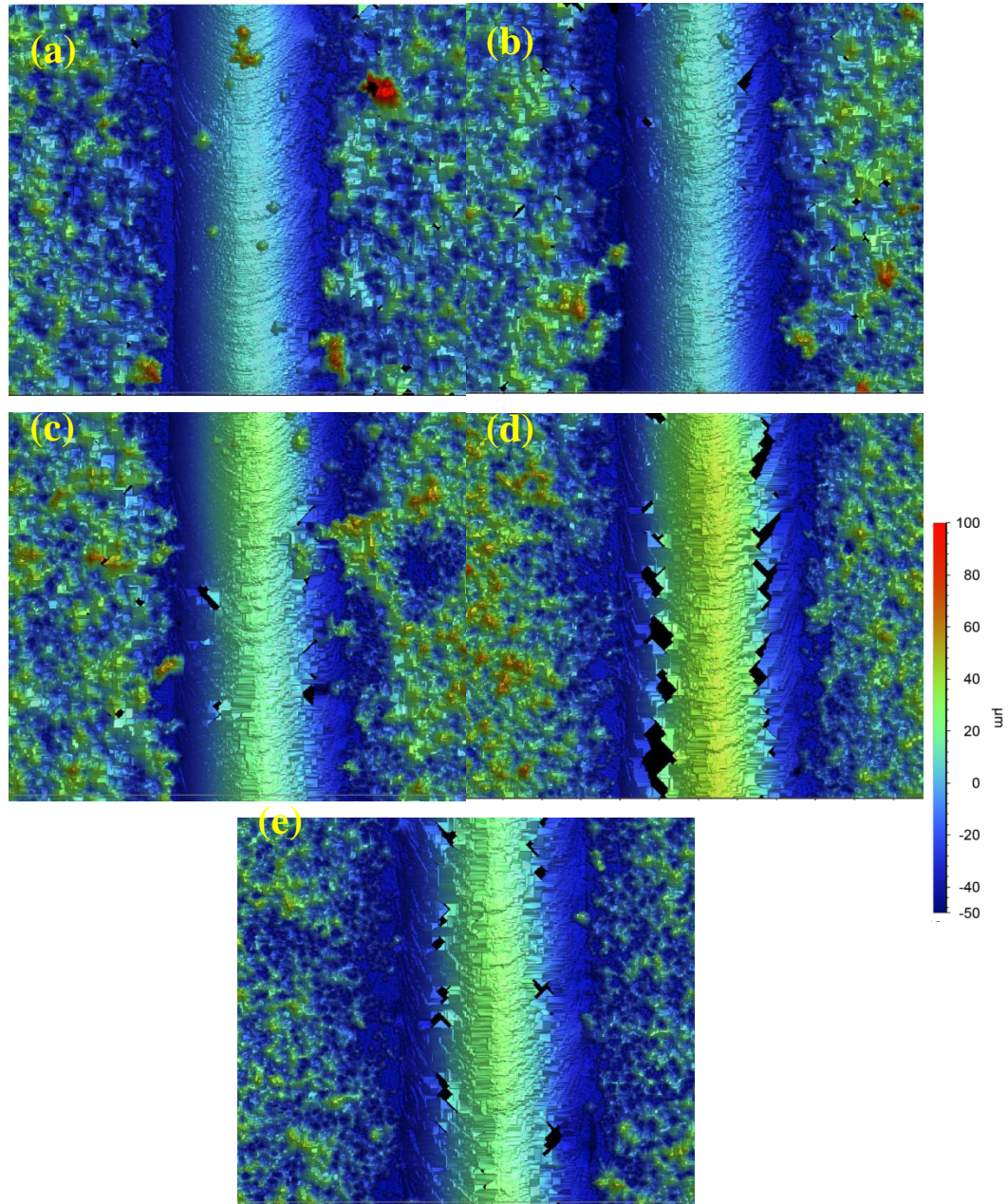
Figure 3.20: Surface profile of an L-PBF single track at (a) 149.8W, (b) 173.0 W, (c) 201.3 W, (d) 230.0 W, and (e) 258.5 W

Table 3.7: Track geometry extracted for each single track experiment (reported with uncertainty equivalent to one standard deviation)

Laser Power (W)	Track Width (μm)	Track Height (μm)	Denudation Width (μm)	Denudation/Track Width (-)
149.8	367±12	44±2.6	424±19	1.16
173.0	390±8.5	52±3.8	447±32	1.15
201.3	409±38	62±4.8	452±45	1.11
230.0	456±7.8	78±1.7	551±20	1.21
258.5	448±21	64±2.5	536±28	1.20

Simulated results for the track profiles of three middle laser power settings were compared against their analogous experimental profiles, and are shown in Figure 3.21. Cross-sectional profiles at 11 different locations were collected from both the experimental and model data, and were analyzed to provide an average profile and a standard deviation. Track profiles for each laser power show a parabolic shape in both the experimental and simulated data. The track width obtained from the simulation of the 173.0 W, 201.3 W, and 230.0 W laser power settings were found to be 433 μm, 449 μm, and 501 μm, resulting in an error of 11%, 9.8%, and 9.9%, respectively. Similarly, track height obtained from the simulation of the 173.0 W, 201.3 W, and 230.0 W laser power settings were found to be 64.8 μm, 66.5 μm, and 66.1 μm, resulting in an error of 24.6%, 7.3%, and -15.3%, respectively.

Figure 3.22 shows the resulting deposition after the simulation had completed with the powder bed removed to show the underlying temperature field (Figure 3.22(a)) as well as the remaining powder (Figure 3.22(b)). At each of the laser power settings, there was sufficient energy to generate a keyhole which is evidenced by the elongated pocket on the +x-direction of the molten pool in each of the subfigures. The analysis showed that the average temperature within the keyhole of the 201.3 W simulation was 3626 K, which is above the boiling temperature of Ti-6Al-4V as shown in Table 3.4. Quasi-steady conditions with respect to the track geometry were met after the 0.41 mm of deposited powder accumulated behind the keyhole, after which the track geometry was insensitive to the scanning direction.
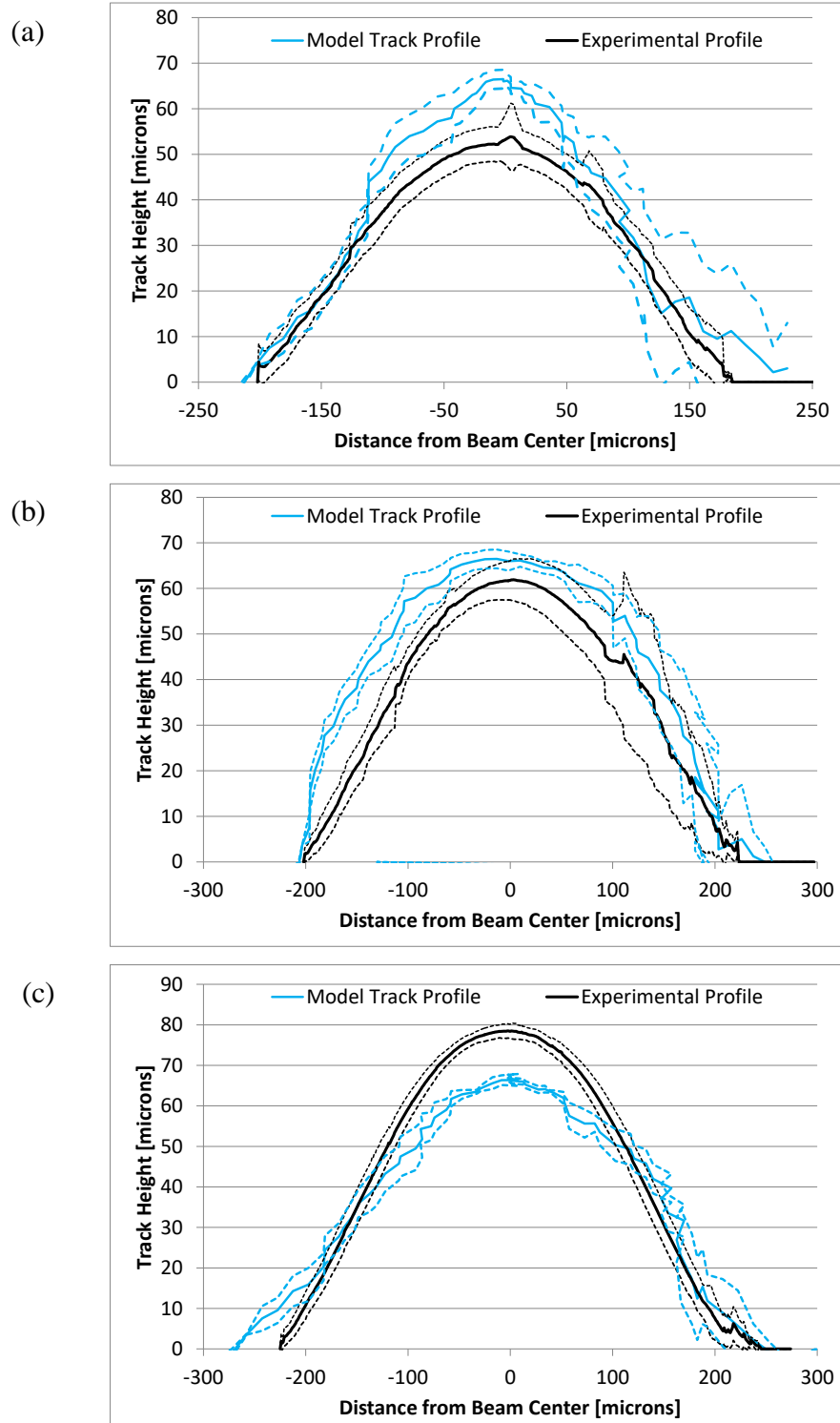
Figure 3.21: Comparison of the track cross-sectional geometry at (a) 173.0 W, (b) 201.3 W, and (c) 230.0 W
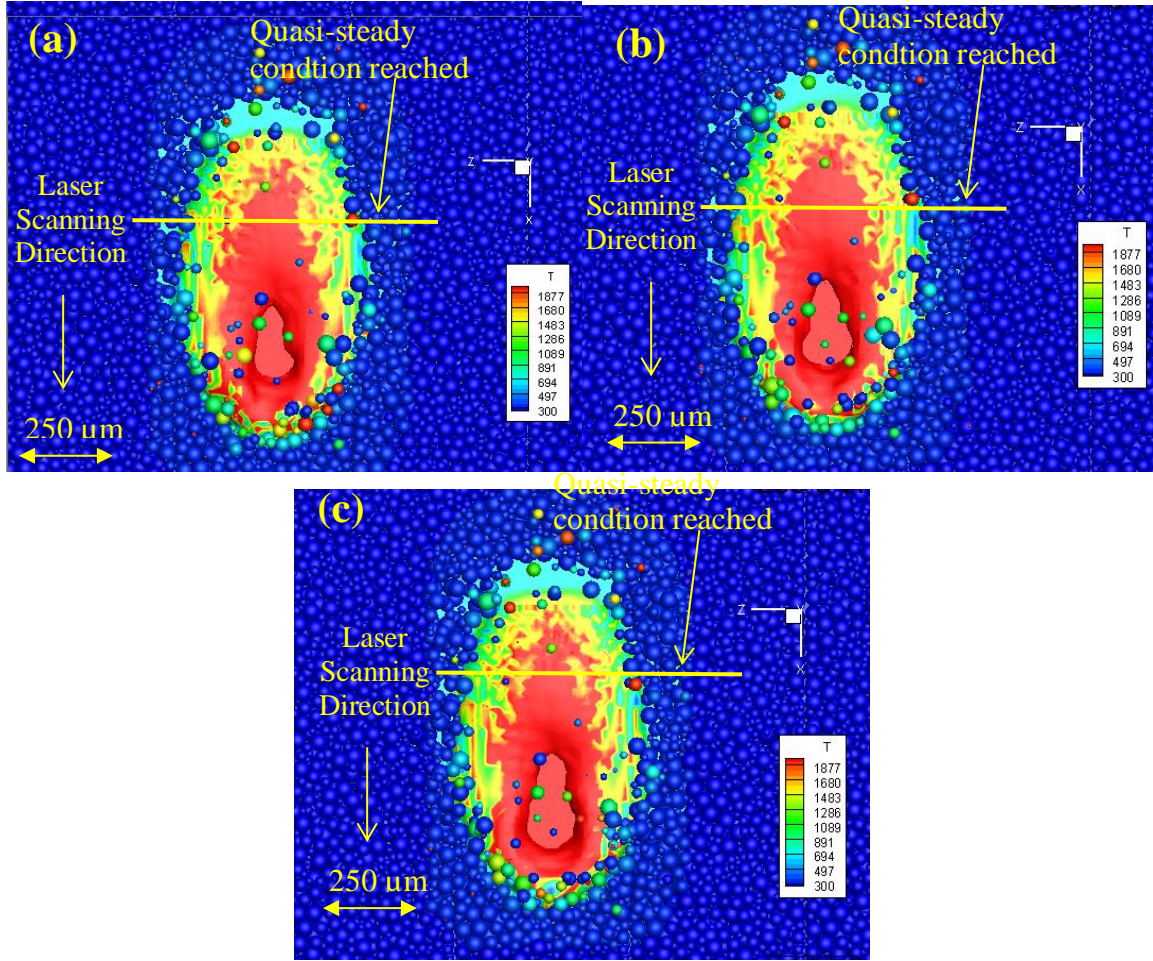
Figure 3.22: Simulation results showing the resulting powder bed upon process completion at (a) 173.0 W, (b) 201.3. W, and (c) 230.0 W (Temperatures displayed in Kelvin)

Figure 3.23 shows both the side and front views of the deposition at the end of the simulation. The molten pool height is temporarily higher than the height observed within the irradiation region, and can be explained by the intake of particles due to absorption of particles in direct contact with the molten pool on the leading side of the molten pool, while molten pool spreading will occur due to evaporation, as evidenced by keyhole formation. From the simulations, the maximum keyhole depths were found to be 74 µm, 114 µm, and 126 µm, for 173.0 W, 201.3 W, and 230.0 W, respectively, while the keyhole lengths (along the direction of laser scanning) were found to be 222 µm, 222 µm, and 263 µm, respectively.
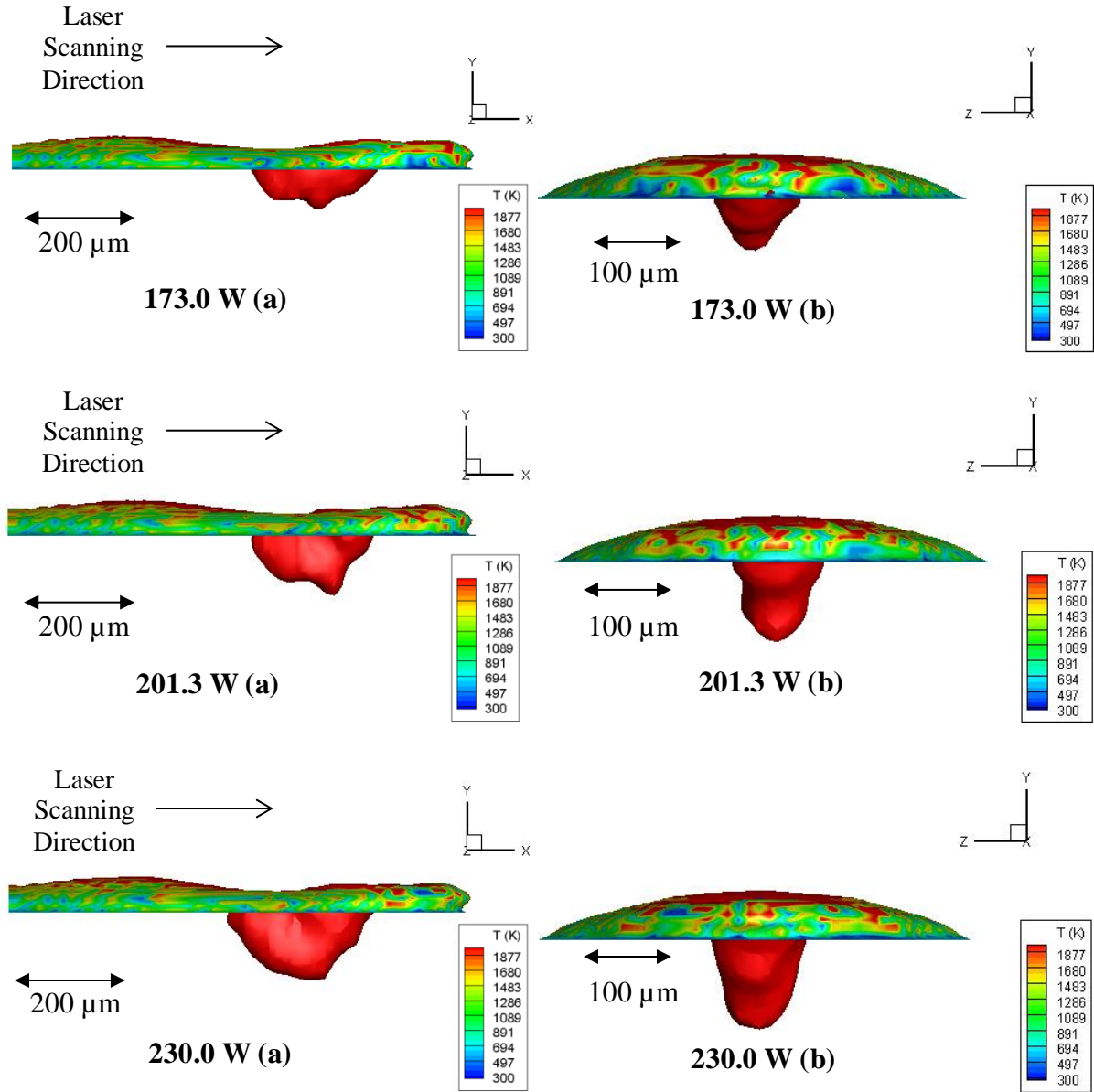
Figure 3.23: Single-track depositions for three laser power settings: (a) Side view of L-BPF deposition showing keyhole length and depth and (b) front view of deposition depicting keyhole width

Discussion

In an effort to reduce simulation time, the initial powder placement is performed on a significantly smaller domain than the size of the substrate. Instead, tessellations of the powder bed are used to generate a sufficiently large powder bed which can be used to simulate larger domains, which are observable in Figure 3.22(b) via the crisp lines where no powder is observed parallel to the x-axis. If ray-tracing were being utilized as the energy transfer mechanism between

the laser and the powder bed, this could have an impact on powder heating; however, since volumetric heating methods were used to distribute the laser energy, and the gap between tessellations (~2 μm) of the powder bed is less than one discretization of the fine mesh (15 μm), the solution will not be significantly affected.

Since the powder bed height will affect the energy transfer to the substrate, it is imperative to acquire a powder bed representative of that observed during experimentation. During the powder placement process simulation, it was observed that the more spreading operations which had occurred, the more settling of smaller particle diameters close to the substrate surface were observed. For thicker powder beds, this resulting behavior is favorable, since smaller particles would be affected by denudation much more readily than larger ones, and the larger particles of the powder bed will provide shielding to smaller ones. Depending on the initial height of the powder bed, multiple spreading passes will be necessary to ensure a uniform powder bed thickness, since the smaller powder requires perturbation to fill in voids produced by larger particles. With a maximum particle diameter of 64 microns, if a thinner powder bed thickness were used, the largest particles wouldn't spread, but rather act as an extension of the spreading bar. Sutton et al. (Sutton et al., 2017) discuss limitations to powder size, which can be used for powder bed fusion processes. The large powder can lead to porosity and poor spreading, while the small powder is more susceptible to evaporation before being added to the molten pool. The DEM simulation performed with three spreading passes closely resembled the final powder bed height of 101 microns when the untouched powder was viewed via optical profile measurement, as shown in Figure 3.20. By spreading the powder using three passes, the height of the powder bed was reduced by approximately 20%, primarily due to forcing smaller particles deeper into the powder bed, increasing the overall packing efficiency.

During experimentation at 220W and higher laser power settings, an evaporation plume was clearly evident throughout the deposition process, substantiating the model observation of keyhole formation. Once a keyhole has been formed, the material is more susceptible to maintaining the keyhole, primarily due to the increased surface area which allows for higher overall absorptivity of the laser energy source (Svenungsson et al., 2015). In each of the cases investigated, a relatively shallow keyhole is formed for two reasons: (1) Powdered material is being added to the molten pool causing localized quenching, and (2) high scan speeds prevent the accumulation of thermal energy. Figure 3.24 shows a contour plot depicting the molten pool

region and the established keyhole with velocity vectors included to show the directionality of the evaporation plume. The maximum velocity in the gas domain in the 230.0 W is due to evaporation is 220 m/s at the leading face of the keyhole wall while the maximum velocity in the molten region is approximately 2.0 m/s and is maximum near the bottom of the keyhole due to the recirculation of molten Ti-6Al-4V to the lagging face of the keyhole.
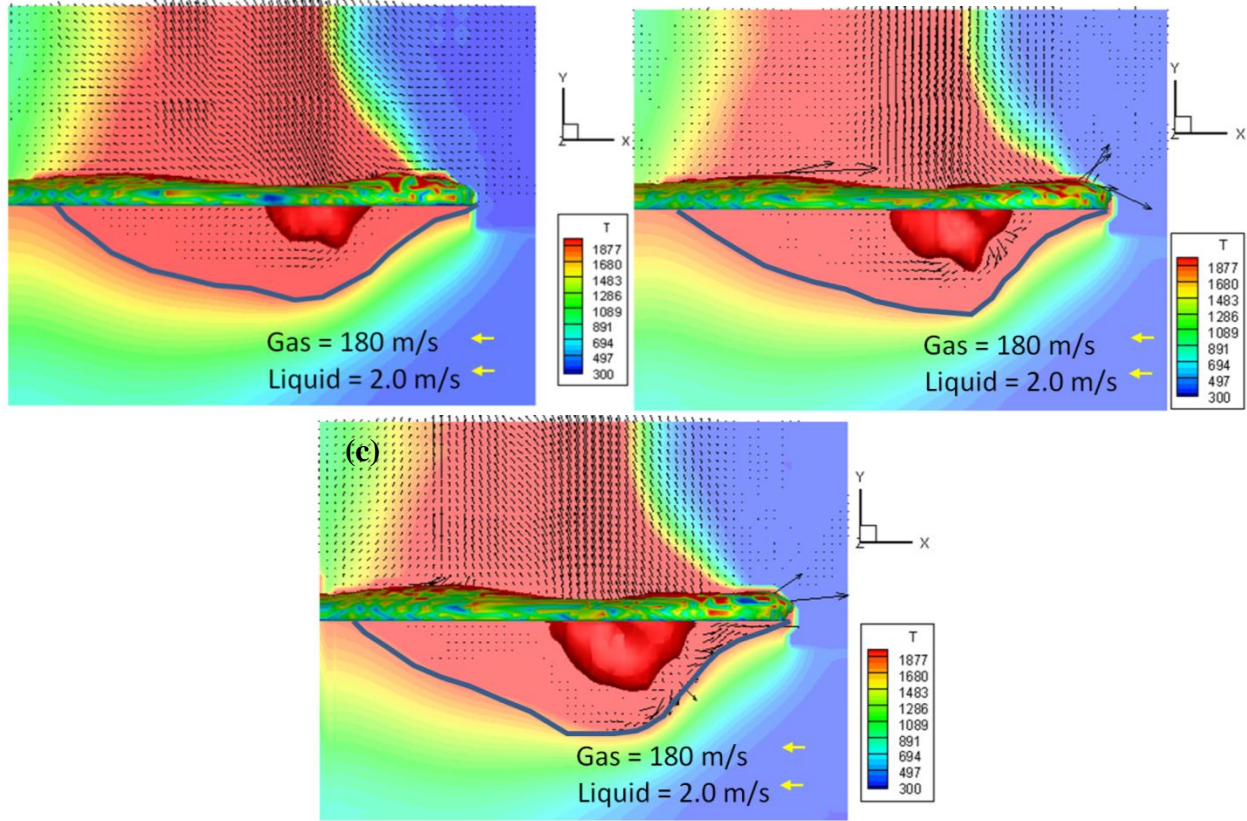
Figure 3.24: Keyhole geometry and gas velocities at (a) 173.0 W, (b) 201.3. W, and (c) 230.0 W

With cross-sectional slices of the deposition extracted (Figure 3.21), the track height as a function of lateral distance along the track was analyzed to determine the cross-sectional area of the deposition via numerical integration. Equation (3.24) provides the expression used to acquire cross-sectional areas for both the experimental data as well as the simulated track

$$A_{track} = \int (H(x) - H_o)dx$$

(3.24)

where A_{track} is the cross-sectional area of the track and $(H(x) - H_o)$ denotes the track height at a given location along the cross-section. Cross-sectional track areas for the 173.0 W, 201.3 W and 230.0 W cases were found to be 12490 μm², 16250 μm², and 21240 μm², while the simulated cross-sectional areas we calculated to be 14230 μm², 20750 μm², and 19660 μm², resulting in an error of 13.9%, 27.7%, and -7.4%, respectively. Differences observed between the experimental data and simulated results could be due to local sparsity in the experimental powder bed compared to the one generated for the simulation, and is substantiated with the optical profile images in Figure 3.20, where localized pockets exist with low powder coverage. The simulation results from the highest laser power setting indicate that less powder was captured, which could be explained by particle motion due to evaporation-induced acceleration causing less powder to be available locally adjacent to the molten pool. Particle motion in the 230.0 W laser power simulation is shown in Figure 3.25, where particle displacement from the original powder bed is apparent.
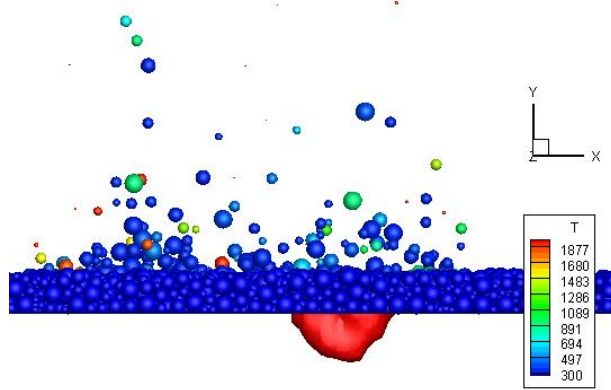
Figure 3.25: Powder bed displacement at 230.0 W laser power setting (Temperature is displayed in Kelvin)

The simulations performed in this work required 5008 CPU-hrs to simulate a millimeter of laser travel distance on an Intel E5-2660 v3 with a 2.6 GHz clock speed. One of the most highly cited models in literature for full-physics simulation of the L-PBF process indicates that computational effort of approximately 100,000 CPU-hrs was necessary to simulate L-PBF for approximately 1.0 mm of travel distance (Khairallah et al., 2016), yielding a computational efficiency of approximately 100 CPU-hrs per micron of laser travel distance. The model presented in this work required 5 CPU-hours per micron, an improvement of 95% for computational effort.

In conclusion, this case study demonstrated a model to describe an L-PBF process using a volumetric heat source for powder heating for three laser power settings at a scanning speed of 84.6 mm/s. By eliminating the requirement of using a ray-tracing model for the powder bed energy absorption, the computational effort was reduced by nearly 95% compared to other models discussed within the literature. Though gas dynamics were included within the model, and particle motion was apparent to varying extents for each laser power simulated, the primary driver for increased capture efficiency was due to molten pool spread, as opposed to particles being propelled into the molten pool from the induced evaporation plume. Higher laser power generated a wider molten pool, which was able to trap additional particles not directly melted by the laser irradiation. Lower capture efficiency for the highest laser power; however, is believed to be directly impacted by evaporated gas causing particles to be ejected from the vicinity of the molten pool.

CHAPTER 4.   FUTURE WORK

In light of the computational improvements completed in the research presented, there is still significant improvement that can be made. Ideally, the high-fidelity model would be leveraged as a design tool, preventing the necessity of performing experiments to information about resulting track geometry. As indicated in Section 2.2.2, temperature field information becomes critical in understanding the resulting material properties, since material strength, brittleness, and resistance to corrosion and/or wear can be altered depending on the cooling rate observed during deposition.

High-fidelity models are significantly limited by the rate at which they are able to produce data to describe large-scale depositions. Typical manufactured components consist of multi-track and multi-layered depositions and could involve complex geometries with many edges and non-uniformities. Unfortunately, using high-fidelity modeling to simulate such an extensive process suffers from high computational burden while low-fidelity modeling sacrifices solution accuracy. A combination of modeling activities can be used to establish instances where high-fidelity models must be used to capture the physics of a given AM process. For example, the characterization of edge effects can be performed with a relatively simple conduction model to assess how thermal energy dissipates, which would direct an analyst to use the high-fidelity model to understand the impact of those effects on the resulting deposition. The decision on whether or not the high-fidelity model is necessary can be driven by a machine learning algorithm called a support vector machine (SVM), which can categorize data into two classes and must be trained. Typically, manual training of SVM is performed by acquiring an entire training data set, and fitting a hyperplane between the two categories of data to maximize the margin (Cortes and Vapnik, 1995, Steinwart and Christmann, 2008). Alternatively, a smart selection process can be used to provide active learning of an SVM, which uses a smaller number of trials adjacent to a previously fitted hyperplane to improve accuracy only where it is essential (2001, 2000).

In addition to leveraging modeling activities to train a machine learning algorithm, experimentation can be used to gain some basic insights into a particular process to understand the limitations of the process parameters to produce a favorable product, such as determining if there is sufficient powder feed rate and/or energy density for track formation. During this initial

parameter optimization, data can be collected for model validation and used to determine track and molten pool geometry. This data can also be used to train a data-driven model through a combination of tools such as regression analysis, artificial neural networks, and support vector machines to obtain geometrical information about the deposition process for various process conditions. To build a data-driven model, features must be carefully selected which would be able to provide correlation to each of the desired outputs. For example, the effect of increasing powder feed rate or laser power density is known to correlate to track height since an increase in energy and/or available powder at the surface of the molten pool augments the possibility of powder being absorbed (Caiazzo and Caggiano, 2018). Other relationships for additive manufacturing processes have similarly intuitive trends and have been documented in available literature (Saqib et al., 2014, Onwubolu et al., 2007, Sun and Hao, 2012), though quantification of those trends generally remains system-dependent. An investigation into the feature selection process can enable selecting high quality features for use in subsequent analysis with a data-driven model.

APPENDIX A: LASER BEAM CHARACTERIZATION AND ANALYSIS

Images for remaining laser power settings from section 2.1.3 have been included here.
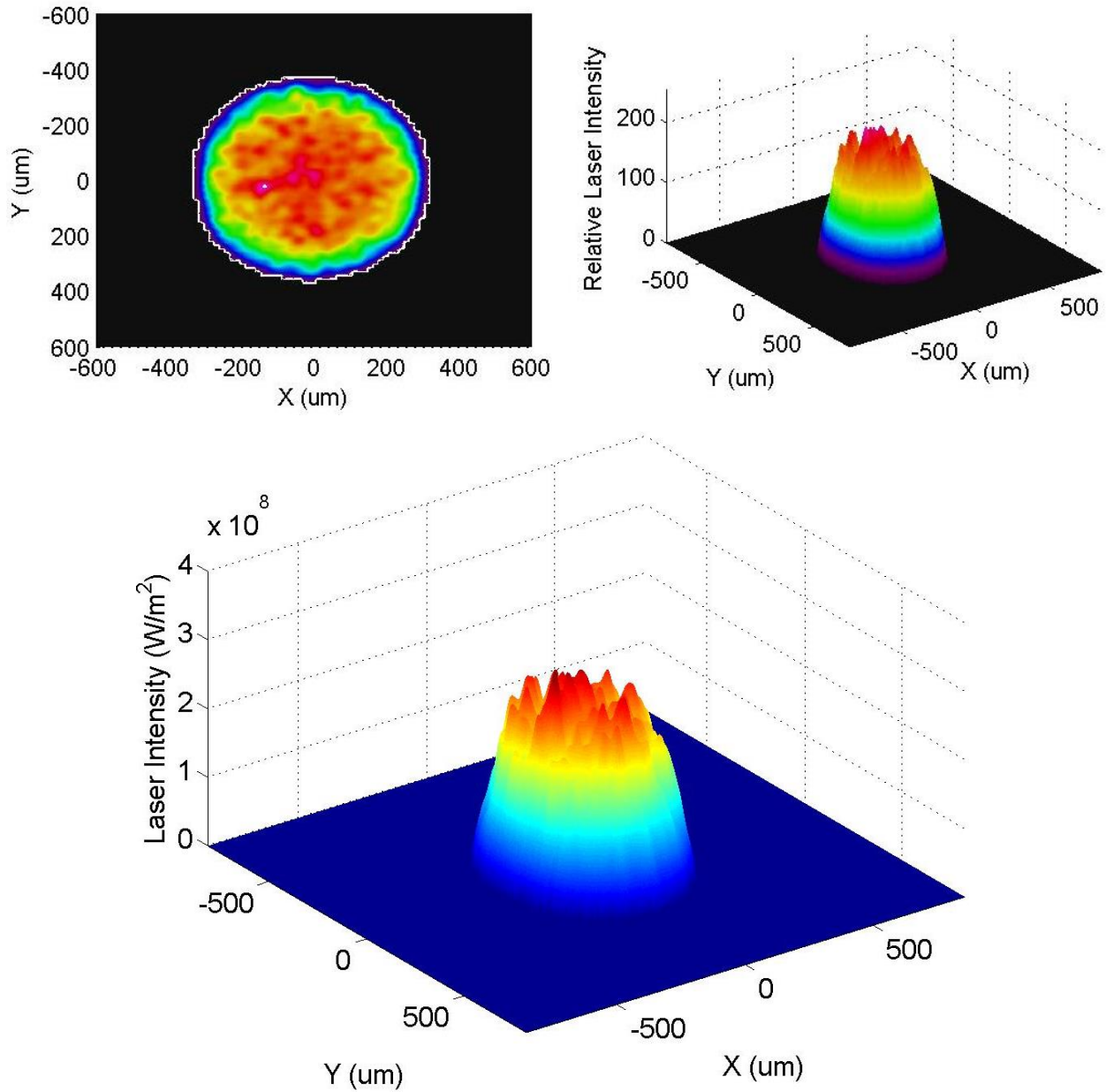
Figure A.1: Post-Processed Results for Laser Intensity Profile at 61.5W
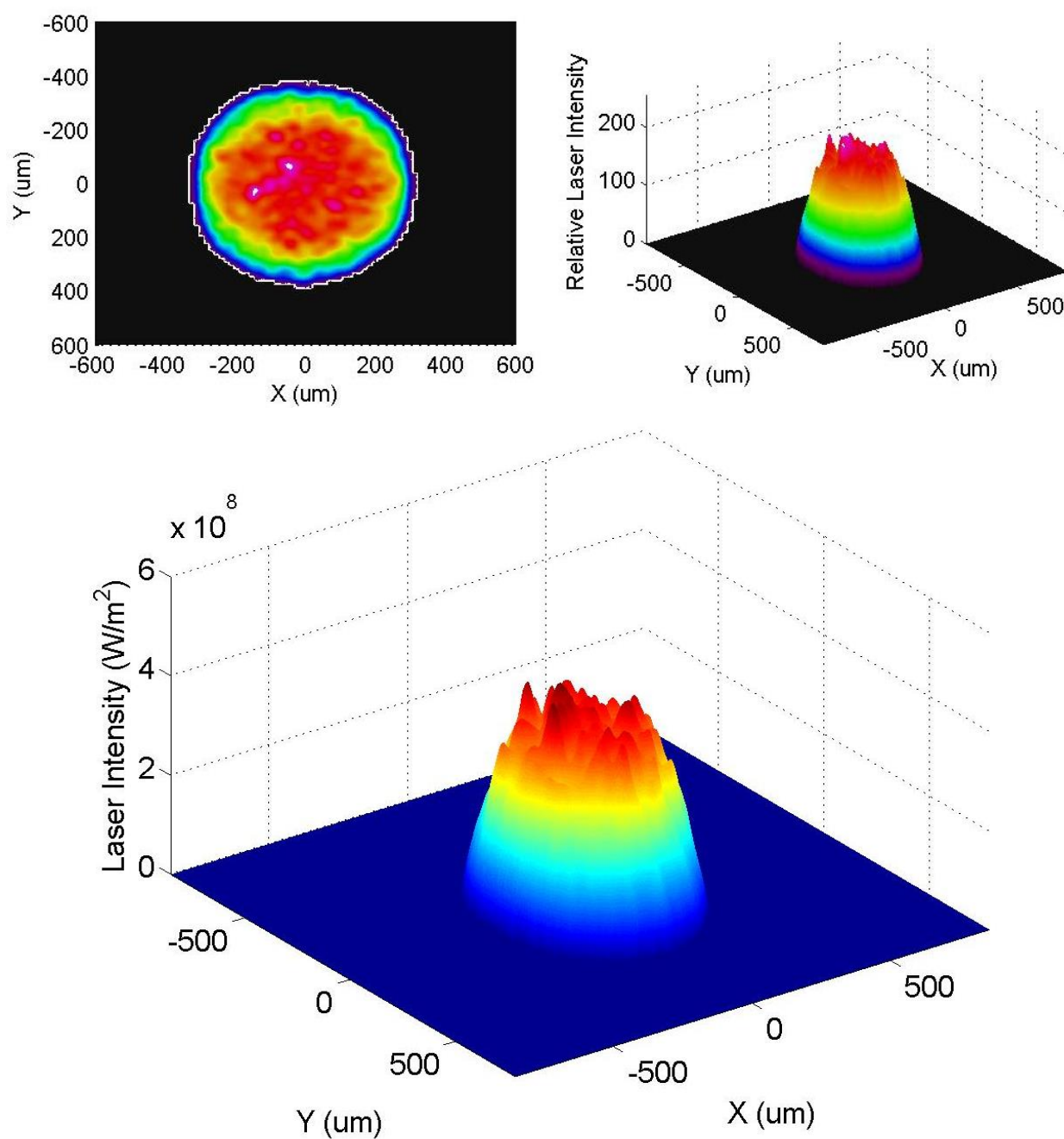
Figure A.2: Post-Processed Results for Laser Intensity Profile at 96W
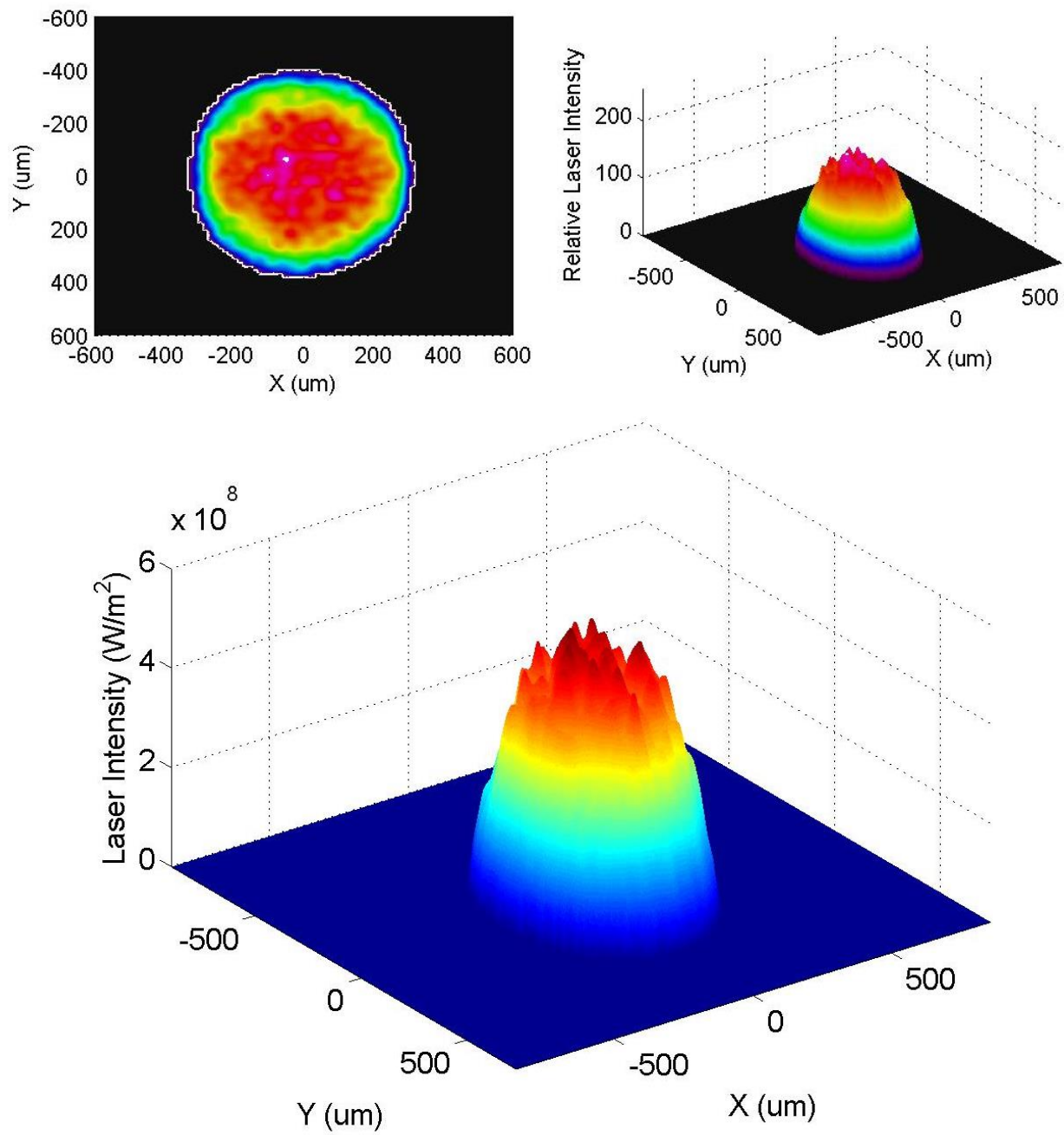
Figure A.3: Post-Processed Results for Laser Intensity Profile at 124W
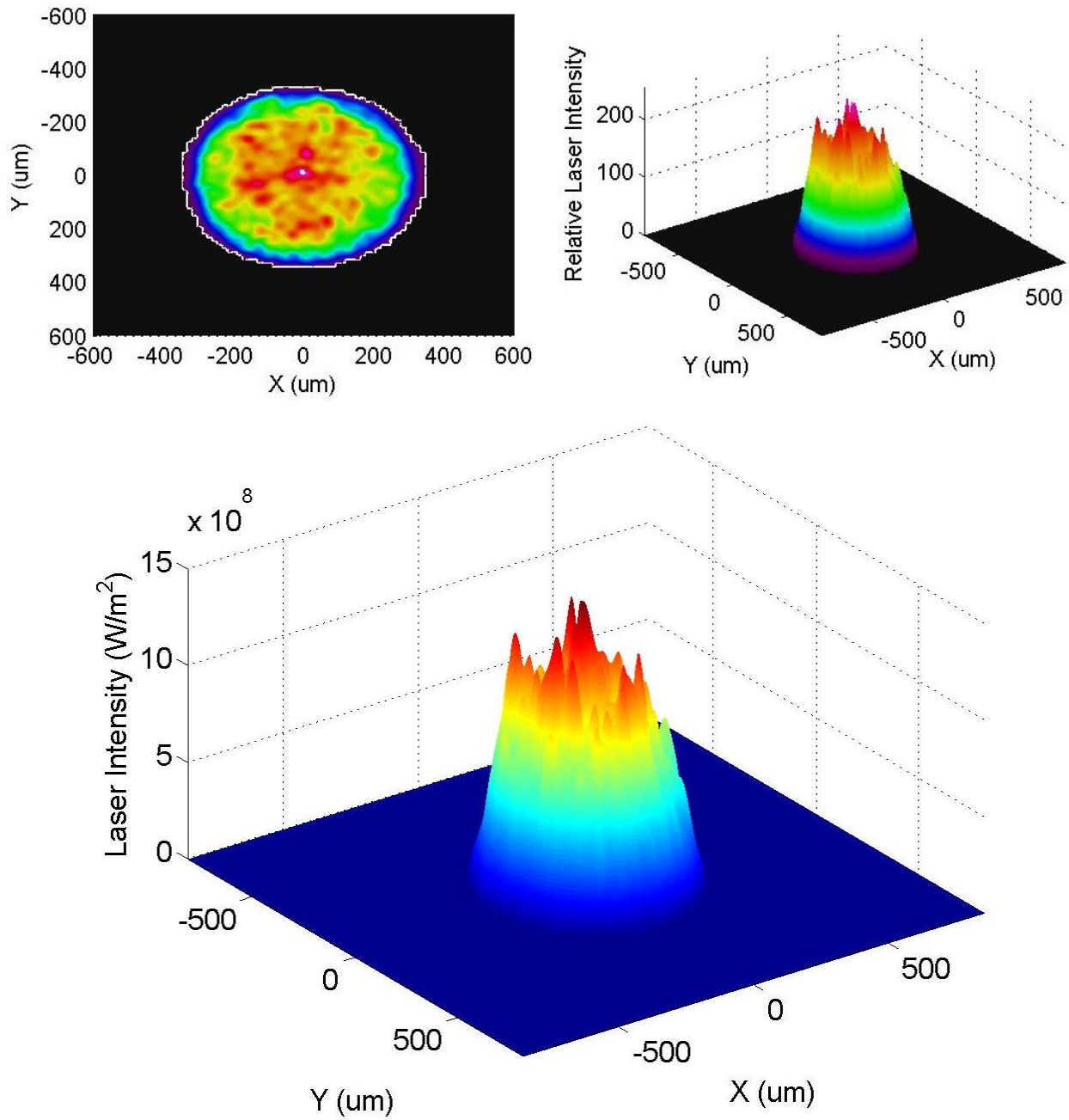
Figure A.4: Post-Processed Results for Laser Intensity Profile at 245W

REFERENCES

"Titanium Alloy Ti 6Al-4V" [Online]. Dynamet Holdings Inc. Available: https://cartech.ides.com/datasheet.aspx?i=101&E=269 [Accessed on 07/17/2017].

"Titanium Alloys - Ti6Al4V Grade 5" [Online]. U.S. Titanium Industry Inc. Available: http://www.azom.com/article.aspx?ArticleID=1547 [Accessed on 07/16/2017].

AHN, H. T. & KALLINDERIS, Y. 2006. Strongly coupled flow/structure interactions with a geometrically conservative ALE scheme on general hybrid meshes. *Journal of Computational Physics,* 219**,** 671-696.

ALESHIN, S. 1996. Coaxial single point powder feed nozzle. Google Patents.

ANSYS. 2009. *Fluent 12.0 Theory Guide*.

ATWOOD, C., GRIFFITH, M., SCHLIENGER, M., HARWELL, L., ENSZ, M., KEICHER, D., SCHLIENGER, M., ROMERO, J. & SMUGERESKY, J. Laser engineered net shaping (LENS): a tool for direct fabrication of metal parts. Proceedings of ICALEO, 1998. 16-19.

BAILEY, N. S., KATINAS, C. & SHIN, Y. C. 2017. Laser direct deposition of AISI H13 tool steel powder with numerical modeling of solid phase transformation, hardness, and residual stresses. *Journal of Materials Processing Technology,* 247**,** 223-233.

BANERJEE, R., COLLINS, P., GENC, A. & FRASER, H. 2003. Direct laser deposition of in situ Ti–6Al–4V–TiB composites. *Materials Science and Engineering: A,* 358**,** 343-349.

BEDENKO, D., KOVALEV, O., SMUROV, I. & ZAITSEV, A. 2016. Numerical simulation of transport phenomena, formation the bead and thermal behavior in application to industrial DMD technology. *International Journal of Heat and Mass Transfer,* 95**,** 902-912.

BELYTSCHKO, T. & HUGHES, T. J. 1983. Computational methods for transient analysis. *Amsterdam, North-Holland(Computational Methods in Mechanics.,* 1.

BENENATI, R. & BROSILOW, C. 1962. Void fraction distribution in beds of spheres. *AIChE Journal,* 8**,** 359-361.

BERTOLI, U. S., GUSS, G., WU, S., MATTHEWS, M. J. & SCHOENUNG, J. M. 2017. In-situ characterization of laser-powder interaction and cooling rates through high-speed imaging of powder bed fusion additive manufacturing. *Materials & Design,* 135**,** 385-396.

BHAVAR, V., KATTIRE, P., PATIL, V., KHOT, S., GUJAR, K. & SINGH, R. 2017. A review on powder bed fusion technology of metal additive manufacturing. *Additive manufacturing handbook***,** 251-253.

BIAN, L., THOMPSON, S. M. & SHAMSAEI, N. 2015. Mechanical properties and microstructural features of direct laser-deposited Ti-6Al-4V. *Jom,* 67**,** 629-638.

BOIVINEAU, M., CAGRAN, C., DOYTIER, D., EYRAUD, V., NADAL, M.-H., WILTHAN, B. & POTTLACHER, G. 2006. Thermophysical properties of solid and liquid Ti-6Al-4V (TA6V) alloy. *International Journal of Thermophysics,* 27**,** 507-529.

BOLEY, C., KHAIRALLAH, S. A. & RUBENCHIK, A. M. 2015. Calculation of laser absorption by metal powders in additive manufacturing. *Applied optics,* 54, 2477-2482.

BURNS, S. J., PIIROINEN, P. T. & HANLEY, K. J. 2019. Critical time step for DEM simulations of dynamic systems using a Hertzian contact model. *International Journal for Numerical Methods in Engineering,* 119**,** 432-451.

CAIAZZO, F. & CAGGIANO, A. 2018. Laser direct metal deposition of 2024 Al alloy: trace geometry prediction via machine learning. *Materials,* 11**,** 444.

CALIGNANO, F. 2020. Additive Manufacturing (AM) of Metallic Alloys. *Crystals,* 10**,** 704.

CARSLAW, H. S. & JAEGER, J. C. 1959. Conduction of heat in solids. *Oxford: Clarendon Press, 1959, 2nd ed.*

CASADEBAIGT, A., HUGUES, J. & MONCEAU, D. 2020. High temperature oxidation and embrittlement at 500–600° C of Ti-6Al-4V alloy fabricated by Laser and Electron Beam Melting. *Corrosion Science,* 175**,** 108875.

CHANDE, T. & MAZUMDER, J. 1985. Two-dimensional, transient model for mass transport in laser surface alloying. *Journal of applied physics,* 57**,** 2226-2232.

CHIUMENTI, M., LIN, X., CERVERA, M., LEI, W., ZHENG, Y. & HUANG, W. 2017. Numerical simulation and experimental calibration of Additive Manufacturing by blown powder technology. Part I: thermal analysis. *Rapid Prototyping Journal,* 23**,** 448-463.

CORTES, C. & VAPNIK, V. 1995. Support-vector networks. *Machine learning,* 20**,** 273-297.

CRIALES, L. E. & ÖZEL, T. 2017. Temperature profile and melt depth in laser powder bed fusion of Ti-6Al-4V titanium alloy. *Progress in Additive Manufacturing,* 2**,** 169-177.

CROWE, C. 1982. Review—Numerical models for dilute gas-particles flows. *Trans. of ASME J. of Fluid Eng,* 104**,** 297-303.

CUNDALL, P. A. & STRACK, O. D. 1979. A discrete numerical model for granular assemblies. *geotechnique,* 29**,** 47-65.

D'OLIVEIRA, A. S. C., DA SILVA, P. S. C. & VILAR, R. M. 2002. Microstructural features of consecutive layers of Stellite 6 deposited by laser cladding. *Surface and Coatings Technology,* 153**,** 203-209.

DE OLIVEIRA, U., OCELIK, V. & DE HOSSON, J. T. M. 2005. Analysis of coaxial laser cladding processing conditions. *Surface and Coatings Technology,* 197**,** 127-136.

DENNEY, P. The process development for a portable Nd: YAG laser materials processing system. International Congress on Applications of Lasers & Electro-Optics, 1991. LIA, 140-149.

DINIZ NETO, O., ALCALDE, A. & VILAR, R. 2007. Interaction of a focused laser beam and a coaxial powder jet in laser surface processing. *Journal of Laser Applications,* 19**,** 84-88.

DONACHIE, M. J. 2000. Titanium: A Technical Guide. *ASM International, Materials Park, OH***,** 5-11.

DULLIEN, F. A. 2012. *Porous media: fluid transport and pore structure*, Academic press.

ELDER, F., GUREWITSCH, A., LANGMUIR, R. & POLLOCK, H. 1947. Radiation from electrons in a synchrotron. *Physical Review,* 71**,** 829.

FATHI, A., TOYSERKANI, E., KHAJEPOUR, A. & DURALI, M. 2006. Prediction of melt pool depth and dilution in laser powder deposition. *Journal of Physics D: Applied Physics,* 39**,** 2613.

FEDKIW, R. P., ASLAM, T., MERRIMAN, B. & OSHER, S. 1999. A non-oscillatory Eulerian approach to interfaces in multimaterial flows (the ghost fluid method). *Journal of computational physics,* 152**,** 457-492.

FRENK, A., VANDYOUSSEFI, M., WAGNIERE, J.-D., KURZ, W. & ZRYD, A. 1997. Analysis of the laser-cladding process for stellite on steel. *Metallurgical and Materials transactions B,* 28**,** 501-508.

FU, Y., LOREDO, A., MARTIN, B. & VANNES, A. 2002. A theoretical model for laser and powder particles interaction during laser cladding. *Journal of materials processing technology,* 128**,** 106-112.

GAN, Z., LIAN, Y., LIN, S. E., JONES, K. K., LIU, W. K. & WAGNER, G. J. 2019. Benchmark Study of Thermal Behavior, Surface Topography, and Dendritic Microstructure in Selective Laser Melting of Inconel 625. *Integrating Materials and Manufacturing Innovation***,** 1-16.

GHODS, S. & HERRMANN, M. 2013. A consistent rescaled momentum transport method for simulating large density ratio incompressible multiphase flows using level set methods. *Physica Scripta,* 2013**,** 014050.

GIBSON, I., ROSEN, D. & STUCKER, B. 2015. Directed Energy Deposition Processes. *Additive Manufacturing Technologies.* Springer.

GRIFFITH, M., KEICHER, D., ATWOOD, C., ROMERO, J., SMUGERESKY, J., HARWELL, L. & GREENE, D. Free form fabrication of metallic components using laser engineered net shaping (LENS). 1996 International Solid Freeform Fabrication Symposium, 1996.

GROPP, W. & LUSK, E. 1996. User's Guide for mpich, a Portable Implementation of MPI. Mathematics and Computer Science Division, Argonne National Laboratory ….

GÜRTLER, F.-J., KARG, M., LEITZ, K.-H. & SCHMIDT, M. 2013. Simulation of laser beam melting of steel powders using the three-dimensional volume of fluid method. *Physics Procedia,* 41**,** 881-886.

GUSAROV, A. & KRUTH, J.-P. 2005. Modelling of radiation transfer in metallic powders at laser treatment. *International Journal of Heat and Mass Transfer,* 48**,** 3423-3434.

GUSAROV, A. & SMUROV, I. 2010. Modeling the interaction of laser radiation with powder bed at selective laser melting. *Physics Procedia,* 5**,** 381-394.

H.-J., K. & KIM, Y. 1999. Wear and corrosion resistance of PTA weld surfaced Ni and Co based alloy layers. *Surface engineering,* 15**,** 495-501.

HAERI, S. 2017. Optimisation of blade type spreaders for powder bed preparation in Additive Manufacturing using DEM simulations. *Powder technology,* 321**,** 94-104.

HAERI, S., WANG, Y., GHITA, O. & SUN, J. 2017. Discrete element simulation and experimental study of powder spreading process in additive manufacturing. *Powder Technology,* 306**,** 45-54.

HAIDER, A. & LEVENSPIEL, O. 1989. Drag Coefficient and Terminal Velocity of Spherical and Nonspherical Particles. *Powder technology,* 58**,** 63-70.

HAN, L., PHATAK, K. & LIOU, F. 2004. Modeling of laser cladding with powder injection. *Metallurgical and Materials transactions B,* 35**,** 1139-1150.

HE, X., FUERSCHBACH, P. W. & DEBROY, T. 2003. Heat transfer and fluid flow during laser spot welding of 304 stainless steel. *Journal of Physics D: Applied Physics,* 36**,** 1388.

HE, X. & MAZUMDER, J. 2007. Transport phenomena during direct metal deposition. *Journal of Applied Physics,* 101**,** 053113.

HE, X., YU, G. & MAZUMDER, J. 2010. Temperature and Composition Profile During Double-Track Laser Cladding of H13 Tool Steel. *Journal of Physics D: Applied Physics,* 43**,** 015502.

HEIGEL, J., MICHALERIS, P. & REUTZEL, E. 2015. Thermo-mechanical model development and validation of directed energy deposition additive manufacturing of Ti–6Al–4V. *Additive Manufacturing,* 5**,** 9-19.

HENRI, P., JONNE, N., SEBASTIAN, T., JARI, T., STEFFEN, N. & PETRI, V. Laser cladding with coaxial wire feeding. International Congress on Applications of Lasers & Electro-Optics, 2012. LIA, 1196-1201.

HOADLEY, A., FRENK, A. & MARSDEN, C. A process overview of laser hardfacing. Proc. I Int. Conf. Surface Engineering: Practice and Prospects, Adelaide, Australia, 1991. 12-14.

HOADLEY, A. & RAPPAZ, M. 1992. A thermal model of laser cladding by powder injection. *Metallurgical transactions B,* 23**,** 631-642.

HUANG, D., LEWIS, I. C., CATE, W. D. & LEWIS, R. T. 2004. Manufacture of carbon/carbon composites by hot pressing. Google Patents.

HULTGREN, R. & DESAI, P. D. Selected values of the thermodynamic properties of the elements. 1973. American Society for Testing and Materials.

HUNT, J., DERGUTI, F. & TODD, I. 2014. Selection of steels suitable for additive layer manufacturing. *Ironmaking & Steelmaking,* 41**,** 254-256.

IBARRA-MEDINA, J. & PINKERTON, A. J. 2011. Numerical investigation of powder heating in coaxial laser metal deposition. *Surface Engineering,* 27**,** 754-761.

IBARRA-MEDINA, J., VOGEL, M. & PINKERTON, A. J. 2011. A CFD Model of Laser Cladding: From Deposition Head to Melt Pool Dynamics. *Proceedings of ICALEO***,** 23-27.

ISANAKA, S. P., KARNATI, S. & LIOU, F. 2016. Blown powder deposition of 4047 aluminum on 2024 aluminum substrates. *Manufacturing Letters,* 7**,** 11-14.

IVANCHENKO, V., IVASISHIN, O. & SEMIATIN, S. 2003. Evaluation of evaporation losses during electron-beam melting of Ti-Al-V alloys. *Metallurgical and Materials Transactions B,* 34**,** 911-915.

JENG, M.-C., YAN, L.-Y. & DOONG, J.-L. 1991. Wear behaviour of cobalt-based alloys in laser surface cladding. *Surface and Coatings Technology,* 48**,** 225-231.

JIA, T., ZHANG, Y. & CHEN, J. 2011. Dynamic simulation of particle packing with different size distributions. *Journal of manufacturing science and engineering,* 133.

JOHNSON, P. & CHRISTY, R. 1974. Optical constants of transition metals: Ti, v, cr, mn, fe, co, ni, and pd. *Physical review B,* 9**,** 5056.

JOUVARD, J. M., GREVEY, D., LEMOINE, F. & VANNES, A. 1997. Continuous wave Nd: YAG laser cladding modeling: a physical study of track creation during low power processing. *Journal of Laser Applications,* 9**,** 43-50.

KADER, B. 1981. Temperature and Concentration Profiles in Fully Turbulent Boundary Layers. *International Journal of Heat and Mass Transfer,* 24**,** 1541-1544.

KARAYAGIZ, K., ELWANY, A., TAPIA, G., FRANCO, B., JOHNSON, L., MA, J., KARAMAN, I. & ARRÓYAVE, R. 2019. Numerical and experimental analysis of heat distribution in the laser powder bed fusion of Ti-6Al-4V. *IISE Transactions,* 51**,** 136-152.

KATINAS, C., LIU, S. & SHIN, Y. C. 2019. Self-Sufficient Modeling of Single Track Deposition of Ti–6Al–4V With the Prediction of Capture Efficiency. *Journal of Manufacturing Science and Engineering,* 141**,** 011001.

KATINAS, C., SHANG, W., SHIN, Y. C. & CHEN, J. 2018. Modeling Particle Spray and Capture Efficiency for Direct Laser Deposition Using a Four Nozzle Powder Injection System. *Journal of Manufacturing Science and Engineering,* 140**,** 041014.

KATINAS, C. & SHIN, Y. C. 2020. Prediction of initial transient behavior with stationary heating during laser powder bed fusion processes. *International Journal of Heat and Mass Transfer,* 153**,** 119663.

KATINAS, C., THROOP, T., SHIN, Y. C. & FRANK, A. 2021. Laser cladding of Stellite-6 with a coaxial nozzle via modeling and systematic experimental investigations. *The International Journal of Advanced Manufacturing Technology,* 113**,** 837-853.

KHAIRALLAH, S. A. & ANDERSON, A. 2014. Mesoscopic simulation model of selective laser melting of stainless steel powder. *Journal of Materials Processing Technology,* 214**,** 2627-2636.

KHAIRALLAH, S. A., ANDERSON, A. T., RUBENCHIK, A. & KING, W. E. 2016. Laser powder-bed fusion additive manufacturing: Physics of complex melt flow and formation mechanisms of pores, spatter, and denudation zones. *Acta Materialia,* 108**,** 36-45.

KING, W. E., ANDERSON, A. T., FERENCZ, R., HODGE, N., KAMATH, C., KHAIRALLAH, S. A. & RUBENCHIK, A. M. 2015a. Laser powder bed fusion additive manufacturing of metals; physics, computational, and materials challenges. *Applied Physics Reviews,* 2**,** 041304.

KING, W. E., ANDERSON, A. T., FERENCZ, R. M., HODGE, N. E., KAMATH, C., KHAIRALLAH, S. A. & RUBENCHIK, A. M. 2015b. Laser powder bed fusion additive manufacturing of metals; physics, computational, and materials challenges. *Applied Physics Reviews,* 2**,** 041304.

KING, W. E., BARTH, H. D., CASTILLO, V. M., GALLEGOS, G. F., GIBBS, J. W., HAHN, D. E., KAMATH, C. & RUBENCHIK, A. M. 2014. Observation of keyhole-mode laser melting in laser powder-bed fusion additive manufacturing. *Journal of Materials Processing Technology,* 214**,** 2915-2925.

KOBRYN, P., MOORE, E. & SEMIATIN, S. 2000. The effect of laser power and traverse speed on microstructure, porosity, and build height in laser-deposited Ti-6Al-4V. *Scripta Materialia,* 43**,** 299-305.

KÖHLER, H., JAYARAMAN, V., BROSCH, D., HUTTER, F. & SEEFELD, T. 2013. A novel thermal sensor applied for laser materials processing. *Physics Procedia,* 41**,** 502-508.

LALAS, C., TSIRBAS, K., SALONITIS, K. & CHRYSSOLOURIS, G. 2007. An analytical model of the laser clad geometry. *The International Journal of Advanced Manufacturing Technology,* 32**,** 34-41.

LAUNDER, B. E. & SPALDING, D. 1974. The Numerical Computation of Turbulent Flows. *Computer methods in applied mechanics and engineering,* 3**,** 269-289.

LAUNDER, B. E. & SPALDING, D. B. 1983. The numerical computation of turbulent flows. *Numerical Prediction of Flow, Heat Transfer, Turbulence and Combustion.* Elsevier.

LEE, Y. & ZHANG, W. Mesoscopic simulation of heat transfer and fluid flow in laser powder bed additive manufacturing. International Solid Free Form Fabrication Symposium, Austin, 2015. 1154-1165.

LEE, Y. & ZHANG, W. 2016. Modeling of heat transfer, fluid flow and solidification microstructure of nickel-base superalloy fabricated by laser powder bed fusion. *Additive Manufacturing,* 12**,** 178-188.

LEMOINE, F., GREVEY, D., VASTRA-BOBIN, I. & VANNES, A. 1993. Laser-cladding cross-section modeling obtained by metallic powder spraying into an Nd: YAG laser beam. *Journal de Physique II, I,* 3**,** 2043-52.

LI, D. & MERKLE, C. L. 2006. A unified framework for incompressible and compressible fluid flows. *Journal of Hydrodynamics, Ser. B,* 18**,** 113-119.

LIN, J. 2000. Numerical Simulation of the Focused Powder Streams in Coaxial Laser Cladding. *Journal of Materials Processing Technology,* 105**,** 17-23.

LIN, J. & HWANG, B.-C. 1999. Coaxial laser cladding on an inclined substrate. *Optics & Laser Technology,* 31**,** 571-578.

LIN, J. & STEEN, W. 1998. Design characteristics and development of a nozzle for coaxial laser cladding. *Journal of Laser Applications,* 10**,** 55-63.

LIN, J. & STEEN, W. M. Powder Flow and Catchment During Coaxial Laser Cladding. Proceedings of SPIE, 1997. Munich, Germany: International Society for Optics and Photonics, 517-528.

LIN, Y., MCHUGH, K. H., ZHOU, Y. & LAVERNIA, E. J. 2007. Modeling the spray forming of H13 steel tooling. *Metallurgical and Materials Transactions A,* 38**,** 1632-1637.

LIU, J. & LI, L. 2005. Effects of powder concentration distribution on fabrication of thin-wall parts in coaxial laser cladding. *Optics & Laser Technology,* 37**,** 287-292.

LIU, J., LI, L., ZHANG, Y. & XIE, X. 2005. Attenuation of laser power of a focused Gaussian beam during interaction between a laser and powder in coaxial laser cladding. *Journal of Physics D: Applied Physics,* 38**,** 1546.

LIU, S., LIU, Z., WANG, Y. & TANG, J. 2014a. A comparative study on the high temperature corrosion of TP347H stainless steel, C22 alloy and laser-cladding C22 coating in molten chloride salts. *Corrosion Science,* 83**,** 396-408.

LIU, S., LIU, Z., WANG, Y. & YUE, P. 2014b. Ti-based composite coatings with gradient TiCx reinforcements on TC4 titanium alloy prepared by laser cladding. *Science China Technological Sciences,* 57**,** 1454-1461.

LIU, S. & SHIN, Y. C. 2019. Additive manufacturing of Ti6Al4V alloy: A review. *Materials & Design,* 164**,** 107552.

LYLE, B. L. & LEVINE, E. 2018. *ADDITIVE MANUFACTURING BENCHMARK TEST SERIES - AMB2018-02 Description. https://*www.nist.gov/ambench/amb2018-02-description/ [Online]. NIST. [Accessed on January 15, 2019].

MAHAMOOD, R. & AKINLABI, E. 2015. Laser metal deposition of functionally graded Ti6Al4V/TiC. *Materials & Design,* 84**,** 402-410.

MAHAMOOD, R. M., AKINLABI, E. T., SHUKLA, M. & PITYANA, S. 2013. Scanning velocity influence on microstructure, microhardness and wear resistance performance of laser deposited Ti6Al4V/TiC composite. *Materials & Design,* 50**,** 656-666.

MANVATKAR, V., DE, A. & DEBROY, T. 2015a. Spatial variation of melt pool geometry, peak temperature and solidification parameters during laser assisted additive manufacturing process. *Materials Science and Technology,* 31**,** 924-930.

MANVATKAR, V. D., GOKHALE, A. A., REDDY, G. J., SAVITHA, U. & DE, A. 2015b. Investigation on laser engineered net shaping of multilayered structures in H13 tool steel. *Journal of Laser Applications,* 27**,** 032010.

MATTHEWS, M. J., GUSS, G., KHAIRALLAH, S. A., RUBENCHIK, A. M., DEPOND, P. J. & KING, W. E. 2016. Denudation of metal powder layers in laser powder bed fusion processes. *Acta Materialia,* 114**,** 33-42.

MAZUMDER, J., CONDE, O., VILAR, R. & STEEN, W. 2012. *Laser Processing: Surface Treatment and Film Deposition*, Springer Science & Business Media.

MCVEY, R., MELNYCHUK, R., TODD, J. & MARTUKANITZ, R. 2007. Absorption of laser irradiation in a porous powder layer. *Journal of laser applications,* 19**,** 214-224.

MILLS, K. C. 2002. *Recommended values of thermophysical properties for selected commercial alloys*, Woodhead Publishing.

MIN, C. 2010. On reinitializing level set functions. *Journal of Computational Physics,* 229**,** 2764-2772.

MIYAGI, M., WANG, H., YOSHIDA, R., KAWAHITO, Y., KAWAKAMI, H. & SHOUBU, T. 2018. Effect of alloy element on weld pool dynamics in laser welding of aluminum alloys. *Scientific reports,* 8.

MOMIN, O., SHUJA, S. Z. & YILBAS, B. S. 2012. Laser heating of titanium and steel: Phase change at the surface. *International Journal of Thermal Sciences,* 54**,** 230-241.

MURR, L. E., QUINONES, S. A., GAYTAN, S. M., LOPEZ, M., RODELA, A., MARTINEZ, E. Y., HERNANDEZ, D. H., MARTINEZ, E., MEDINA, F. & WICKER, R. B. 2009. Microstructure and mechanical behavior of Ti–6Al–4V produced by rapid-layer manufacturing, for biomedical applications. *Journal of the Mechanical Behavior of Biomedical Materials,* 2**,** 20-32.

NANDAN, R., ROY, G., LIENERT, T. & DEBROY, T. 2007. Three-dimensional heat and material flow during friction stir welding of mild steel. *Acta materialia,* 55**,** 883-895.

NG, G., JARFORS, A., BI, G. & ZHENG, H. 2009. Porosity formation and gas bubble retention in laser metal deposition. *Applied Physics A,* 97**,** 641.

NISHI, T., SHIBATA, H., WASEDA, Y. & OHTA, H. 2003. Thermal conductivities of molten iron, cobalt, and nickel by laser flash method. *Metallurgical and Materials Transactions A,* 34**,** 2801-2807.

ONWUBOLU, G. C., DAVIM, J. P., OLIVEIRA, C. & CARDOSO, A. 2007. Prediction of clad angle in laser cladding by powder using response surface methodology and scatter search. *Optics & Laser Technology,* 39**,** 1130-1134.

OSHER, S. & SETHIAN, J. A. 1988. Fronts propagating with curvature-dependent speed: algorithms based on Hamilton-Jacobi formulations. *Journal of Computational Physics,* 79**,** 12-49.

PARK, H. & RHEE, S. 2001. Analysis of weld geometry considering the transferring droplets in gas metal arc welding. *JSME International Journal Series C Mechanical Systems, Machine Elements and Manufacturing,* 44**,** 856-862.

PARTELI, E. J. & PÖSCHEL, T. 2016. Particle-based simulation of powder application in additive manufacturing. *Powder Technology,* 288**,** 96-102.

PARTES, K. 2009. Analytical Model of the Catchment Efficiency in High Speed Laser Cladding. *Surface and Coatings Technology,* 204**,** 366-371.

PATIL, N., PAL, D., RAFI, H. K., ZENG, K., MORELAND, A., HICKS, A., BEELER, D. & STUCKER, B. 2015. A Generalized Feed Forward Dynamic Adaptive Mesh Refinement and Derefinement Finite Element Framework for Metal Laser Sintering—Part I: Formulation and Algorithm Development. *Journal of Manufacturing Science and Engineering,* 137**,** 041001.

PATIL, N., PAL, D. & STUCKER, B. A new finite element solver using numerical eigen modes for fast simulation of additive manufacturing processes. Proceedings of the Solid Freeform Fabrication Symposium, Austin, TX, Aug, 2013. 12-14.

PEYRE, P., AUBRY, P., FABBRO, R., NEVEU, R. & LONGUET, A. 2008. Analytical and numerical modelling of the direct metal deposition laser process. *Journal of Physics D: Applied Physics,* 41**,** 025403.

PINKERTON, A. J. 2007. An analytical model of beam attenuation and powder heating during coaxial laser direct metal deposition. *Journal of Physics D: Applied Physics,* 40**,** 7323.

PINKERTON, A. J. & LI, L. 2004a. Modelling Powder Concentration Distribution From a Coaxial Deposition Nozzle for Laser-Based Rapid Tooling. *Journal of Manufacturing Science and Engineering,* 126**,** 33-41.

PINKERTON, A. J. & LI, L. 2004b. Modelling the geometry of a moving laser melt pool and deposition track via energy and mass balances. *Journal of Physics D: Applied Physics,* 37**,** 1885.

PINKERTON, A. J. & LI, L. 2005. Direct additive laser manufacturing using gas-and water-atomised H13 tool steel powders. *The International Journal of Advanced Manufacturing Technology,* 25**,** 471-479.

PIRCH, N., KREUTZ, E. & OLLIER, B. 1996. The modelling of heat, mass and solute transport in surface processing with laser radiation. *Laser Processing: Surface Treatment and Film Deposition,* 307**,** 177.

POWELL, J., HENRY, P. & STEEN, W. 1988. Laser cladding with preplaced powder: analysis of thermal cycling and dilution effects. *Surface Engineering,* 4**,** 141-149.

QIU, C., PANWISAWAS, C., WARD, M., BASOALTO, H. C., BROOKS, J. W. & ATTALLAH, M. M. 2015a. On the role of melt flow into the surface structure and porosity development during selective laser melting. *Acta Materialia,* 96**,** 72-79.

QIU, C., RAVI, G., DANCE, C., RANSON, A., DILWORTH, S. & ATTALLAH, M. M. 2015b. Fabrication of large Ti–6Al–4V structures by direct laser deposition. *Journal of Alloys and Compounds,* 629**,** 351-361.

RAI, R., ELMER, J., PALMER, T. & DEBROY, T. 2007. Heat transfer and fluid flow during keyhole mode laser welding of tantalum, Ti–6Al–4V, 304L stainless steel and vanadium. *Journal of Physics D: Applied Physics,* 40**,** 5753.

RASTEGARI, H., ASGARI, S. & ABBASI, S. 2011. Producing Ti–6Al–4V/TiC composite with good ductility by vacuum induction melting furnace and hot rolling process. *Materials & Design,* 32**,** 5010-5014.

ROBERTS, G. A., KENNEDY, R. & KRAUSS, G. 1998. *Tool steels*, ASM international.

SAQIB, S., URBANIC, R. & AGGARWAL, K. 2014. Analysis of laser cladding bead morphology for developing additive manufacturing travel paths. *Procedia Cirp,* 17**,** 824-829.

SCHEITHAUER, U., KORDAß, R., NOACK, K., EICHENAUER, M. F., HARTMANN, M., ABEL, J., GANZER, G. & LORDICK, D. 2018. Potentials and challenges of additive manufacturing technologies for heat exchanger. *Adv. Heat Exch,* 4.

SCHOHN, G. & COHN, D. Less is more: Active learning with support vector machines. ICML, 2000. Citeseer, 839-846.

SEIBOLD, G., DAUSINGER, F. & HUEGEL, H. Absorptivity of Nd: YAG-laser radiation on iron and steel depending on temperature and surface conditions. International Congress on Applications of Lasers & Electro-Optics, 2000. Laser Institute of America, E125-E132.

SELI, H., ISMAIL, A. I. M., RACHMAN, E. & AHMAD, Z. A. 2010. Mechanical evaluation and thermal modelling of friction welding of mild steel and aluminium. *Journal of materials processing technology,* 210**,** 1209-1216.

SETHIAN, J. A. & SMEREKA, P. 2003. Level set methods for fluid interfaces. *Annual Review of Fluid Mechanics,* 35**,** 341-372.

SEXTON, L., LAVIN, S., BYRNE, G. & KENNEDY, A. 2002. Laser cladding of aerospace materials. *Journal of Materials Processing Technology,* 122**,** 63-68.

SHI, R., KHAIRALLAH, S., HEO, T. W., ROLCHIGO, M., MCKEOWN, J. T. & MATTHEWS, M. J. 2019. Integrated Simulation Framework for Additively Manufactured Ti-6Al-4V: Melt Pool Dynamics, Microstructure, Solid-State Phase Transformation, and Microelastic Response. *JOM***,** 1-16.

SHRESTHA, S. & CHOU, Y. K. 2019. A Numerical Study on the Keyhole Formation During Laser Powder Bed Fusion Process. *Journal of Manufacturing Science and Engineering***,** 1-20.

SHUNMUGAVEL, M., POLISHETTY, A. & LITTLEFAIR, G. 2015. Microstructure and mechanical properties of wrought and additive manufactured Ti-6Al-4V cylindrical bars. *Procedia Technology,* 20**,** 231-236.

SILBERT, L. E., ERTAŞ, D., GREST, G. S., HALSEY, T. C., LEVINE, D. & PLIMPTON, S. J. 2001. Granular flow down an inclined plane: Bagnold scaling and rheology. *Physical Review E,* 64**,** 051302.

SINGH, J. & MAZUMDER, J. 1987. Microstructure and wear properties of laser clad Fe− Cr− Mn− C alloys. *Metallurgical and Materials Transactions A,* 18**,** 313-322.

SONG, J., CHEW, Y., BI, G., YAO, X., ZHANG, B., BAI, J. & MOON, S. K. 2018. Numerical and experimental study of laser aided additive manufacturing for melt-pool profile and grain orientation analysis. *Materials & Design,* 137**,** 286-297.

STEINWART, I. & CHRISTMANN, A. 2008. *Support vector machines*, Springer Science & Business Media.

STEUBEN, J. C., ILIOPOULOS, A. P. & MICHOPOULOS, J. G. 2016. Discrete element modeling of particle-based additive manufacturing processes. *Computer Methods in Applied Mechanics and Engineering,* 305**,** 537-561.

SUN, Y. & HAO, M. 2012. Statistical analysis and optimization of process parameters in Ti6Al4V laser cladding using Nd: YAG laser. *Optics and Lasers in Engineering,* 50**,** 985-995.

SUSSMAN, M., SMEREKA, P. & OSHER, S. 1994. A level set approach for computing solutions to incompressible two-phase flow. *Journal of Computational Physics,* 114**,** 146-159.

SUTTON, A. T., KRIEWALL, C. S., LEU, M. C. & NEWKIRK, J. W. 2017. Powder characterisation techniques and effects of powder characteristics on part properties in powder-bed fusion processes. *Virtual and physical prototyping,* 12**,** 3-29.

SVENUNGSSON, J., CHOQUET, I. & KAPLAN, A. F. 2015. Laser welding process–a review of keyhole welding modelling. *Physics procedia,* 78**,** 182-191.

TABERNERO, I., LAMIKIZ, A., MARTINEZ, S., UKAR, E. & DE LACALLE, L. L. 2012. Modelling of energy attenuation due to powder flow-laser beam interaction during laser cladding process. *Journal of materials processing technology,* 212**,** 516-522.

TAN, W. & SHIN, Y. C. 2014. Analysis of multi-phase interaction and its effects on keyhole dynamics with a multi-physics numerical model. *Journal of Physics D: Applied Physics,* 47**,** 345501.

THAKAR, Y. D., PAN, H. & LIOU, F. Numerical and Experimental Analysis of the Powder Flow Streams in the Laser Aided Material Deposition Process. Proceeding of the 15th Conference on Solid Freeform Fabrication, 2004. Austin, 512-522.

TONG, S. & KOLLER, D. 2001. Support vector machine active learning with applications to text classification. *Journal of machine learning research,* 2**,** 45-66.

TRAPP, J., RUBENCHIK, A. M., GUSS, G. & MATTHEWS, M. J. 2017. In situ absorptivity measurements of metallic powders during laser powder-bed fusion additive manufacturing. *Applied Materials Today,* 9**,** 341-349.

TSUJI, Y., KAWAGUCHI, T. & TANAKA, T. 1993. Discrete particle simulation of two-dimensional fluidized bed. *Powder technology,* 77**,** 79-87.

VÁSQUEZ, F., RAMOS-GREZ, J. A. & WALCZAK, M. 2012. Multiphysics simulation of laser–material interaction during laser powder depositon. *The International Journal of Advanced Manufacturing Technology,* 59**,** 1037-1045.

VRANCKEN, B., THIJS, L., KRUTH, J.-P. & VAN HUMBEECK, J. 2012. Heat treatment of Ti6Al4V produced by Selective Laser Melting: Microstructure and mechanical properties. *Journal of Alloys and Compounds,* 541**,** 177-185.

WANG, F., MEI, J., JIANG, H. & WU, X. 2007. Laser fabrication of Ti6Al4V/TiC composites using simultaneous powder and wire feed. *Materials Science and Engineering: A,* 445**,** 461-466.

WANG, L. & FELICELLI, S. 2007. Process modeling in laser deposition of multilayer SS410 steel. *Journal of Manufacturing Science and Engineering,* 129**,** 230-241.

WANG, X., LAOUI, T., BONSE, J., KRUTH, J.-P., LAUWERS, B. & FROYEN, L. 2002. Direct selective laser sintering of hard metal powders: experimental study and simulation. *The International Journal of Advanced Manufacturing Technology,* 19**,** 351-357.

WEERASINGHE, V. & STEEN, W. 1986. Laser Surface Cladding. *Laser Surface Treatments of Metals (CW Draper and P. Mazzoldi, eds.), Martinus Nijhoff, Dordrecht***,** 360-387.

WEERASINGHE, V. & STEEN, W. 1987. Laser cladding with pneumatic powder delivery. *Applied Laser Tooling.* Springer.

WEI, P., WEI, Z., CHEN, Z., HE, Y. & DU, J. 2017. Thermal behavior in single track during selective laser melting of AlSi10Mg powder. *Applied Physics A,* 123**,** 604.

WEN, S., SHIN, Y., MURTHY, J. & SOJKA, P. 2009. Modeling of Coaxial Powder Flow for the Laser Direct Deposition Process. *International Journal of Heat and Mass Transfer,* 52**,** 5867-5877.

WEN, S. & SHIN, Y. C. 2010. Modeling of transport phenomena during the coaxial laser direct deposition process. *Journal of Applied Physics,* 108**,** 044908.

WEN, S. & SHIN, Y. C. 2011. Comprehensive predictive modeling and parametric analysis of multitrack direct laser deposition processes. *Journal of Laser Applications,* 23**,** 022003.

WESTERBERG, K., MERIER, T., MCCLELLAND, M., BRAUN, D., BERZINS, L., ANKLAM, T. & STORER, J. 1998. Analysis of the e-beam evaporation of titanium and Ti-6Al-4V. Lawrence Livermore National Lab., CA (United States).

WILSON, J. M., PIYA, C., SHIN, Y. C., ZHAO, F. & RAMANI, K. 2014. Remanufacturing of turbine blades by laser direct deposition with its energy and environmental impact analysis. *Journal of Cleaner Production,* 80**,** 170-178.

WILSON, J. M. & SHIN, Y. C. 2012. Microstructure and wear properties of laser-deposited functionally graded Inconel 690 reinforced with TiC. *Surface and Coatings Technology,* 207**,** 517-522.

WOHLERS, T. T. 2012. *Wohlers report 2012: additive manufacturing and 3D printing state of the industry: annual worldwide progress report*, Wohlers Associates.

WU, X., LIANG, J., MEI, J., MITCHELL, C., GOODWIN, P. & VOICE, W. 2004. Microstructures of laser-deposited Ti–6Al–4V. *Materials & Design,* 25**,** 137-144.

WU, Y.-C., SAN, C.-H., CHANG, C.-H., LIN, H.-J., MARWAN, R., BABA, S. & HWANG, W.-S. 2018. Numerical modeling of melt-pool behavior in selective laser melting with random powder distribution and experimental validation. *Journal of Materials Processing Technology,* 254**,** 72-78.

XIANG, Z., YIN, M., DENG, Z., MEI, X. & YIN, G. 2016. Simulation of forming process of powder bed for additive manufacturing. *Journal of Manufacturing Science and Engineering,* 138**,** 081002.

YAN, W., GE, W., QIAN, Y., LIN, S., ZHOU, B., LIU, W. K., LIN, F. & WAGNER, G. J. 2017. Multi-physics modeling of single/multiple-track defect mechanisms in electron beam selective melting. *Acta Materialia,* 134**,** 324-333.

YANG, G., MA, J., CARLSON, B., WANG, H.-P. & KOVACEVIC, R. 2017. Effect of laser beam configuration on microstructure evolution and joint performance in laser joining AA 6111 panels. *Materials & Design,* 123**,** 197-210.

YANG, J., SUN, S., BRANDT, M. & YAN, W. 2010. Experimental investigation and 3D finite element prediction of the heat affected zone during laser assisted machining of Ti6Al4V alloy. *Journal of Materials Processing Technology,* 210**,** 2215-2222.

YANG, N. 2009. Concentration Model Based on Movement Model of Powder Flow in Coaxial Laser Cladding. *Optics & Laser Technology,* 41**,** 94-98.

YU, J., ROMBOUTS, M., MAES, G. & MOTMANS, F. 2012. Material properties of Ti6Al4V parts produced by laser metal deposition. *Physics Procedia,* 39**,** 416-424.

YUAN, P. & GU, D. 2015. Molten pool behaviour and its physical mechanism during selective laser melting of TiC/AlSi10Mg nanocomposites: simulation and experiments. *Journal of Physics D: Applied Physics,* 48**,** 035303.

ZEKOVIC, S., DWIVEDI, R. & KOVACEVIC, R. 2007. Numerical Simulation and Experimental Investigation of Gas–Powder Flow From Radially Symmetrical Nozzles in Laser-Based Direct Metal Deposition. *International Journal of Machine Tools and Manufacture,* 47**,** 112-123.

ZENG, K., PAL, D., GONG, H., PATIL, N. & STUCKER, B. 2015. Comparison of 3DSIM thermal modelling of selective laser melting using new dynamic meshing method to ANSYS. *Materials Science and Technology,* 31**,** 945-956.

ZHANG, Y., LEE, W. H., WU, L., MENG, L., JUNG, Y.-G. & ZHANG, J. 2018. Multiscale multiphysics modeling of laser powder bed fusion process. *Additive Manufacturing.* Elsevier.

ZHANG, Y., WEI, Z., SHI, L. & XI, M. 2008. Characterization of laser powder deposited Ti–TiC composites and functional gradient materials. *Journal of Materials Processing Technology,* 206**,** 438-444.

ZHAO, C., FEZZAA, K., CUNNINGHAM, R. W., WEN, H., DE CARLO, F., CHEN, L., ROLLETT, A. D. & SUN, T. 2017. Real-time monitoring of laser powder bed fusion process using high-speed X-ray imaging and diffraction. *Scientific reports,* 7**,** 3602.

ZHOU, J., ZHANG, Y. & CHEN, J. 2009. Numerical simulation of laser irradiation to a randomly packed bimodal powder bed. *International Journal of Heat and Mass Transfer,* 52**,** 3137-3146.

ZHU, G., LI, D., ZHANG, A., PI, G. & TANG, Y. 2011. The Influence of Standoff Variations on the Forming Accuracy in Laser Direct Metal Deposition. *Rapid Prototyping Journal,* 17**,** 98-106.

ZOHDI, T. 2006. Computation of the coupled thermo-optical scattering properties of random particulate systems. *Computer Methods in Applied Mechanics and Engineering,* 195**,** 5813-5830.

PUBLICATIONS

Bailey, N.S., Katinas, C. and Shin, Y.C., 2017. Laser direct deposition of AISI H13 tool steel powder with numerical modeling of solid phase transformation, hardness, and residual stresses. *Journal of Materials Processing Technology*, *247*, pp.223-233.

Katinas, C., Shang, W., Shin, Y.C. and Chen, J., 2017, June. Modeling Particle Spray and Capture Efficiency for Direct Laser Deposition Using a Four Nozzle Powder Injection System. In *ASME 2017 12th International Manufacturing Science and Engineering Conference collocated with the JSME/ASME 2017 6th International Conference on Materials and Processing* (pp. V002T01A005-V002T01A005). American Society of Mechanical Engineers.

Shin, Y.C., Bailey, N., Katinas, C. and Tan, W., 2018. Predictive modeling capabilities from incident powder and laser to mechanical properties for laser directed energy deposition. *Computational Mechanics*, *61*(5), pp.617-636.

Katinas, C., Shang, W., Shin, Y.C. and Chen, J., 2018. Modeling Particle Spray and Capture Efficiency for Direct Laser Deposition Using a Four Nozzle Powder Injection System. *Journal of Manufacturing Science and Engineering*, *140*(4), p.041014.

Zhang, B., Katinas, C. and Shin, Y.C., 2018. Robust tool wear monitoring using systematic feature selection in turning processes with consideration of uncertainties. *Journal of Manufacturing Science and Engineering*, *140*(8), p.081010.

Katinas, C., Liu, S. and Shin, Y.C., 2019. Self-sufficient modeling of single track deposition of Ti–6Al–4V with the prediction of capture efficiency. *Journal of Manufacturing Science and Engineering*, *141*(1), p.011001.

Liu, S., Hong, K.M., Katinas, C. and Shin, Y.C., 2019. Multiphysics modeling of phase transformation and microhardness evolution in laser direct deposited Ti6Al4V. *Journal of Manufacturing Processes*, *45*, pp.579-587.

Katinas, C. and Shin, Y.C., 2020. Prediction of initial transient behavior with stationary heating during laser powder bed fusion processes. *International Journal of Heat and Mass Transfer*, *153*, p.119663.

Zhang, B., Katinas, C. and Shin, Y.C., 2020. Robust Wheel Wear Monitoring System for Cylindrical Traverse Grinding. *IEEE/ASME Transactions on Mechatronics*, *25*(5), pp.2220-2229.

Katinas, C., Throop, T., Shin, Y.C. and Frank, A., 2021. Laser cladding of Stellite-6 with a coaxial nozzle via modeling and systematic experimental investigations. *The International Journal of Advanced Manufacturing Technology*, *113*(3), pp.837-853.